

**Structure and function of integral and
peripheral membrane proteins by cryo-EM:
RyR1 and SidE family proteins**

Dissertation

Zur Erlangung des Doktorgrades
der Naturwissenschaften

vorgelegt beim Fachbereich 14
Biochemie, Chemie und Pharmazie
der Johann Wolfgang Goethe-Universität
in Frankfurt am Main

von

Wenbo Chen

aus China

Frankfurt am Main, 2020

(D30)

Diese Arbeit wurde in der Arbeitsgruppe von Dr. Misha Kudryashev der Abteilung Strukturbiologie des Max-Planck-Institutes für Biophysik in Frankfurt am Main durchgeführt und vom Fachbereich 14 Biochemie, Chemie und Pharmazie der Johann Wolfgang Goethe-Universität als Dissertation angenommen.

Dekan:

1.Gutachter: Dr. Misha Kudryashev

2.Gutachter: Prof. Dr. Klaas Martinus Pos

Datum der Disputation: 08.09.2020

Table of contents

Abstract	1
Zusammenfassung	5
List of figures	11
Chapter 1: Introduction.....	13
Membrane proteins and cryo-electron microscopy	13
Chapter 2: Structures of RyR1 in native membranes.....	25
2.1 Introduction into the role of RyR1 in excitation-contraction coupling.....	25
2.2 Methods	31
2.2.1 Biochemical sample preparation	31
2.2.2 Cryo-EM grid preparation and tomographic data collection	32
2.2.3 Image processing	33
2.2.4 Analysis of conformational heterogeneity	34
2.3 Results: structure of RyR1 in native membranes	35
2.3.1 SR isolation by sucrose gradient centrifugation	35
2.3.2 SR image by cryo-EM	36
2.3.3 Structures of RyR1.....	37
2.3.4 An unaccommodated density in the cytoplasmic domain.....	43
2.3.5 The helix-like density in the SR membrane	45
2.3.6 Interactions of RyR1 in the SR lumen	46
2.3.7 Structural variation of the RyR1 domains in the native membranes	48
2.3.8 Activation of RyR1 in native membranes	50
2.4 Discussion and outlook	54
Chapter 3: Improvement of the resolution of RyR1 by hybrid single particle- subtomogram averaging	61
3.1 Introduction of hybrid single particle-subtomogram averaging.....	61
3.2 Methods	64
3.2.1 Tomographic data collection	64
3.2.2 Tomographic data processing	65
3.3 Results	66
3.3.1 Structure of RyR1 in native membranes at sub-nanometer resolution	66

3.4 Discussion and outlook	69
Chapter 4: Structure of SidE family proteins by single-particle cryo-EM	71
4.1 Introduction	71
4.2 Methods	78
4.2.1 Protein expression and purification	78
4.2.2 Cryo-EM grid preparation and single particle image data collection	79
4.2.3 Image processing	79
4.3 Results	80
4.3.1 Purification of SdeC	80
4.3.2 Cryo-EM structure of SdeC	81
4.3.3 CC domain and the composite map of SdeA-CC ₂₃₁₋₁₄₉₉	85
4.4 Discussion and outlook	87
Chapter 5: Concluding remarks and future perspectives	93
References.....	97
Declaration of Contributions and Publications.....	111
Curriculum Vitae	113
Publications.....	115
Acknowledgment.....	117

Abstract

Membrane proteins play important roles in most aspects of life, not surprising that membrane proteins are also prime drug targets. Obtaining the structures of membrane proteins is key to understand their functions and mechanisms, which is typically difficult as the proteins have to be extracted from the native context making their handling and interpretation of the results challenging. In recent years cryo-electron microscopy (cryo-EM) techniques are developed quickly and are applied widely to high-resolution structural studies of membrane proteins. The two major modalities of cryo-EM techniques are single-particle analysis and tomography and subtomogram averaging, which are suitable for purified proteins and proteins in native context, respectively.

Ryanodine receptor 1 (RyR1) is the largest known ion channel to date, which is located on the membrane of sarcoplasmic reticulum (SR) of mammalian skeletal muscle cells. RyR1 mediates excitation-contraction coupling by releasing Ca^{2+} from SR to the cytoplasm of skeletal muscle cells. RyR1 possesses a giant cytoplasmic region and a transmembrane region, which can bind many regulatory proteins and small molecules. RyR1 activation is regulated by several proteins from both the cytoplasm and lumen of the SR. So far the structures of purified RyR1 have been investigated extensively by single-particle cryo-EM and near-atomic resolution structures at various functional states have been reported, which provided structural insights into the gating and opening mechanisms of RyR1. However, in those studies the role of native SR membrane in the activation and regulation of RyR1 was not clarified due to the lack of native environment, preventing us to fully understand the mechanisms of RyR1 in native environment. In this work I isolated SR from rabbit skeletal muscle and we solved the structures of RyR1 in its native SR membrane

in apo and ryanodine-binding states by tomography and subtomogram averaging, at 12.6 Å and 17.5 Å, respectively. Compared to the previously reported single-particle structures of purified RyR1, my structures reveal additional densities at cytosolic domain and in the SR membrane and SR lumen, which are an unaccommodated density, helix-like densities traversing the bilayer approximately 5 nm from the RyR1 transmembrane domain, and sarcoplasmic extensions linking RyR1 to a putative calsequestrin network, respectively. Activation of RyR1 leads to contraction of cytosolic domain and significant changes in membrane curvature and inward movement of the sarcoplasmic extensions. This is the first time for the conformational changes of RyR1 in native membrane upon activation to be observed. In addition, we could be able to improve the resolution of the structure of RyR1 in apo state in native membrane to 9.5 Å using hybrid method, which incorporated single-particle analysis and tomography and subtomogram averaging. The quality of the density of the helices in transmembrane domain are greatly improved in the higher resolution structure, which allows accurate docking of the transmembrane helices from previous single-particle structure. The structures of RyR1 in native membrane present additional features compared to purified RyR1, which indicates that native environment is important for membrane proteins to preserve the full structures and functions. Deeper structural insights into the activation and regulation mechanisms of RyR1 in its native environment are provided in our work.

The second project during my thesis focused on a peripheral membrane protein from SidE family which a pathogenic gram-negative bacterium *Leginella pneumophila* uses to aid the infection process into host cells utilizing the bacterial type IV secretion system. *Leginella pneumophila* is widespread in fresh water environment and can infect especially

immunocompromised people, which can lead to severe symptoms. To date more than 300 kinds of effector proteins including SidE family proteins have been discovered to be involved into the infection of host cell and replication of *Leginella pneumophila*. SidE family proteins are involved in the non-canonical ubiquitylation using NAD as energy, which inhibits the canonical ubiquitylation of host cell and disrupts the normal cellular processes. Currently there are several crystal structures of the SidE family members in truncated forms reported, revealing the catalytic mechanisms of ubiquitylation. However, the missing C-terminal in the crystal structure is critical for the localization of the whole protein to ER membrane. The lack of the structure of the C-terminal hinders us to understand the mechanism of localization. Here, we solved the structure of the member SdeC in its full length form at 4.6 Å by single-particle cryo-EM. In addition, the crystal structure of the C-terminal of the member SdeA was solved to 2 Å by our collaborators. By superimposing one common helix of these two structures, we could be able to build a combined model and get a generalized understanding of the SidE family proteins. Our structural analysis revealed for the first time the functional membrane-interacting domains which were missing in the previous structures and broadened our understanding of SidE family proteins.

In conclusion, structures of RyR1 in closed and open states in native membrane were solved to 12.6 Å and 17.5 Å using tomography and subtomogram averaging, respectively, which show additional features of RyR1 compared to the reported single particle structures and present the conformational changes of RyR1 including SR membrane upon activation. The structure of closed RyR1 was further improved to 9.5 Å using hybrid method, which has greatly improved the quality of transmembrane helices. Those results not only provided us a panoramic view of the structure of

RyR1 in native SR membrane, but also expanded our understanding into the mechanism of RyR1 in native SR membrane. The structure of purified SdeC was solved to 4.6 Å using single particle analysis, combining with the crystal structure of the C-terminal of SdeA the near-full length model of SidE family proteins were built for the first time, which provides further insights into its mechanism.

Zusammenfassung

Membranproteine spielen in den meisten Lebensbereichen eine wichtige Rolle, was nicht überrascht, dass Membranproteine auch Hauptarzneimittelziele sind. Das Erhalten der Strukturen von Membranproteinen ist der Schlüssel zum Verständnis ihrer Funktionen und Mechanismen. Dies ist typischerweise schwierig, da die Proteine aus dem nativen Kontext extrahiert werden müssen, was ihre Handhabung und die Interpretation der Ergebnisse schwierig macht. In den letzten Jahren wurden Kryoelektronenmikroskopie (Kryo-EM) Techniken schnell entwickelt und in großem Umfang auf hochauflösende Strukturuntersuchungen von Membranproteinen angewendet. Die beiden Hauptmodalitäten der Kryo-EM-Techniken sind Einzelpartikelanalyse und Tomographie sowie Subtomogramm-Mittelung, die für gereinigte Proteine und Proteine im nativen Kontext geeignet sind.

Der Ryanodinrezeptor 1 (RyR1) ist der bislang größte bekannte Ionenkanal, der sich auf der Membran des sarkoplasmatischen Retikulums (SR) von Säugetierskelettmuskelzellen befindet. RyR1 vermittelt die Anregungs-Kontraktions-Kopplung durch Freisetzung von Ca^{2+} aus dem SR in das Zytoplasma von Skelettmuskelzellen. RyR1 besitzt eine riesige zytoplasmatische Region und eine Transmembranregion, die viele regulatorische Proteine und kleine Moleküle binden können. Die RyR1-Aktivierung wird durch mehrere Proteine sowohl aus dem Zytoplasma als auch aus dem Lumen des SR reguliert. Hier berichten wir über die Struktur von RyR1 in geschlossenen und offenen Zuständen von nativen SR-Membranen. Bisher wurden die Strukturen von gereinigtem RyR1 ausführlich durch Einzelpartikel Kryo-EM untersucht, und es wurden Strukturen mit nahezu atomarer Auflösung in verschiedenen Funktionszuständen beschrieben, die strukturelle Einblicke in die Gate-

und Öffnungsmechanismen von RyR1 lieferten. In diesen Forschungen wurde jedoch die Rolle der nativen SR-Membran bei der Aktivierung und Regulation von RyR1 aufgrund des Mangels an nativer Umgebung nicht geklärt, was uns daran hinderte, die Mechanismen von RyR1 in nativer Umgebung vollständig zu verstehen. In dieser Arbeit isolierte ich SR aus dem Skelettmuskel von Kaninchen und löste die Strukturen von RyR1 in seiner nativen SR-Membran in Apo- und Ryanodin-Bindungszuständen durch Tomographie und Subtomogramm-Mittelung bei 12,6 Å und 17,5 Å. Verglichen mit den zuvor beschriebenen Einzelpartikelstrukturen von gereinigtem RyR1 zeigen meine Strukturen zusätzliche Dichten in der cytosolischen Domäne und in der SR-Membran und im SR-Lumen, bei denen es sich um helixartige Dichten handelt, die die Doppelschicht ungefähr 5 nm von der RyR1-Transmembrandomänen durchqueren und sarkoplasmatische Verlängerungen, die RyR1 mit einem mutmaßlichen Calsequestrin-Netzwerk verbinden. Die Aktivierung von RyR1 führt zu einer Kontraktion der cytosolischen Domäne und signifikanten Änderungen der Membrankrümmung und der Bewegung der sarkoplasmatischen Verlängerungen nach innen. Dies ist das erste Mal, dass Konformationsänderungen von RyR1 in der nativen Membran bei Aktivierung beobachtet werden. Zusätzlich sind wir in der Lage, die Auflösung der Struktur von RyR1 im Apo-Zustand in der nativen Membran unter Verwendung der Hybridmethode, die Einzelpartikelanalyse sowie Tomographie und Subtomogramm-Mittelung umfasste, auf 9,5 Å zu verbessern. Die Qualität der Dichte der Helices in der Transmembrandomäne ist in der Struktur mit höherer Auflösung stark verbessert, was ein genaues Andocken der Transmembranhelices von der vorherigen Einzelpartikelstruktur ermöglicht. Die Strukturen von RyR1 in der nativen Membran weisen im Vergleich zu gereinigtem RyR1

zusätzliche Merkmale auf, was darauf hinweist, dass die native Umgebung für Membranproteine wichtig ist, um die vollständigen Strukturen und Funktionen zu erhalten. In unserer Arbeit werden tiefere strukturelle Einblicke in die Aktivierungs- und Regulationsmechanismen von RyR1 in seiner natürlichen Umgebung gegeben.

Das zweite Projekt während meiner Doktorarbeit konzentrierte sich auf ein peripheres Membranprotein aus der SidE-Familie, das ein pathogenes gramnegatives Bakterium *Leginella pneumophila* verwendet, um den Infektionsprozess in Wirtszellen unter Verwendung des bakteriellen Typ IV-Sekretionssystems zu unterstützen. *Leginella pneumophila* ist in frischen Wasserumgebungen weit verbreitet und kann insbesondere immungeschwächte Menschen infizieren, was zu schweren Symptomen führen kann. Bisher wurde festgestellt, dass mehr als 300 Arten von Effektorproteinen, einschließlich Proteinen der SidE-Familie, an der Infektion der Wirtszelle und der Replikation von *Leginella pneumophila* beteiligt sind. Proteine der SidE-Familie sind an der nicht-kanonischen Ubiquitylierung unter Verwendung von NAD als Energie beteiligt, wodurch die kanonische Ubiquitylierung der Wirtszelle gehemmt und die normalen zellulären Prozesse gestört werden. Derzeit sind einige Kristallstrukturen der SidE-Familienmitglieder in verkürzter Form beschrieben, die die katalytischen Mechanismen der Ubiquitylierung aufklären. Der fehlende C-Terminus in der Kristallstruktur ist jedoch entscheidend für die Lokalisierung des gesamten Proteins zur ER-Membran. Das Fehlen der Struktur des C-Terminus erschwert das Verständnis des Lokalisierungsmechanismus. Hier wollen wir die Struktur

des Mitglieds SdeC in voller Länge durch Einzelpartikel-Kryo-EM lösen. Die Struktur hat eine Gesamtauflösung von 4.6 Å. Zusätzlich wurde die Kristallstruktur des C-Terminus des Mitglieds SdeA von unserem Projektpartners auf 2 Å angehoben. Durch Überlagerung einer gemeinsamen Helix dieser beiden Strukturen konnten wir ein kombiniertes Modell erstellen und ein allgemeines Verständnis der Proteine der SidE-Familie erhalten. Unsere Strukturanalyse ergab zum ersten Mal die funktionellen membranwechselwirkenden Domänen, die in den vorherigen Strukturen fehlten, und erweiterte unser Verständnis der Proteine der SidE-Familie.

Zusammenfassend wurden Strukturen von RyR1 in geschlossenen und offenen Zuständen in nativer Membran unter Verwendung von Tomographie- und Subtomogramm-Mittelung auf 12,6 Å und 17,5 Å gelöst, die zusätzliche Merkmale von RyR1 im Vergleich zu den angegebenen Einzelpartikelstrukturen zeigen und die Konformationsänderungen von RyR1 darstellen einschließlich SR-Membran bei Aktivierung. Die Struktur von geschlossenem RyR1 wurde unter Verwendung der Hybridmethode weiter auf 9,5 Å verbessert, was die Qualität der Transmembranhelices erheblich verbessert hat. Diese Ergebnisse lieferten uns nicht nur einen Panoramablick auf die Struktur von RyR1 in der nativen SR-Membran, sondern erweiterten auch unser Verständnis für den Mechanismus von RyR1 in der nativen SR-Membran. Die Struktur von gereinigtem SdeC wurde mithilfe einer Einzelpartikelanalyse auf 4,6 Å gelöst. In Kombination mit der Kristallstruktur des C-Terminus von SdeA wurde erstmals das nahezu

vollständige Modell von Proteinen der SidE-Familie erstellt, das weitere Einblicke in das SdeC liefert Mechanismus.

List of figures

Figure 1.1: Types and function of membrane proteins	14
Figure 1.2: Cartoon model of biological membrane and its components	15
Figure 1.3: Models of artificial membranes used for membrane protein solubilization	17
Figure 1.4: Negative stain and cryo-EM sample preparation.....	18
Figure 1.5: Examples of structures of membrane proteins solved by cryo-EM.....	19
Figure 1.6: The workflow of single particle cryo-EM	21
Figure 1.7: Tomographic data collection and 3D reconstruction.....	22
Figure 1.8: Overview of subtomogram averaging workflow	23
Figure 1.9: Resolution trends for single-particle analysis and subtomogram averaging	24
Figure 2.1.1: Composition and model of triad junction	26
Figure 2.1.2: The morphology of the purified RyR	28
Figure 2.1.3: An atomic model derived from single particle cryo-EM structures of RyR1.....	29
Figure 2.1.4: Schematic representation of RyR1 activation and pore opening.....	30
Figure 2.3.1.1: Sample preparation	36
Figure 2.3.2.1: A slice through a low-pass filtered tomogram showing SR vesicles in contact with a putative T-tubule.....	37
Figure 2.3.3.1: Structure of RyR1 <i>in situ</i> in the apo state	39
Figure 2.3.3.2: Volume-rendered visualizations of the average structure of RyR1 at 12.6 Å resolution	40
Figure 2.3.3.3: Structural similarities between the <i>in situ</i> structure and previously reported high-resolution structures of purified RyRs	41
Figure 2.3.3.4: Rigid-body fitting of the atomic model 5TB2 into the <i>in situ</i> structure	42
Figure 2.3.3.5: Putative inter-protomer interactions between RyR1 tetramers in native membranes.....	43
Figure 2.3.4.1: The unaccommodated density in the cytoplasmic domain.....	44
Figure 2.3.5.1: The slice through the <i>in situ</i> structure and a thin slice through a volume-rendered representation of the structure with PDB 5TB2 fitted	45

Figure 2.3.6.1: Intra-SR extensions of RyR1	47
Figure 2.3.7.1: Structural heterogeneity of RyR1 <i>in situ</i>	50
Figure 2.3.8.1: Structure of RyR1 in the presence of Ca ²⁺ and ryanodine.....	51
Figure 2.3.8.2: Activation of RyR1 <i>in situ</i>	52
Figure 2.3.8.3: Measuring the local curvature of the membrane by transforming the density maps into spherical coordinates and varying the distance to the origin of the coordinate system	53
Figure 3.1.1: Comparisons of the untilted and tilted images.....	63
Figure 3.1.2: Hybrid subtomogram averaging workflow	64
Figure 3.3.1.1: The new structure of closed RyR1 <i>in situ</i>	66
Figure 3.3.1.2: Volume-rendered visualizations of the new average structure of closed RyR1 at 9.5 Å resolution	67
Figure 3.3.1.3: Improvements of the new RyR1 structure	68
Figure 4.1.1: The infection processes of <i>L. pneumophila</i> in phagocytes	72
Figure 4.1.2: The SidE family members	73
Figure 4.1.3: The mechanisms of canonical and noncanonical ubiquitylation pathways	75
Figure 4.1.4: Crystal structure of truncated SdeA.....	76
Figure 4.1.5: Components and structures of the Dot/Icm T4BSSs	77
Figure 4.3.1.1: Purification of SdeC.....	81
Figure 4.3.2.1	83
Figure 4.3.2.2: 3D classification and local refinement of the SdeC density map	84
Figure 4.3.2.3: Resolution of SdeC by single-particle cryo-EM.....	85
Figure 4.3.3.1: Crystal structure of SdeA-CC ₁₁₅₈₋₁₄₉₉	86
Figure 4.3.3.2	87
Figure 4.4.1: Overlay of the longer-SdeA and the two shorter-SdeA.....	89
Figure 4.4.2: Assumed interaction between DotL(656-783)-IcmW-IcmS complex and SdeA-CC ₁₁₅₈₋₁₄₉₉	91

Chapter 1: Introduction

Membrane proteins and cryo-electron microscopy

Living cells and cell organelles contain biological membranes that is highly waterproof and electrochemically sealed (Mio & Sato, 2018). Membrane proteins refers to proteins that are embedded in membrane, which contain two types, namely integral and peripheral proteins (Figure 1.1). Integral proteins are permanently embedded in membrane spanning the bilayer. Major folds of integral membrane proteins include α -helix, helical bundle and β -barrel proteins. Peripheral proteins are temporally anchored to one surface of the membrane by non-covalent interactions (von Heijne, 2006). Membrane proteins play important roles in cells such as transportation of molecules and ions, signal transduction, cell recognition, receptors and enzymatic catalyzing (Figure 1). In humans membrane proteins also regulate a number of critical functions related to muscle, heart and brain function. Among the genome of all organisms, membrane proteins are encoded by nearly 20-30% of the genes. Since membrane proteins are involved in various cellular processes and associated with many related diseases, they are important drug target, in fact more than 50% of drugs are developed based on membrane proteins such as G protein-coupled receptors (GPCR) and ion channels (Mio & Sato, 2018).

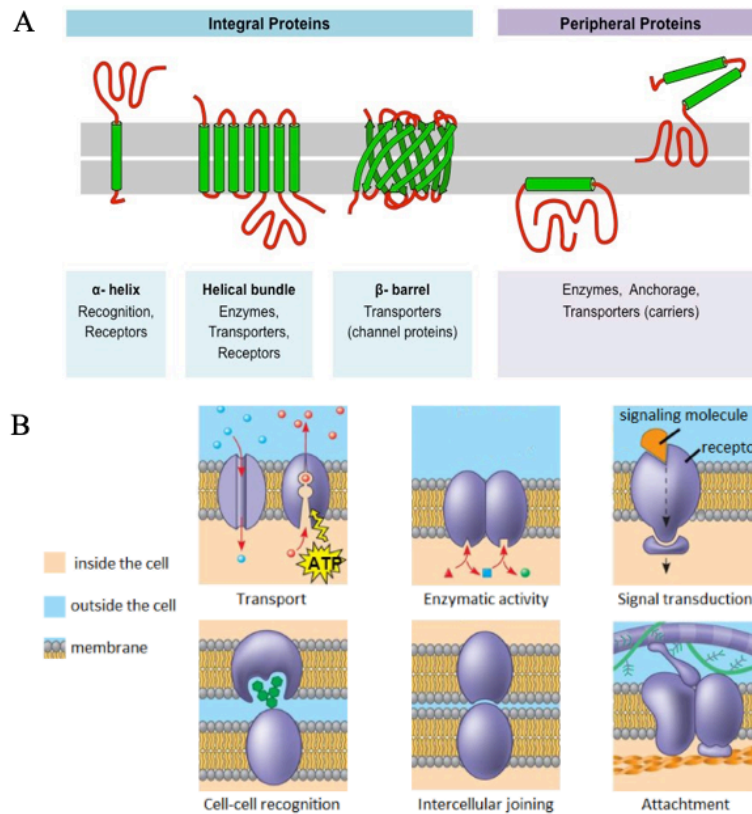


Figure 1.1. Types and function of membrane proteins. A: Diagrams of integral proteins and peripheral membrane proteins. Integral proteins can be classified into α -helix, helical bundle and β -barrel; peripheral proteins, which is adhered to the membrane either by an amphipathic α -helix or by hydrophobic loops. (adapted from (Nidhish Raj, 2018)) B: Various functions of membrane proteins in living organisms. (adapted from Campbell *et al.* 9th edition)

The biological membranes containing membrane proteins comprise hundreds of different lipids, which are asymmetrically distributed in the bilayers. The variety of biological membrane compositions leads to complicated lipid-protein interactions (Nyholm, 2015, van Meer, Voelker et al., 2008) (Figure 1.2). Lipids do not only provide an embedding environment for membrane proteins but also actively participate in the regulation of membrane proteins, such as trafficking, activity and localization (van Meer et al., 2008). Membrane proteins can either specifically bind lipids, where there are defined binding sites for lipids, or

nonspecifically, where lipids act as a medium to regulate membrane proteins through the membrane thickness, fluidity and curvature (Contreras, Ernst et al., 2011, Laganowsky, Reading et al., 2014). Moreover, membrane proteins may also be regulated by other factors such as other proteins and transmembrane ion gradients and lipid raft.

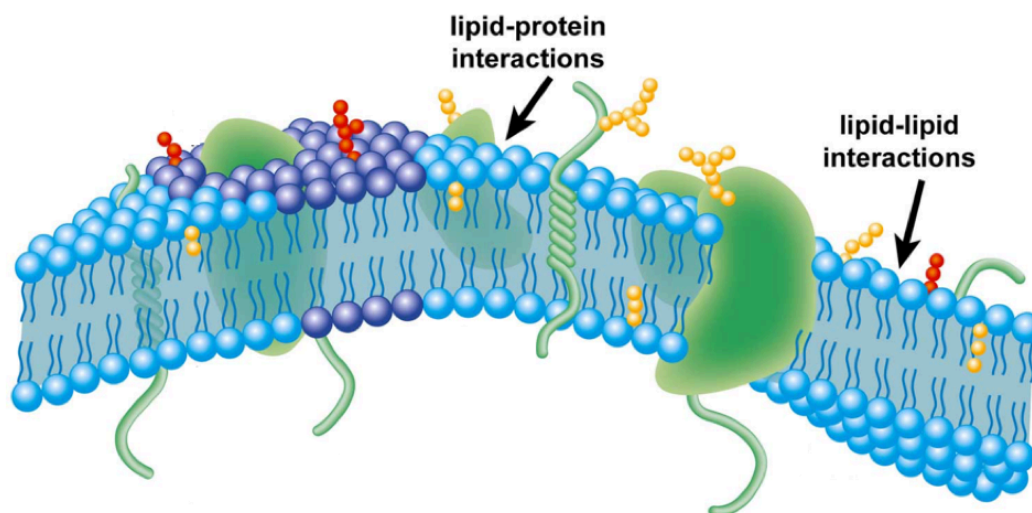


Figure 1.2. Cartoon Model of biological membrane and its components. Blue molecules represent lipids with a hydrophilic head and two hydrophobic tails; green molecules represent various membrane proteins in the membrane; purple area represents lipid raft which comprises cholesterol and glycosphingolipids; red and yellow molecules represent glycolipids. There are various interactions of membrane protein and lipids or between lipids in the biological membrane. (adapted from www.asbmb.org)

Knowing the structures of membrane proteins is necessary to understand their biological mechanisms and design new drugs. Despite their huge importance, so far only about 7% of the structures in the protein data bank (PDB) come from membrane proteins in 2016 (De Zorzi, Mi et al., 2016). The highly hydrophobic property is the intrinsic nature of membrane proteins, which makes the sample preparation more difficult than water-soluble proteins.

Preparing membrane proteins for structural determination involves a critical first step of extracting them from the membranes. There are two commonly used methods, namely purifying membrane proteins in their native membrane without using detergent and from heterologously-expressed cells or native tissue by using detergent. There are several strategies to solubilize membrane proteins during purification (Figure 1.3). Detergents are commonly used in purification of membrane proteins to solubilize and stabilize them. The type of detergent, critical micelle concentration (CMC) and micelle size of different detergents need to be carefully chosen and screened for purifying membrane proteins, as inappropriate or nonoptimal concentration of detergents may result in functional abnormality or physical aggregation or dissociation of subunits of membrane proteins (Mio, Mio et al., 2010). In addition, detergents can be substituted with more stable polymers such as amphipol to solubilize membrane proteins. Detergent-solubilized proteins can be reconstituted into bicelle or liposome, which can provide artificial membrane environment. Nanodisc technologies emerged in recent years, which allow membrane proteins being reconstituted into lipid bilayer surrounded by scaffold proteins or different polymers and also provide a near-native environment (Mio & Sato, 2018).

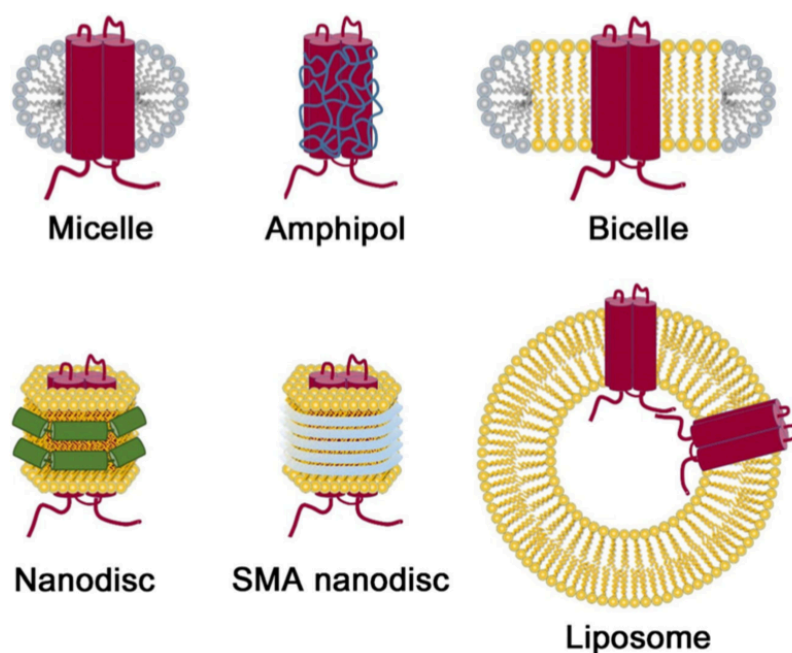


Figure 1.3. Models of various artificial membranes used for membrane protein solubilization. Detergents form micelle with membrane protein. Amphipathic polymer amphipoles can be in place of detergents to solubilize membrane protein, which form stable complexes with membrane protein. Bicelles are generated by mixing two phospholipids and detergents, phospholipids (shown as yellow molecules) with long chains interact with the protein and form a bilayer, and detergents (shown as gray molecules) with short chains fill the rim of bicelle. For the nanodisc, two membrane scaffold proteins assemble around detergent-solubilized membrane proteins with lipids to form disc-shaped particles. Styrene-maleic acid (SMA) copolymers wrap around the hydrophobic acyl chains of lipid bilayer. Membrane proteins are reconstituted into liposomes to form proteoliposomes. (adapted from (Mio & Sato, 2018))

There are three main techniques to solve structure of biomacromolecules including membrane proteins, which are x-ray crystallography, nuclear magnetic resonance (NMR) spectroscopy and electron microscopy (EM). Crystallography and NMR spectroscopy can provide detailed information on the structures, however they are limited to the molecular weights of biomacromolecules. EM is the major technique to determine structures over the molecular to cellular size range. EM has two kinds sample

preparation methods: negative stain and cryo-EM (Figure 1.4). Negative stain is quick and simple to do and can provide a low resolution model for high resolution structure determination; cryo-EM stabilizes biomacromolecules in the native and hydrated state and the high resolution information is well-preserved, allowing high resolution structures to be solved.

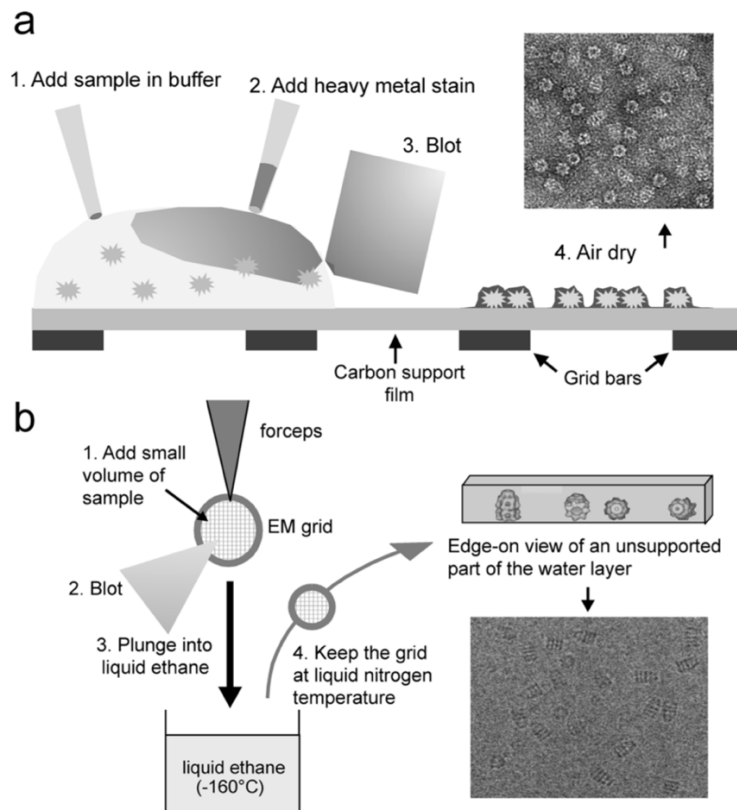


Figure 1.4. Negative stain and cryo-EM sample preparation. (a): Workflow of negative stain sample preparation. Sample is first deposited to the EM grid, and add heavy metal stain and blot away excessive liquid, then wait until grid dries and it can be used for imaging. (b): Workflow of cryo-EM sample preparation. Sample is applied to the cryo-EM grid, excessive buffer is removed by blotting the grid with filter papers, afterwards grid is plunged into liquid ethane, finally transfer and save the grid in liquid nitrogen and can be further imaged.

(adapted from *Orlova et al.* (Orlova & Saibil, 2011))

Cryo-EM has three imaging modalities: single particle cryo-EM, cryo electron tomography (cryo-ET) and electron diffraction of 2D or 3D crystals. In recent years with the developments of direct electron detector and algorithms of data processing (Kimanius, Forsberg et al., 2016, Li, Mooney et al., 2013b), single particle cryo-EM is becoming a sought-after technique, which is able to solve the structures of many biomacromolecules to atomic resolution (Bai, McMullan et al., 2015, Cheng, 2018, Fernandez-Leiro & Scheres, 2016, Kuhlbrandt, 2014) (Figure 1.5). Compared to the other two techniques: crystallography and nuclear magnetic resonance (NMR), single particle cryo-EM does not need huge amounts of biological specimen to crystalize and is suitable for specimens in a wide range (currently small up to 52 kilodalton (Fan, Wang et al., 2019), big up to 10^3 megadalton (Fang, Zhu et al., 2019)) of molecular weight.

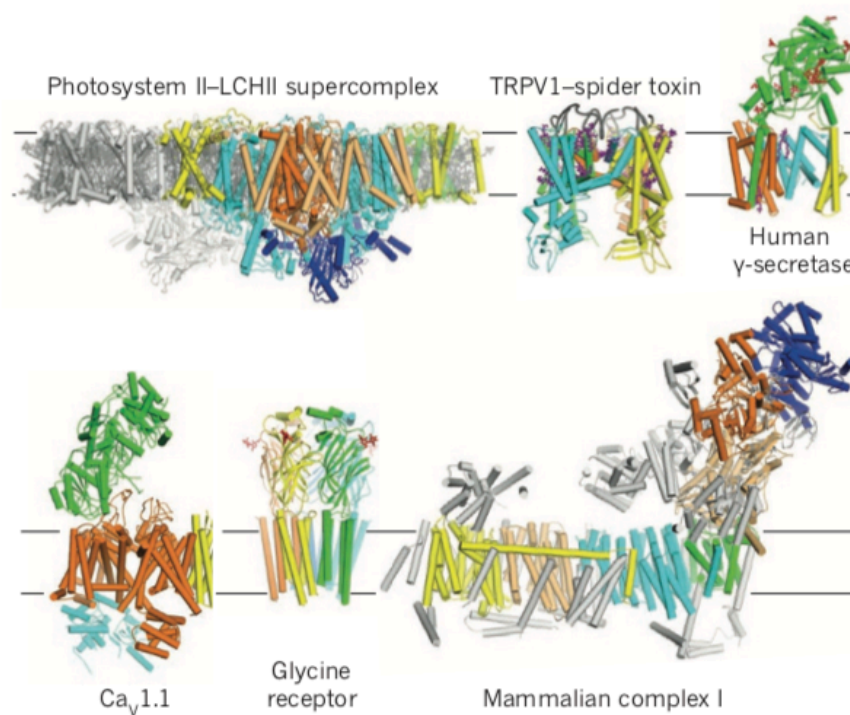


Figure 1.5. Examples of structures of membrane proteins solved by cryo-EM: the photosystem-light harvesting II supercomplex (Wei, Su et al., 2016b), TRPV 1 in

complex with the spider toxin D α Tx (Cao, Liao et al., 2013), human γ -secretase (Bai, Yan et al., 2015), the voltage-gated calcium channel Ca_v1.1 (Wu, Yan et al., 2015), the glycine receptor and mammalian complex (Vinothkumar, Zhu et al., 2014). (adapted from (Fernandez-Leiro & Scheres, 2016))

The workflow of single particle cryo-EM includes sample preparation, cryo-grids freezing/negative staining grids preparation, image data acquisition and processing, which is becoming much more automated due to hardware and software developments (Figure 1.6). Sample used for cryo-EM analysis should have the same high quality as that for crystallography, which should be pure and homogeneous. However, for single particle cryo-EM sample is present in solution and does not need to be crystallized. Before freezing grids, the quality of sample such as purity and homogeneity is typically checked by negative staining EM. Promising sample can be further cryo prepared for structural analysis. At this stage only a few microgram of sample is required which is several orders of magnitude lower than would be required for crystallization. Cryo grids are further transferred to high-end cryo EM such as 300 kV Titan Krios for high resolution image data collection. When protein particles have different orientations in amorphous ice, micrographs could be collected automatically, protein particles are picked manually or automatically, classified and averaged, class averages can be combined to generate the 3D structure of protein according to the central slice theorem (Orlova & Saibil, 2011).

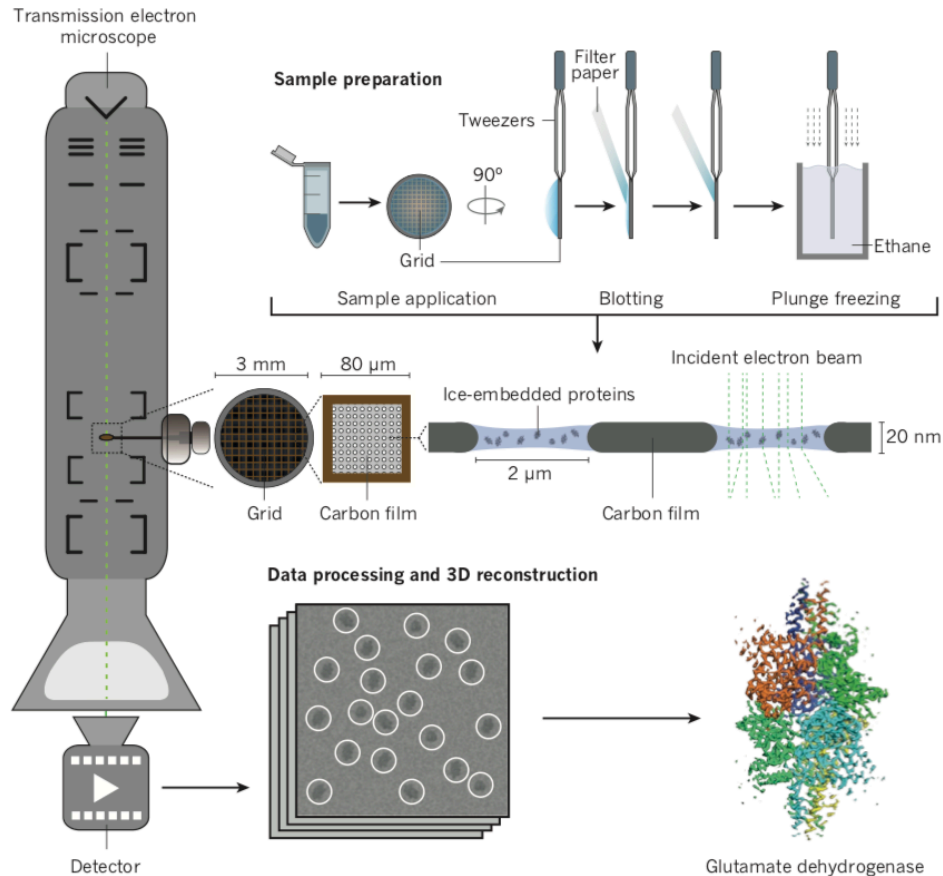


Figure 1.6. The workflow of single particle cryo-EM, which includes grid preparation, data collection, data processing and reconstruction. A few microliters of purified protein is applied to EM grid, the excess liquid is blotted away by filter paper and the grid is plunged into liquid ethane, the protein is flash-frozen and embedded in the vitreous ice. The grid is transferred into cryo-EM. Two-dimensional images of proteins in different orientations are acquired by the detector. The data are processed to combine all images of the protein to generate the 3D structure. Structure of glutamate dehydrogenase is shown as an example which is determined by single particle cryo-EM (adapted from (Fernandez-Leiro & Scheres, 2016)).

Purified proteins, organelles, small organelles and peripheries of cells thinner than ~ 500 nm can be imaged by cryo electron tomography. (Figure 1.7). Computational reconstruction allows observing protein and lipid densities at resolutions of several nanometers. Repeating molecular copies could be picked, mutually aligned and averaged in 3D in a process called

subtomogram averaging (Castano-Diez & Zanetti, 2019, Galaz-Montoya & Ludtke, 2017, Wan & Briggs, 2016, Zhang, 2019), this method is especially suitable for samples which are difficult to purify and provides the information about structure of protein complexes in the native context without purification.

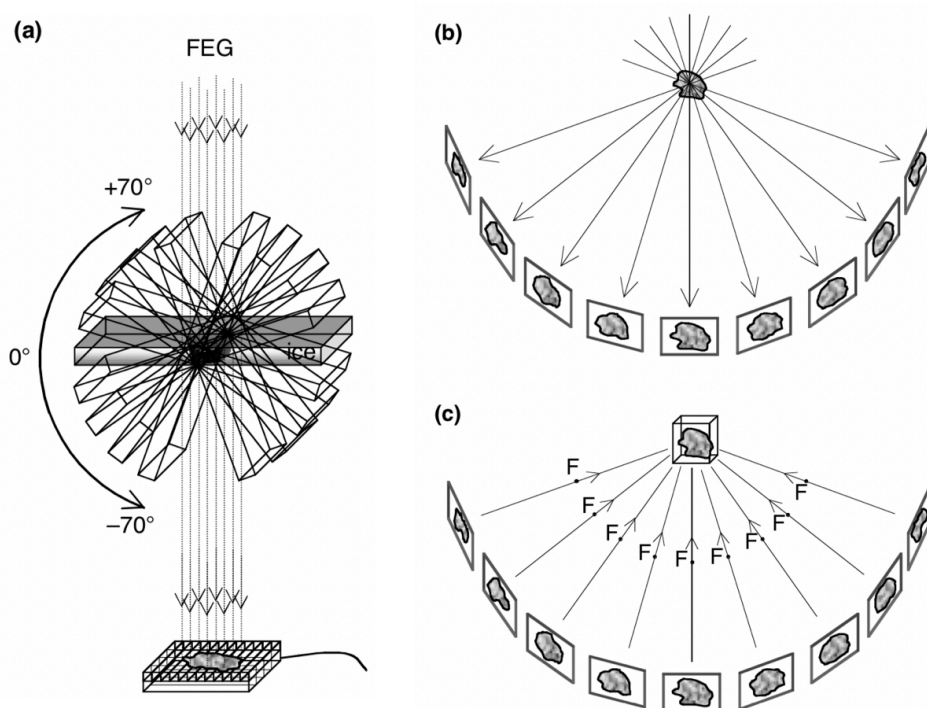


Figure 1.7. Tomographic data collection and 3D reconstruction. (a): The stage carrying cryo grids is rotated in a certain range of angle (example: from -70° to 70°) around an axis perpendicular to the electron beam [field-emission gun (FEG)]. (b): At each tilted angle, the projection of the specimen is recorded on the camera. (c): each projection is back-projected along the projected direction to reconstruct the 3D volume, which is called tomogram.

(Adapted from Steven *et.al.* (Steven & Aebi, 2003))

The identical particles of the biomacromolecule namely sub-tomograms with random orientations are recognized and picked from the 3D tomogram, which can be aligned and averaged to generate an initial model of the biomacromolecule, then the sub-tomograms are aligned to the initial

model and averaged to yield the structure as a new reference, the alignment and averaging processes are iterated until the final structure is stable (Figure 1.8). Usually the subtomograms have missing wedges because the angle range of stage of EM is limited, averaging of the sub-tomograms can not only alleviate or solve the missing wedge issue, but also produces structure with greatly improved contrast and resolution (Wan & Briggs, 2016).

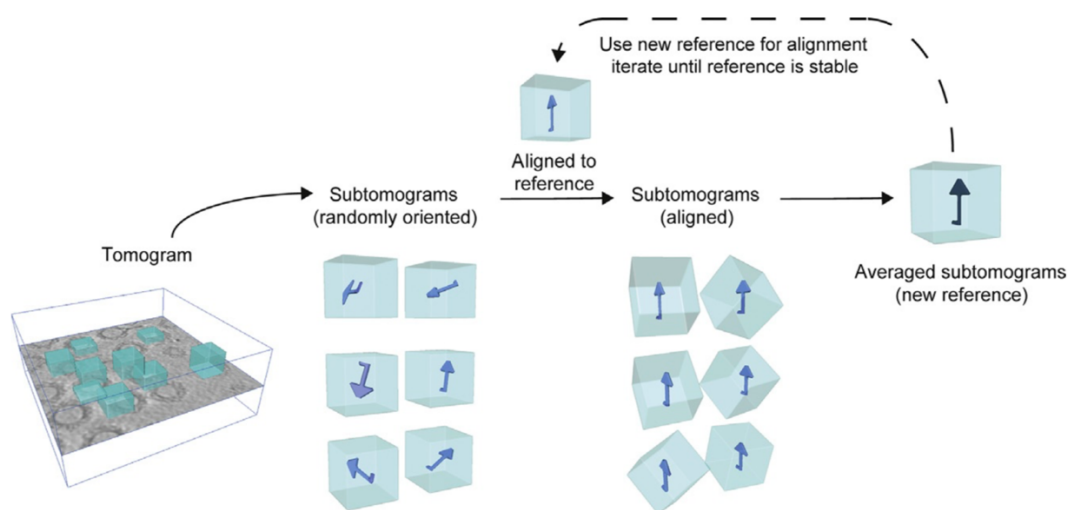


Figure 1.8. Overview of subtomogram averaging workflow. Identical macromolecules called subtomograms are picked and extracted from the full tomogram; each subtomogram is randomly oriented. Subtomograms are aligned to the reference and a new reference is generated from the aligned particles. This process is iterated until the alignment converges to a stable reference (adapted from *Wan et.al.* (Wan & Briggs, 2016)).

Due to the developments of hardware and software of cryo-EM, in recent years the number of structures solved by single-particle cryo-EM and subtomogram averaging surge and the attainable resolution becomes higher and higher (Figure 1.9). The resolution of structures solved by single-particle cryo-EM can often reach atomic level, which enables atomic model building. Single-particle cryo-EM requires purified sample

with high homogeneity, so far the highest resolution achieved by single-particle cryo-EM is 1.54 Å with a cold field emission gun (Takayuki Kato, 2019). The resolution of structures solved by subtomogram averaging is usually lower than that of single-particle cryo-EM, which needs combination of high resolution crystal or single-particle or NMR structures of the individual components of the biological sample to interpret the entire subtomogram averaging density map. However, subtomogram averaging has the advantage to investigate the structures of biological samples in their native environments, in which the structure and function of the biological sample can be well preserved.

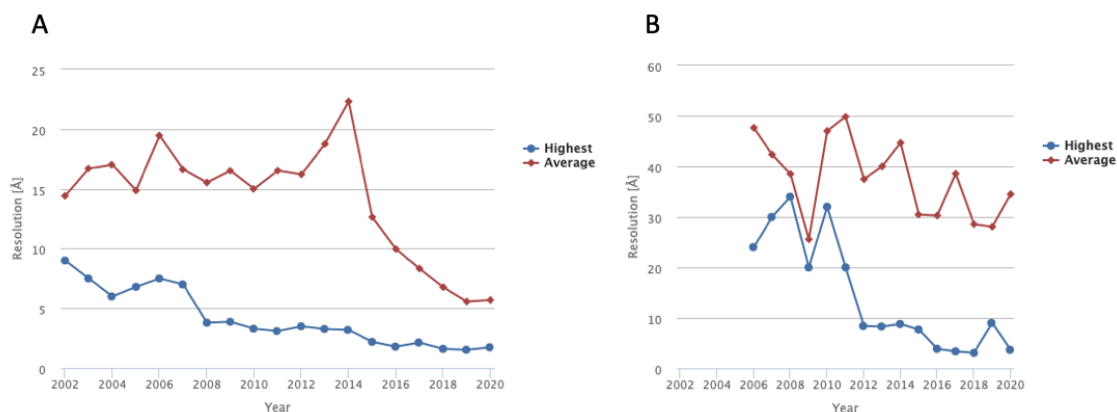


Figure 1.9. A: Resolution trends for single-particle analysis; B: Resolution trends for subtomogram averaging. (Figures were downloaded from ebi.ac.uk)

Chapter 2: Structures of RyR1 in native membranes

2.1 Introduction into the role of RyR1 in excitation-contraction coupling

In muscle cells excitation-contraction coupling (E-C coupling) is the physiological process of converting electrical impulse to mechanical response of muscle fiber, which plays an important role for many life processes such as heart beating. Two kinds of vital Ca^{2+} channels are involved in excitation-contraction coupling, namely RyR1 on the membrane of SR and dihydropyridine receptor (DHPR, also known as one of the L-type voltage-gated Ca^{2+} channels) on the membrane of transverse tubule (T-tubule) (Rios & Brum, 1987). In the process of E-C coupling, the action potential originated from motor neuron propagates along plasma membrane to T-tubule to activate DHPR, and the activated DHPR stimulates opening of RyRs on the SR membrane to release Ca^{2+} from SR lumen to cytoplasm, triggering muscle contraction (Rios & Pizarro, 1991, Schneider, 1994). In muscle cells, the region where T-tubule flanked by two SR forms triad junction (Figure 2.1.1a), which plays a pivotal role in excitation and contraction coupling (E-C coupling) of muscle (Barone, Randazzo et al., 2015). Freeze-fracture EM experiments suggested that every other RyR interacts with four DHPRs to form super-complex called Ca^{2+} -releasing unit (Protasi, 2002) (Figure 2.1.1b).

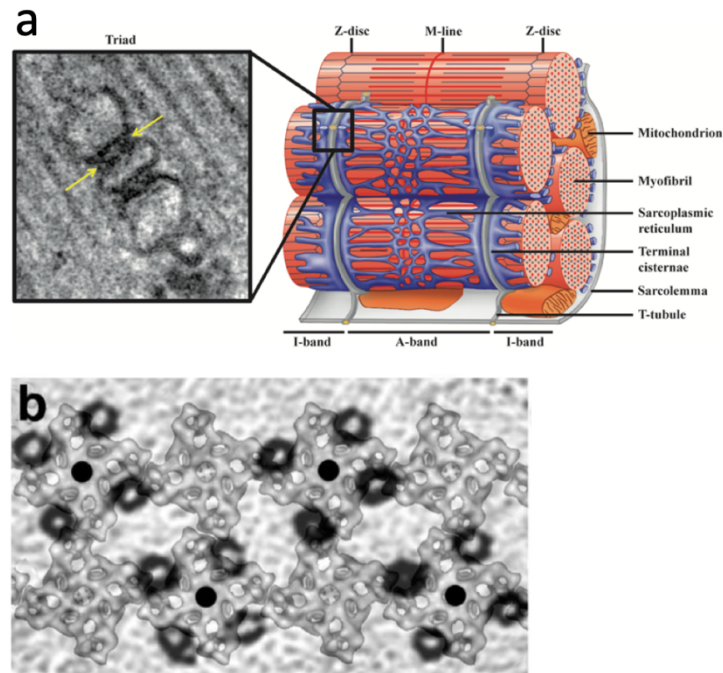


Figure 2.1.1. Composition and model of triad junction. a: Triad junction in skeletal muscle (from Al-Qusairi *et al.* (Al-Qusairi & Laporte, 2011)). The left electron micrograph of a triad junction and its corresponding schematic representation from skeletal muscle cell. The T-tubule is flanked on both sides by a terminal cisternae of the sarcoplasmic reticulum. b: Overlay of the DHPR tetrad and the RyRs array which is revealed by freeze-fracture technique (from Paolini *et al.* (Paolini, Protasi *et al.*, 2004)), showing that four DHPRs are bound to every other RyR.

RyRs were named after their antagonist ryanodine, which is a compound extracted from the south American plant *Ryania speciosa* and can bind open RyRs to lock them in the open state at nanomolar concentrations (Franzini.C, 1970). RyRs are homotetramers and have molecular weights of more than 2.2 MDa and are the largest known ion channels to date, which are responsible for releasing Ca^{2+} from the lumen of SR into cytoplasm, thus triggering muscle fiber contraction (Inui, Saito *et al.*, 1987, Lai, Erickson *et al.*, 1988). RyRs comprise an ion-conductive pore in the transmembrane region and a giant N-terminal domain in the cytoplasmic region that consists of about 70% of the whole molecular weight. In mammals, RyRs have three isoforms (RyR1-3). RyR1 is expressed in

skeletal muscle cells and was the first cloned isoform (Takeshima, Nishimura et al., 1989, Zorzato, Fujii et al., 1990), RyR2 is primarily expressed in cardiac muscle cells (Nakai, Imagawa et al., 1990, Otsu, Willard et al., 1990) and RyR3 was first identified in the brain (Hakamata, Nakai et al., 1992). Those three isoforms share sequences identity of approximately 65% (Lanner, Georgiou et al., 2010), the biggest different regions lie in three segments throughout the gene sequence, which are called D1 (residues 4254-4631), D2 (residues 1342-1403) and D3 (residues 1872-1923) of RyR1. Lower organisms such as lobster and fruit flies express a single RyR isoform. In addition, two RyR isoforms, RyR α and RyR β were found to be expressed in non-mammalian vertebrates (Lanner et al., 2010). Besides the main trigger Ca^{2+} , the opening activity of RyRs are regulated by other regulatory proteins such as DHPR, calmodulin (CaM), S100A1, triadin, junctin and so on, cation ions such as Mg^{2+} , small molecules such as caffeine, ATP and ryanodine and so on, hence the activity regulation of RyR1 is very diverse (Witherspoon & Meilleur, 2016).

RyRs were initially visualized by negative stain electron microscopy in the studies of muscle ultrastructure. RyRs were shown to be “feet-like” electron dense protrusions spanning the intracellular junctions between the terminal cisternae of sarcoplasmic reticulum (SR) and transverse tubular (T-tubule) formed by the invaginations of plasma membrane (Franzini.C, 1970). Those “feet-like” protrusions were later purified *in vitro* and proved to be RyRs (Inui et al., 1987, Lai et al., 1988) (Figure 2.1.2).

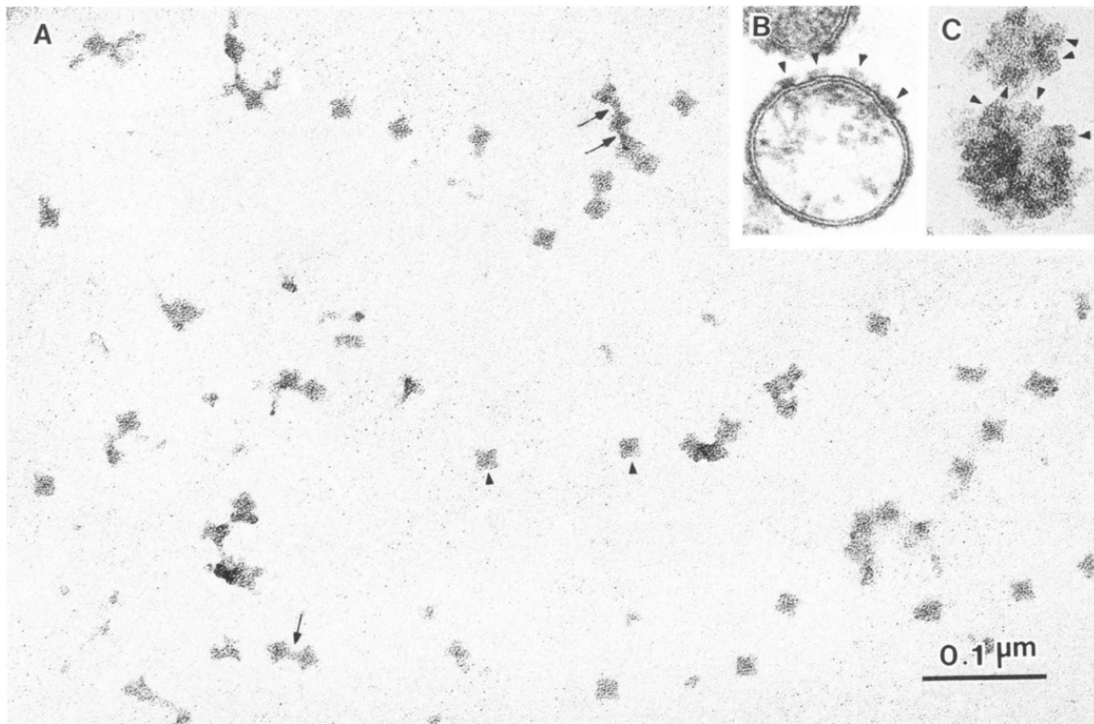


Figure 2.1.2. The morphology of the purified RyR (A) and the feet structures of terminal cisternae of SR (B and C). A, negative staining electron microscopy of the purified RyR. The purified RyR shows square shape of about 210 Å (arrowheads). B and C, thin sections of terminal cisternae of SR. The feet structures are observed in thin section in cross-section (B) and in tangential section (C). The square shape of the feet is observed (arrowheads) in the tangential sections. (adapted from *Inui et al.* (Inui et al., 1987))

RyR1 located in skeletal muscle is the subtype of ryanodine receptor that has been studied the most. RyR1 has been visualized in native toadfish and zebrafish muscles (Wagenknecht, Hsieh et al., 2015) and the structure of the receptor in purified native muscle membranes has been reported at a resolution of 71 Å (Renken, Hsieh et al., 2009). More recently, due to the development of cryo-electron microscopy technology, the sub-5-Å (Zalk, Clarke et al., 2015) and sub-4-Å (Yan, Bai et al., 2015) resolution structures of RyR1 in apo state (Figure 2.1.3), as well as the structures in nanodiscs in closed and partially open states (Efremov, Leitner et al., 2015)

have been reported. Des Georges and colleagues (des Georges, Clarke et al., 2016) determined a series of approximately 4-Å reconstructions of RyR1 that allowed building atomic models. The authors proposed an activation sequence: first Ca^{2+} or ATP “prime” the channel for opening stabilizing the conformation of the channel in the configuration permissive for opening. Then a combination of three ligands, Ca^{2+} , caffeine, and ATP, open the channel of the purified receptor (des Georges et al., 2016). Alternatively, Ca^{2+} and ryanodine lock the channel in an open state (des Georges et al., 2016) (Figure 2.1.4). Conformational changes from the ligand binding sites are transmitted to the pore several nanometers away via the central domain (Bai, Yan et al., 2016b), and computational analysis suggests multiple routes by which ligand binding leads to channel activation (des Georges et al., 2016). However, there are significant differences between activation of RyR1 *in vitro* and *in vivo*. Transition between closed and open conformations of RyR1 *in vitro* is sensitive to applied detergents which favor closed state (Willegems & Efremov, 2018) and is generally modulated by a large number of small molecules (Hwang, Zorzato et al., 2012, Witherspoon & Meilleur, 2016) which were only partially present in the purified receptors analyzed by single particle cryo-EM.

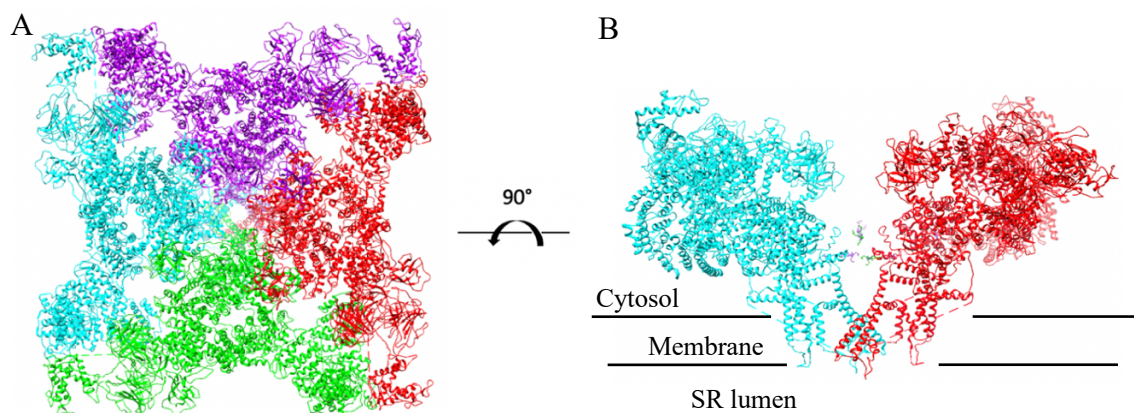


Figure 2.1.3. An atomic model derived from single particle cryo-EM structures of RyR1 (des Georges et al., 2016) in closed state as representative of RyRs, EMDB: 5taw. A: the top view, each monomer is shown in different color. B: the side view, only two monomers are shown for clarity.

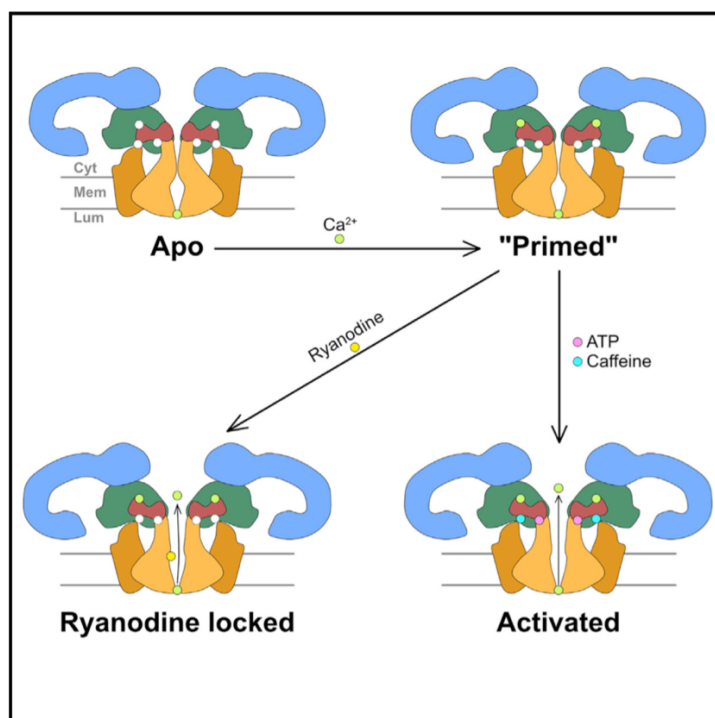


Figure 2.1.4. Schematic representation of RyR1 activation and pore opening. Apo: RyR1 is under 5 mM EGTA and in closed state; Primed: RyR1 is under 30 μM Ca²⁺; Activated: “primed” RyR1 is under 2 mM ATP and 5 mM caffeine and in activated and open state; “primed” RyR1 is under 10 μM ryanodine and in open-locked state (adapted from *des Georges* and colleagues (des Georges et al., 2016)).

In this chapter I performed structural analysis of RyR1 in native SR membranes. For this I isolated SR from rabbit skeletal muscle and collected tomographic images of the SR with cryo-EM and solved the structures of RyR1 in closed and open states by subtomogram averaging. The structure includes the native membrane which shows observable curvature, as well as several interacting protein densities that are not observed in the high-resolution cryo-EM structures of purified receptor.

Our analysis reveals the most probable conformations of RyR1 *in situ* and decomposes the structural variation of RyR1 *in situ* into principal components. Upon activation by Ca^{2+} and ryanodine, conformational changes in RyR1 lead to a drastic change in the curvature of the membrane, potentially contributing to the energetics of channel opening and closing.

2.2 Methods

2.2.1 Biochemical sample preparation

SR vesicles were isolated based on the previously described protocol (Mitchell, Palade et al., 1983). Briefly, 60 g of fresh rabbit skeletal muscle tissue from the hind leg and back was ground using a meat grinder, and then homogenized using a blender with 300 mL of homogenization buffer (0.5 mM EDTA, 10% sucrose, 20 mM $\text{Na}_4\text{O}_7\text{P}_2$, 20 mM NaH_2PO_4 , and 1 mM MgCl_2 , pH 7.1) plus the following protease inhibitors: 2.6 $\mu\text{g}/\text{ml}$ aprotinin, 1.4 $\mu\text{g}/\text{ml}$ pepstatin, and 10 $\mu\text{g}/\text{ml}$ leupeptin. Homogenates derived from a total of 180 g of muscle were centrifuged in a Beckman Coulter rotor JLA-16.250 fixed-angle rotor at 8,900 x g at 4°C for 20 min. The resulting supernatant was filtered through cheesecloth and then ultra-centrifuged in a Beckman Coulter Type 45Ti fixed-angle rotor at a speed of 20,000 x g at 4°C for 1 h. The membrane pellets were divided into 20 aliquots. One aliquot was used immediately in the next step and the remaining aliquots were stored at -80°C for future use. The membrane pellet fraction was subjected to a discontinuous sucrose gradient with steps of 0.15 mL 50%, 1.27 mL 36%, 1.27 mL 34%, 1.58 mL 32%, 1.58 mL 28%, 3.8 mL 25%, and 1.27 mL 14% sucrose. The sucrose gradient was then centrifuged in a Beckman Coulter SW40Ti swinging-bucket rotor at 96 200 x g for 90 min. Bands at the interface of the 25% and 28% sucrose phases and at the band at the interface of the 28% and 32% sucrose phases

were confirmed to contain RyR1 by western blot. These bands were extracted from the sucrose gradient, further diluted with a dilution buffer (0.5 mM EDTA, 20 mM Na₄O₇P₂, 20 mM NaH₂PO₄, and 1 mM MgCl₂, pH 7.1) to 4 mL, and then ultra-centrifuged in a Beckman Coulter TLA 100.4 fixed-angle rotor at a speed of 40 000 x g at 4°C for 20 min. The final membrane pellet was resuspended with 1 mL of dilution buffer. For RyR1 in the presumably closed state, this suspension was used directly for cryo-EM grid preparation. For RyR1 in the presumably open state, this suspension was dialyzed against dialysis buffer (20mM sodium pyrophosphate, 20mM NaH₂PO₄, pH7.1) overnight at 4°C, and then Ca²⁺ was added to the sample to a final concentration of 0.3 mM Ca²⁺. The mixture was incubated at room temperature for 20 min before ryanodine was added to a final concentration of 10 μM. This final mixture was incubated overnight at 4°C and then used for cryo-EM grid preparation.

2.2.2 Cryo-EM grid preparation and tomographic data collection

Grids were frozen for cryo-EM using a Vitrobot™ Mark IV (Thermo Fisher). 3 μL of the sample mixed with 10-nm colloidal gold fiducials was applied to a 300-mesh gold Quantifoil® R 2/2 grid with gold support. The grid was blotted with Whatman® No. 1 filter paper and plunged into liquid ethane cooled to liquid nitrogen temperature. Imaging was performed on a Thermo Fisher Titan Krios operated at 300 kV equipped with a Gatan K2 Summit® direct electron detector and a Gatan Quantum® energy filter. Single-axis tilt series (-60° to +60°) were collected using a dose-symmetric tilt-scheme (Hagen, Wan et al., 2017) with 3° intervals implemented in SerialEM (Mastrorade, 2005). The electron dose for the untilted image was increased to 18 e-/Å², with all the remaining projections receiving a dose of 1.1 e-/Å² recorded in five frames; the total exposure was about 62 e-/Å². Images were recorded at a magnification of 53000x, resulting in a

pixel size of 2.7 Å/pixel. Nominal defocus was set between 4 μm and 5 μm.

2.2.3 Image processing

Per-tilt motion correction was performed using MotionCor2 (Zheng, Palovcak et al., 2017), defocus estimation was performed using Gctf for each projection (Zhang, 2016). The tomographic tilt series were aligned using the 10-nm gold fiducials in IMOD (Kremer, Mastronarde et al., 1996). Tomographic reconstructions were generated by weighted back-projection implemented in IMOD (Kremer et al., 1996). Nonlinear anisotropic diffusion filtering (Frangakis & Hegerl, 2001) was performed to aid particle picking in binned tomograms and display in the figures. Subtomogram positions were picked manually with IMOD and extracted to 200 x 200 x 200 voxels boxes from unbinned contrast transfer function (CTF)-corrected tomograms using the dtcrop function in Dynamo (Castano-Diez, Kudryashev et al., 2012). Initial alignment was done manually with the dynamo_gallery followed by constrained refinement of shifts and angles using the Dynamo alignment dcp workflow. C4 symmetry was applied. Initial classification by multi-reference alignment was used to remove bad particles, after which independent half-set refinement was performed for the datasets containing over 500 particles as previously described (Castano-Diez, Kudryashev et al., 2017). For the datasets containing less than 501 particles, the frequency ranges of the resulting reconstructions were restricted to 36 Å which was much lower than the final resolution values. The final reconstructions were produced by taking into consideration dose-dependent resolution decay for each particle, and the contribution of each of the particle to the final average was proportional to the particle's cross-correlation to a reference. The

resolution was determined by *dynamo_fsc*; local resolution and locally filtered maps were generated using Relion 2.0 (Kimanius et al., 2016).

For the classification in Figure 2.3.4.1D we extracted the four asymmetric subboxes from each RyR1 particle, generated the alignment parameters to bring them to a common average using the *dynamo_data_subboxing* routine (Castano-Diez et al., 2017). We further generated an ellipsoidal mask around the area of interest and performed a multireference classification with restricted refinement till convergence. The class averages were reconstructed by taking into consideration dose-dependent resolution decay for each particle, and the contribution of each of the particle to the final average was proportional to the particle's cross-correlation to a reference.

2.2.4 Analysis of conformational heterogeneity

We used Dynamo to perform multi-reference alignment and classification of our final dataset into fifty classes using frequencies up to 22 Å and with the applying C4 symmetry. From these fifty classes, we excluded fourteen classes which had low particle abundance or included other confounding features, such as gold beads. We mutually aligned the remaining 36 classes, containing a total of 2105 particles, to a common average and performed eigen volume analysis by principal component analysis (PCA). At this step all 36 volumes were fully sampled in Fourier space therefore no accounting for the missing wedge was needed. The classes, or half-maps were generated by dividing the 36 particles into equal-sized groups according to their eigencoefficients, and these groups are presented in Figure 16C, Figure 22. The first principal component was trivial, therefore, the reported modes are enumerated starting from the second principal component. The informativity of the classes presented in Figure 21D is the covariance along the corresponding eigenvector. It is the result of the PCA

procedure implemented in *dynamo_ccmartix_analyze* and is presented in arbitrary units with the covariance of the first mode set to 1.

2.3 Results: structure of RyR1 in native membranes

2.3.1 Isolation of SR by sucrose gradient centrifugation

As it is described in the methods, the workflow of solving the structure of RyR1 *in situ* can be summarized in Figure 2.3.1.1A. The fresh rabbit skeletal muscle from the hind leg and back are homogenized, membranes can be collected through ultra-centrifugation, then SR vesicles are extracted from the membranes through sucrose gradient centrifugation, tomographic data of the SR vesicles are collected and subtomogram averaging of RyR1 on the SR vesicles is performed to generate the structure of RyR1 *in situ*. As for SR vesicles extraction, the homogenized skeletal muscle membrane aliquot was applied to the sucrose gradient centrifugation. Four thick bands were visible in the interfaces between sucrose gradients, each band was taken out from up to down by pipette and named fraction 1, fraction 2, fraction 3 and fraction 4, respectively (Figure 2.3.1.1B). Each fraction was checked with NS-EM, fraction 1 and 2 contained potential SR and was further confirmed by western blot against RyR1.

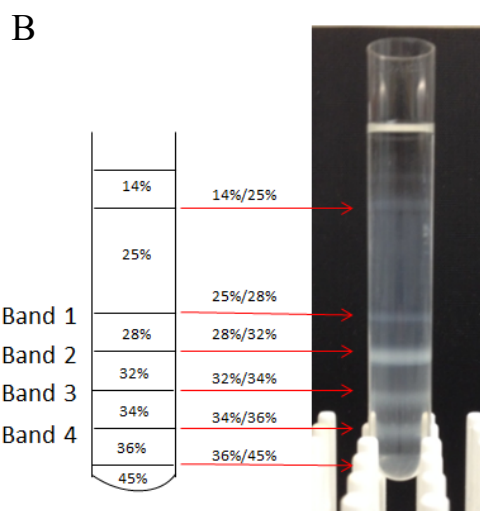
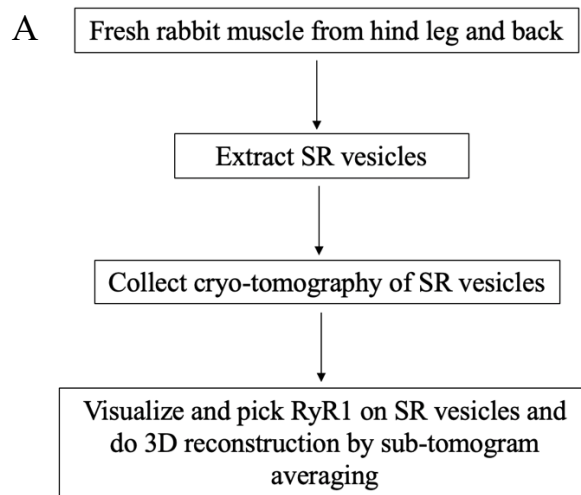


Figure 2.3.1.1. Sample preparation. A: The workflow of doing this project. SR vesicles are extracted from fresh rabbit muscle from hind legs and back, then tomographic data of SR vesicles are collected and sub-tomogram averaging of RyR1 on SR vesicles are performed to obtain its structure. B: The separation of SR vesicles by sucrose gradient centrifugation, which yielded four thick bands marked as band 1, 2, 3, 4, which are at the interface between 25% and 28%, 28% and 32%, 32% and 34%, 34% and 36% sucrose, respectively.

2.3.2 SR imaged by cryo-EM

Fraction 2 was used to freeze cryo-EM grids and further checked by Titan Krios. Triad junctions composed of one T-tubule flanked by two SR vesicles were seen and one of them was shown as an example (Figure

2.3.2.1). Tilt-series of triad junctions was collected and reconstructed into 3D tomogram. RyR1 particles can be recognized easily on the SR membrane in the 3D tomogram due to the giant size of RyR1 and its characteristic shape, as indicated by the red circles. In addition, RyR1 can also be observed in a similar way on the isolated SR instead of the SR in the triad junctions. It is noteworthy that inside the SR lumen higher protein density was observed in the vicinity of RyR1 compared to other areas.

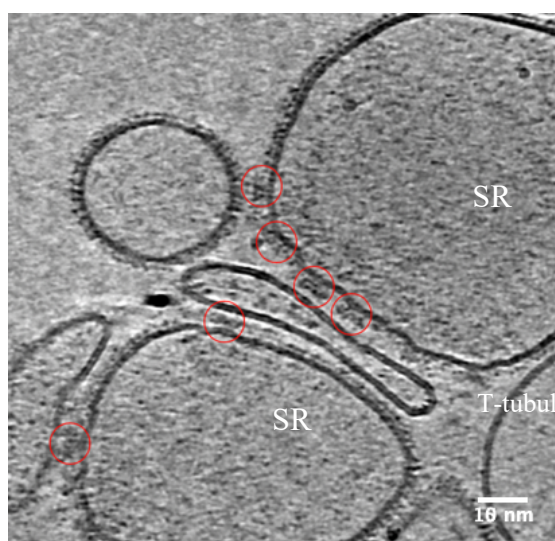


Figure 2.3.2.1. A slice through a low-pass filtered tomogram showing SR vesicles in contact with a putative T-tubule. Individual RyR1 molecules on the SR vesicles are indicated by the red circles.

2.3.3 Structures of RyR1

To ensure that RyR1 was in an environment without Ca^{2+} and thus in a closed state, I added EDTA to the SR vesicles resuspension to deplete Ca^{2+} . Cryo-grids of SR vesicles were frozen and 97 tilt-series of SR vesicles on Titan Krios were collected, those tilt-series were motion-corrected, aligned, CTF-corrected to generate tomograms. Due to the huge size of RyR1 and its unique shape which was known from previous literatures, RyR1 in native SR membranes could be easily recognized and 3,118 particles were manually picked. Out of the all particles 256 had an observable adjacent

T-tubule-like membrane density. From this subset of particles, we generated an asymmetric reconstruction that showed C4 symmetry, which we applied for further refinement. The final structure had a resolution of 38 Å (Figure 2.3.3.1C). Unexpectedly, we could not detect an ordered density attributable to DHPR on the T-tubule membrane, which was expected to be distinguishable at such resolution. As RyR1 without the T-tubule membrane was more commonly observed, we therefore performed StA on all the available particles. An asymmetric reconstruction of a dataset consisting of the best 2574 receptors resulted in C4 symmetry, and we therefore applied C4 symmetry for the subsequent alignment and reconstruction. As a consequence, all the features in the maps are C4 symmetric unless otherwise stated. The global resolution of the resulting structure is 12.6 Å (Figure 2.3.3.1E). Local resolution is higher in the central domain, suggesting bigger flexibility in the peripheral domains (Figure 2.3.3.1D). Overall, the *in situ* structure resembles the reported single particle cryo-EM reconstructions of purified RyR1, particularly in its cytoplasmic domain (Figure 2.3.3.1A and 2.3.3.2)(Bai et al., 2016b, des Georges et al., 2016, Efremov et al., 2015, Samso, Feng et al., 2009, Wagenknecht, Grassucci et al., 1989, Wei, Wang et al., 2016a, Yan et al., 2015, Zalk et al., 2015). In addition, apparent membrane curvature is observed in the *in situ* structure which was absent in the single particle structure (Figure 2.3.3.1B and 2.3.3.2).

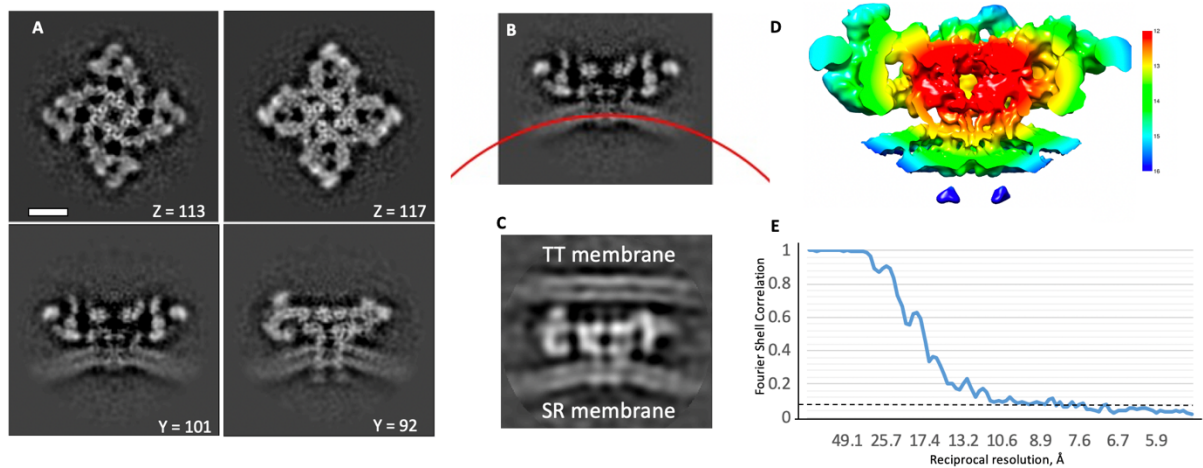


Figure 2.3.3.1. Structure of RyR1 *in situ* in the apo state. A) Slices through the *in situ* average map of RyR1 in the apo state from the XY and XZ directions. Scale bar: 10 nm. Please note that just by observing from different directions the apparent curvature in the same structure may change. Therefore, it is critical to compare the curvature either at the same section or in sections traversing the middle of the particle. B) Measurement of the membrane curvature in the average structure. C) Slice through the *in situ* average map of RyR1 in adjacent with TT membrane. D) Resolution measurement of the structure in apo state by Fourier shell correlation between independently processed half-maps. E) Heat-map of the local resolution of the structure with resolutions indicated by the accompanying colorimetric key. (Figure prepared together with Dr. Misha Kudryashev)

The *in situ* density map of RyR1 present three distinguishable regions, which are the giant cytoplasmic region, SR membrane and the density inside the SR lumen. Interestingly, the SR membrane and density in the SR lumen were not observed in the published high resolution structures of purified RyR1 by single particle cryo-EM due to the lack of native environment. The single particle structure of RyR1 in closed state (5TB2) can be best fitted into the *in situ* density map (Figure 2.3.3.2).

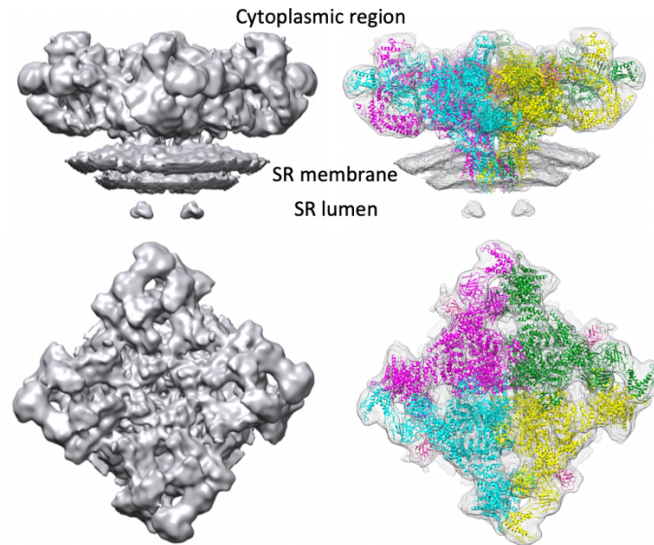


Figure 2.3.3.2. Volume-rendered visualizations of the average structure of RyR1 at 12.6 Å resolution (left) shown in side and top view, and with the atomic model of RyR1 (PDB: 5TB2) fitted (right). There are three regions in the structure: cytoplasmic region, SR membrane and SR lumen.

By comparing to all the published structures of RyR1, we found that one of the previously reported single particle structures of the purified RyR1 in the closed apo state, EMD-8393, namely one of the multiple classes obtained at the same time (des Georges et al., 2016), is most similar to my *in situ* structure based on both Fourier shell correlation (Figure 2.3.3.3) and visual analysis of the rigid body fitting of the corresponding atomic model (PDB: 5TB2). This suggests that the captured conformation of my structure represents a closed apo state (apoRyR1) and we have therefore used the atomic model 5TB2 for further analysis in the following. In addition, we found that the *in situ* structure has an additional density on the cytoplasmic region, which was absent in all the reported single particle structures (Figure 2.3.3.3, indicated by the red circles).

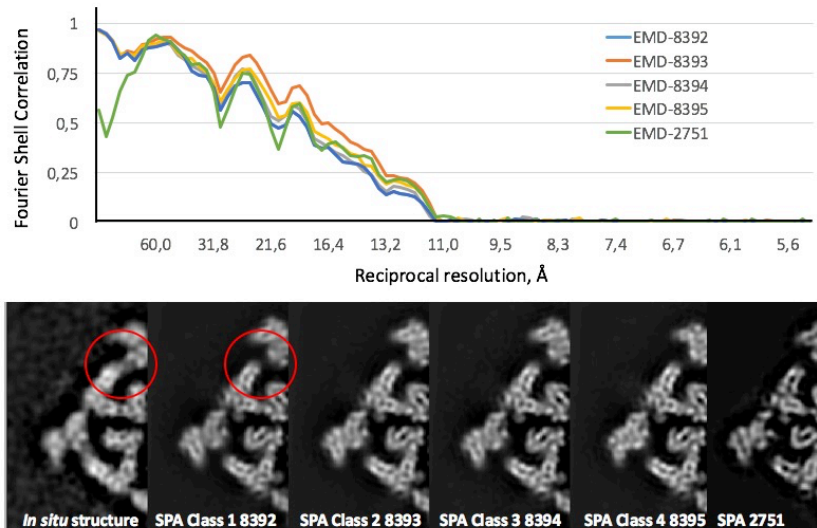


Figure 2.3.3.3. Structural similarities between the *in situ* structure and previously reported high-resolution structures of purified RyRs. Top: Fourier shell correlation between the mutually aligned *in situ* structure and the respective reconstructions of purified receptor by single particle cryo-EM (des Georges et al., 2016, Efremov et al., 2015). Bottom: slices through the *in situ* structure and the reported single particle cryo-EM structures of purified receptor filtered to 15 Å for comparison. Bridging density present in our *in situ* structure, but absent in the single-particle structures is circled in red.

Rigid-body fitting of the atomic model of RyR1 to the *in situ* density map reveals that all of the FKBP12 interaction sites are occupied (Figure 2.3.3.4). FKBP12 is a 12-kDa protein also named as FK506-binding protein, which is a kind of RyR accessory protein and regulates RyR-evoked Ca^{2+} release (MacMillan, Currie et al., 2008). FKBP12 was also used to pull down RyR1 during RyR1 purification (Yan et al., 2015). The *in situ* structure further confirmed that FKBP12 was bound to RyR1 in the native closed state.

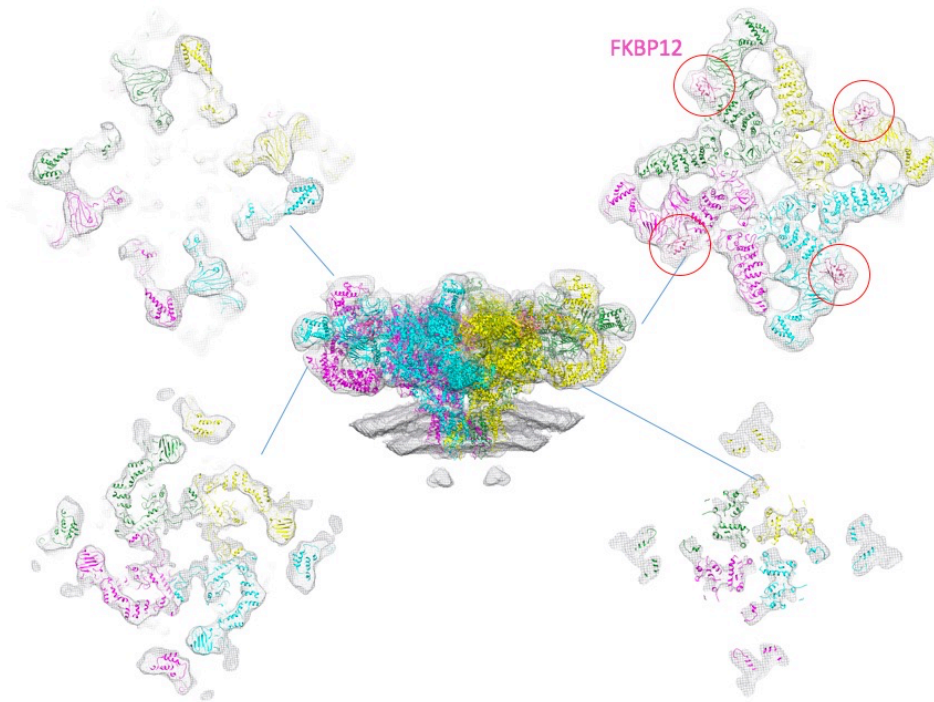


Figure 2.3.3.4. Rigid-body fitting of the atomic model 5TB2 into the *in situ* structure. Slices through the isosurface are presented perpendicular to the central panel at the heights indicated by the blue lines. FKBP12 is marked by red circles in the top-right panel.

Previous studies using freeze-fracture electron microscopy and focused ion beam (FIB) milling and cryo-electron tomography report RyR1 forms a loosely ordered paracrystalline array (Renken et al., 2009, Wagenknecht et al., 2015). For our data, image classification of particles of RyR1 *in situ* revealed that out of 2547 particles, 960 showed a neighboring density, which corresponds to the T-tubule membrane. Of these, 242 resulted in the most ordered arrangement, which was reported previously but at lower resolutions. Rigid-body fitting of the RyR1 atomic model (PDB:5TIB) into the resulting density arrays suggests that inter-receptor interactions may be modulated by bridging solenoids. The closest contacts between the fitted atomic models occur between corresponding helices 2950-2976, 3126-

3143, 3140-3163, 3199-3212 and 3241-3254 of the neighboring RyR1 tetramers (Figure 2.3.3.5).

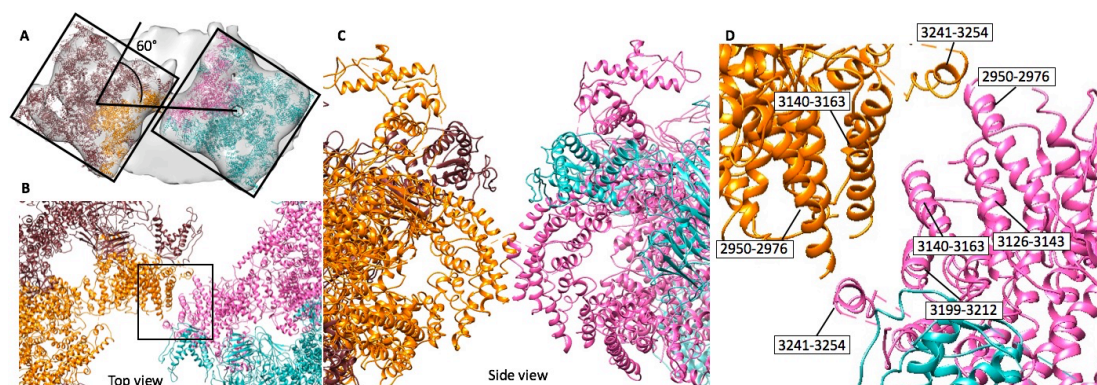


Figure 2.3.3.5. Putative inter-protomer interactions between RyR1 tetramers in native membranes. A) A subtomogram average map of two neighboring apo RyR1 tetramers with the atomic model 5TIB fitted twice. B, C) Top and side views of the interacting domains of the atomic models. D) An enlarged version of the area boxed in panel B with the residue numbers of the putative interaction helices labelled. (Figure prepared together with Dr. Misha Kudryashev)

2.3.4 An unaccommodated density in the cytoplasmic domain

The map of apo closed RyR1 *in situ* also shows density that, based on the fitting of the atomic model, corresponds to residues 3613-3639 of the RyR1 protomer (Figure 2.3.4.1A). This density is not present in the reported high resolution single particle cryo-EM maps of purified RyR1 (Figure 2.3.4.1B), and consequently it is not included in the existing atomic models of RyR1 (Figure 2.3.4.1A-C) (Bai, Yan et al., 2016a, des Georges et al., 2016, Efremov et al., 2015, Wei et al., 2016a, Yan et al., 2015, Zalk et al., 2015). The missing residues at this location have been previously shown to be the CaM binding site for which S100A1 also competes to bind (Prosser, Wright et al., 2008). CaM is an approximately 17-kDa protein that switches between being a partial agonist of RyR1 as apoCaM and an antagonist upon Ca²⁺ binding (Wagenknecht, Berkowitz et al., 1994), while S100A1 is an approximately 10-kDa RyR1 agonist

(Wright, Prosser et al., 2008). However, at the current resolution we can not clearly identify the origin of the observed density. Alternatively, the density corresponding to the missing residues and the nearby lobes may be more ordered in situ compared to the structure of purified RyR1. In addition, focused asymmetric classification centered on the area of interest revealed that all the resulting classes had this density (Figure 2.3.4.1D). However, in the fourth class, the apparent density was smaller, possibly corresponding to an unoccupied site, *i.e.*, residues 3613-3639 without an allosteric modulator bound, while the three other classes had larger density similar to the original global average, suggesting that this larger density results from additional bound protein(s).

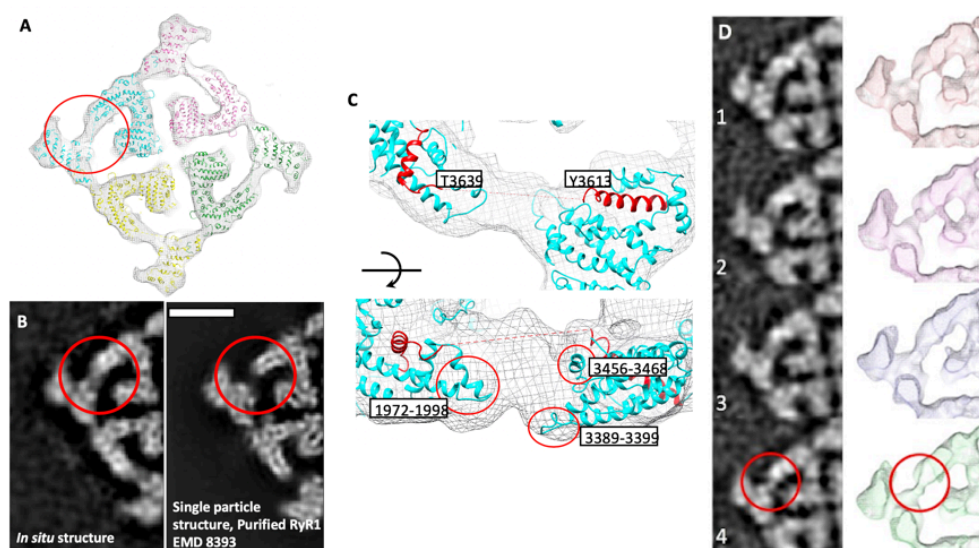


Figure 2.3.4.1. The unaccommodated density in the cytoplasmic domain. A, B: The location of the unaccommodated density is marked with red circles on a volume-rendered representation fitted with an atomic model (PDB: 5TB2) (A) and in slices through maps of the in-situ structure (B, left) and the single particle structure (EMDB: 8393) filtered to 15 Å (B, right). Scale bar: 10 nm. C: The *in situ* structure with an atomic model (PDB: 5TB2) fitted. Red circles are sites of potential interaction between RyR1 and other regulatory proteins. D: Classification focused on the binding site shows both full (classes 1-3) or partial (class 4) occupancy of the binding site. Classes are

depicted as slices through the maps and as volume rendered representations. The narrower density observed in class 4 is highlighted by a red circle.

2.3.5 The helix-like density in the SR membrane

Further examination of the *in situ* RyR1 structure revealed a defined helix-like density inside the SR membrane, which is visible approximately 5 nm from the edge of the transmembrane domain of RyR1 (Figure 2.3.5.1). The density snaps the inner and outer leaflets. We suggest that this density corresponds to an ordered transmembrane helix; however, at the current resolution, we cannot conclude if it is one helix or a few closely positioned helices.

Through reading literatures, we found that both the small RyR accessory proteins junctin and triadin have single predicted transmembrane helices and long disordered intra-SR domains, which are likely the helix-like density here, however we were unable to identify other distinct densities in the SR that could correspond to triadin or junctin at the current resolution, hence the observed ordered transmembrane density in the SR bilayer likely correspond to either triadin, junctin, or both.

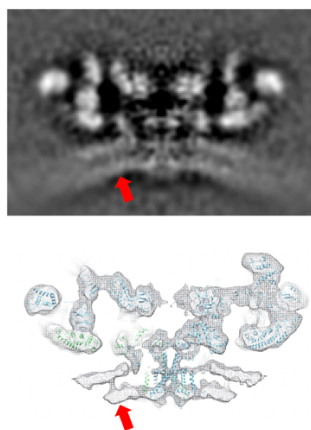


Figure 2.3.5.1. The slice through the *in situ* structure (top) and a thin slice through a volume-rendered representation of the structure with PDB 5TB2 fitted (bottom). The observed additional transmembrane density is indicated by the red arrow.

2.3.6 Interactions of RyR1 in the SR lumen

Inside the SR lumen, approximately 4-nm long extensions originating from the transmembrane domain of RyR1 can be observed (Figure 2.3.6.1A, B). The local resolution of these extensions is lower than that of the cytoplasmic domain of RyR1, suggesting lower local order or higher flexibility. Previously reported atomic models of purified RyR1 are missing the residues from A4340 in the cytoplasmic domain through to F4540 on the luminal side. However, we are able to observe density traversing the inner and outer leaflet of the SR bilayer in the vicinity of F4540 (Figure 2.3.6.1B), adjacent to the transmembrane density presented in Figure 2.3.5.1.

In previously published *in vitro* experiments, the Ca^{2+} -buffering protein calsequestrin 1 (CSQ1) located in the SR lumen was suggested to bind RyR1 via triadin and junctin at physiological Ca^{2+} concentrations (1mM), and disassociate from RyR1 at Ca^{2+} concentrations that are either lower ($\leq 1\text{mM}$) or higher ($\geq 4\text{mM}$) than physiological level (Beard, Wei et al., 2009). We therefore probed if the appearance of the SR extensions could be manipulated by variations in intra-SR calcium concentrations. To this end, we recorded tomograms of sample which had been depleted of Ca^{2+} (with 0.5 mM EDTA), were at physiological Ca^{2+} concentrations (1 mM), and were at high (5 mM) Ca^{2+} concentrations. In order to make the SR lumen accessible for Ca^{2+} supplementation, I added sub-CMC concentrations of n-Dodecyl-B-D-Maltoside detergent (DDM) to the SR resuspension to a final concentration of 0.005% (57.4% of the critical micelle concentration (CMC)) in order to gently destabilize the SR membrane, and equalize the concentration of Ca^{2+} inside and outside of the SR lumen. Tomographic data of SR vesicles from each of the conditions were collected and sub-tomogram averaging were performed, all of the

structures were similar and had intra-SR extensions (Figure 2.3.6.1E). We therefore concluded that most of the density in the sarcoplasmic extensions is not occupied by CSQ1 and likely corresponds to residues 4341-4540 of RyR1. In addition, segregation of protein density inside the SR lumen next to RyR1 was observed at physiological concentrations of Ca^{2+} and in our tomograms where no detergent was added, suggesting that the SR lumen has become accessible to Ca^{2+} after addition of detergent. Addition of detergent and depletion of Ca^{2+} by EDTA changed the appearance of the density inside the SR from primarily “segregated” to primarily “evenly distributed” (Figure 2.3.6.1C, D). Addition of 5mM of exogenous Ca^{2+} also resulted either in “evenly distributed” protein density or “empty” SR lumen (Figure 2.3.6.1C, D). Filamentous densities inside and outside of the SR vesicles (Figure 2.3.6.1C, rightmost panel) were observed in tomograms with 5mM Ca^{2+} , but not in the other conditions.

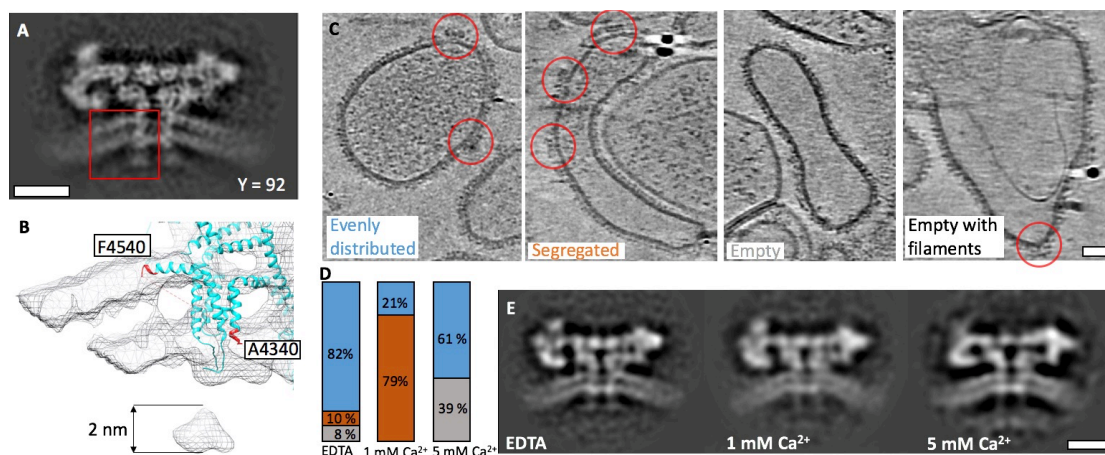


Figure 2.3.6.1. Intra-SR extensions of RyR1. A: A slice through the average structure of the apo-state at a different slice than Fig. 1C. The intra-SR extension density is boxed in red. B: A zoom into the corresponding volumetric density as the boxed area in (A), with the atomic model PDB 5TB2 fitted. C: Representative SR vesicles with different distributions of inner-SR density: evenly distributed, segregated, empty and empty with filaments inside. RyR1 particles are circled in red. D: The fractions of vesicles that fall into each density category for each RyR1 sample. Blue color corresponds to SR lumen showing evenly distributed density, orange to segregated

density, and grey to empty vesicles. The number of vesicles measurements for the 'EDTA' sample is 64, for '1mM Ca²⁺' sample is 32, for '5mM Ca²⁺' sample is 21. E: Structures of RyR1 determined in presence of increasing Ca²⁺ concentration (1 mM and 5 mM), still showing intra-SR extensions. Scale bars: 10 nm in (A) and I, 20 nm in (C).

2.3.7 Structural variation of the RyR1 domains in native membranes

Classification of the RyR1 particles into four distinct classes yielded one major class containing 45% of the particles, with the other classes less populated, namely 27%, 19%, and 10% of the particles, respectively (Figure 2.3.7.1A-C). Luminal extensions are apparent in all four classes (Figure 2.3.7.1C), suggesting that the majority of the particles have the corresponding density. Class 1 is most similar to the global average. The major difference between class 2 and class 1 is the downward movement of the AB-domain (ABD) and the outward rotation of the peripheral domains. The major differences between the classes 3 and 1 is the outward movement of the N-terminal solenoid towards the SPRY3 domain; this rotation was accompanied by a rotation of the Ry1-2 domain. While classes 1-3 all had similar membrane curvature, the membrane curvature in class 4 is less pronounced, and class 4 also shows the Nsol and SPRY3 domains extending in the cytoplasmic direction.

In order to further understand the structural variation of RyR1 present in the data, we made use of principal component analysis inspired by Dashiti and colleagues (Dashti, Schwander et al., 2014) and by Haselbach and colleagues (Haselbach, Schrader et al., 2017). Briefly, we performed multireference classification with alignment into a large number (50) of classes and then executed a principal component analysis on the result (see Methods). This analysis resulted, by definition, in multiple uncorrelated modes, ordered by the variance encapsulated within the mode. For

example, mode 1 is defined as that encoding the greatest variance and is therefore more informative than mode 5 (Figure 2.3.7.1E). Dividing the data into half-sets along the eigenvector of each mode and comparing the resulting averages revealed the principal movements of apoRyR1 (Figure 2.3.7.1D):

Mode 1: global movement of the central domains in the direction of the membrane with associated upwards rotational movement of the peripheral domains of the receptor. This mode also includes movement of the N-terminal solenoid towards the SPRY3 domain.

Mode 2 (71% of variance compared to the mode 1): an increase in the distance between the leaflets of the bilayer around the transmembrane domain of RyR1 is associated with minor movements of SPRY3 towards the symmetry axis and the bridging solenoid away from the symmetry axis.

Mode 3 (49% of variance compared to the mode 1): movement of the inner domains upwards along the central axis of the receptor coupled with a lower amplitude movement by the membrane in the same direction.

Mode 4 (42% of variance compared to the mode 1): vertical stretch of the cytoplasmic part receptor away from the membrane coupled to displacement of the intra-SR extensions away from the symmetry axis.

Mode 5 (36% of variance compared to the mode 1): an outward twist of the cytoplasmic domains associated with an increase in membrane curvature.

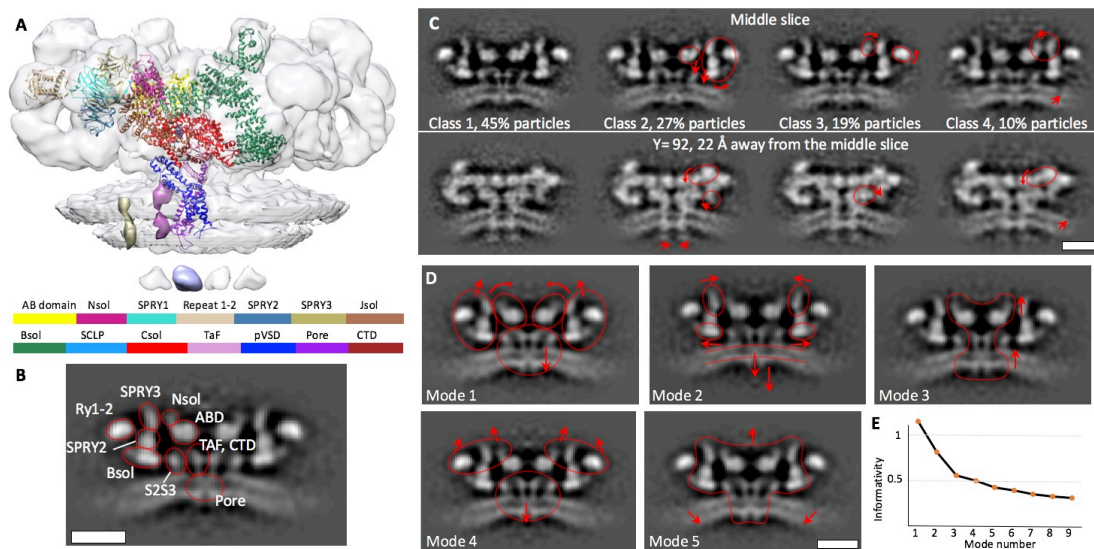


Figure 2.3.7.1. Structural heterogeneity of RyR1 *in situ*. A,B: The domains definition displayed on the *in-situ* structure, the updated from (Yan et al., 2015) is presented in Table 1. A is a volume-rendered representation with an atomic model, B is domain representation on the grayscale image. Please note the location of two transmembrane densities: yellow – shown in Figure 2.3.5.1, magenta – shown in Figure 2.3.6.1B. B: Slices through the results of classification of the particles in the global average into 4 classes at resolutions 15.4, 18, 18, and 27 Å, respectively, with the percentages of the total particles in each class shown beneath. Red arrows show domain movements compared to class 1. C: The first five modes of correlated movements. Direction of motion is indicated by the arrows. D: Informativity of the respective modes measured as variance of the corresponding mode divided by variance of the first mode. Scale bars: 10 nm. (Figure prepared together with Dr. Misha Kudryashev)

2.3.8 Activation of RyR1 in native membranes

We further solved the structure of open RyR1 in the presence of 0.3 mM Ca^{2+} and 10 μM ryanodine in a similar method, it was previously reported that 0.3 mM Ca^{2+} activate and open RyR1 and 10 μM ryanodine lock the receptor in the open state (des Georges et al., 2016). The structure was determined by cryo electron tomography and StA with 890 particles and a structure with a global resolution of 17.5 Å was obtained (Figure 2.3.8.1).

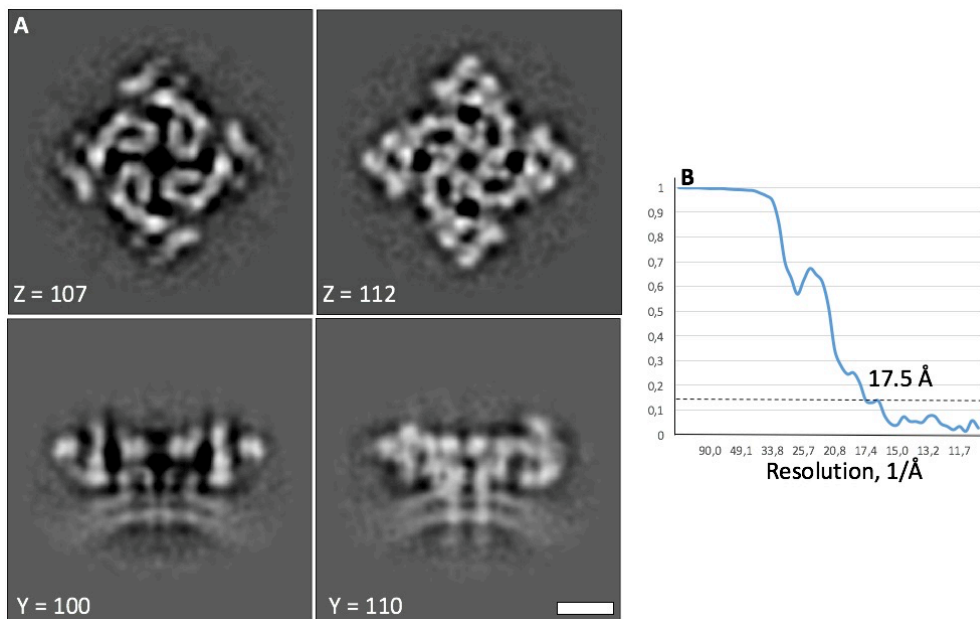


Figure 2.3.8.1. Structure of RyR1 in the presence of Ca^{2+} and ryanodine. A: Slices through the structure with the locations of the sections indicated by the Y or Z coordinates. Scale bar: 10 nm. B: Fourier shell correlation between independently refined half-sets indicates the resolution of the reconstruction is 17.5 Å.

When compared to apoRyR1, the structure of RyR1 in the presence of Ca^{2+} and ryanodine, which we refer to as ryRyR1, shows movement of the outer domains of RyR1 down towards the SR membrane (Figure 2.3.8.2A-B). In the previously reported single particle structures of purified receptor (des Georges et al., 2016, Efremov et al., 2015, Samsó et al., 2009), similar conformational changes were suggested to be associated with the opening of the ion channel, indicating that the captured conformation of the structure *in situ* corresponds to the open state of RyR1.

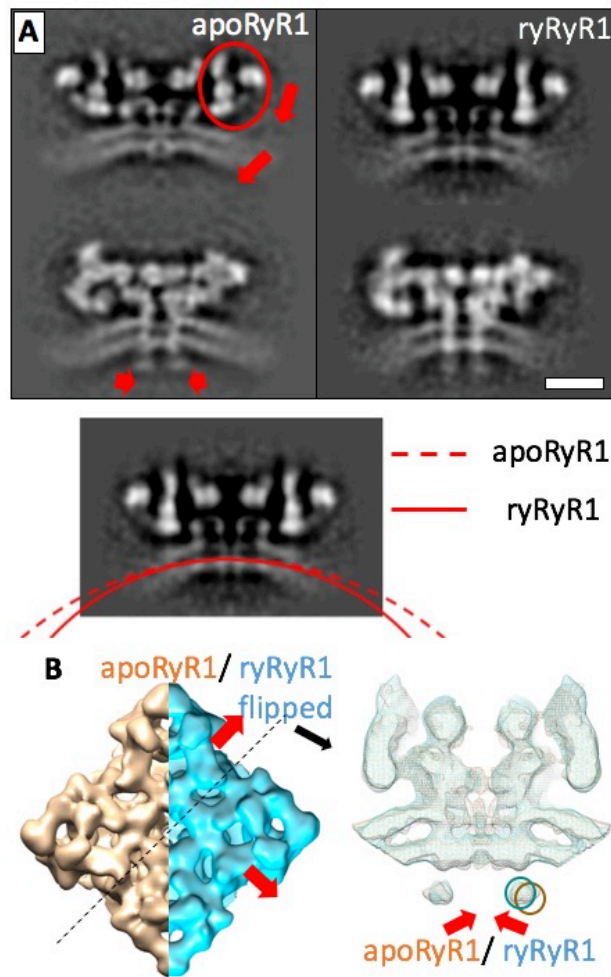


Figure 2.3.8.2. Activation of RyR1 *in situ*. A: Structure of ryRyR1 at a resolution of 17.5 Å. The movement of the outer domains is associated with a visible change in membrane curvature as compared to the apo-structure. This movement is highlighted by red arrows in the upper view of the upper-left panel. Scale bar: 10 nm. B: A volume-rendered representation of the apoRyR1 (orange) and ryRyR1 (blue) structures with the highlighted conformational changes. The left panel depicts the view down onto the receptor from the cytoplasm. The right panel depicts the section through the isosurface indicated by the dashed line, with red arrows indicating the conformational transition of the SR extensions (dark-orange and blue circles for apoRyR1 and ryRyR1, respectively).

Interestingly, other conformational changes are also observed in the SR membrane and SR lumen. There is a difference in the curvature of the SR membrane between the apoRyR1 and ryRyR1, resulting in an additional

movement of the intra-SR extensions inwards by approximately 1 nm (Figure 2.3.8.2). The membrane curvature measured in the same section through RyR1 changes from approximately $1/49 \text{ nm}^{-1}$ in the apo closed state to approximately $1/35 \text{ nm}^{-1}$ (Figure 2.3.8.3) in the presence of Ca^{2+} and ryanodine. The curvature of apoRyR1 attached to putative T-tubule membrane had a curvature of $1/54 \text{ nm}^{-1}$, slightly lower than that of apoRyR1 (Figure 2.3.8.3). In comparison, patches of the SR membrane lacking RyR1 showed a wide range of curvatures from concave to convex, with the most common appearance near flat (Figure 2.3.8.3).

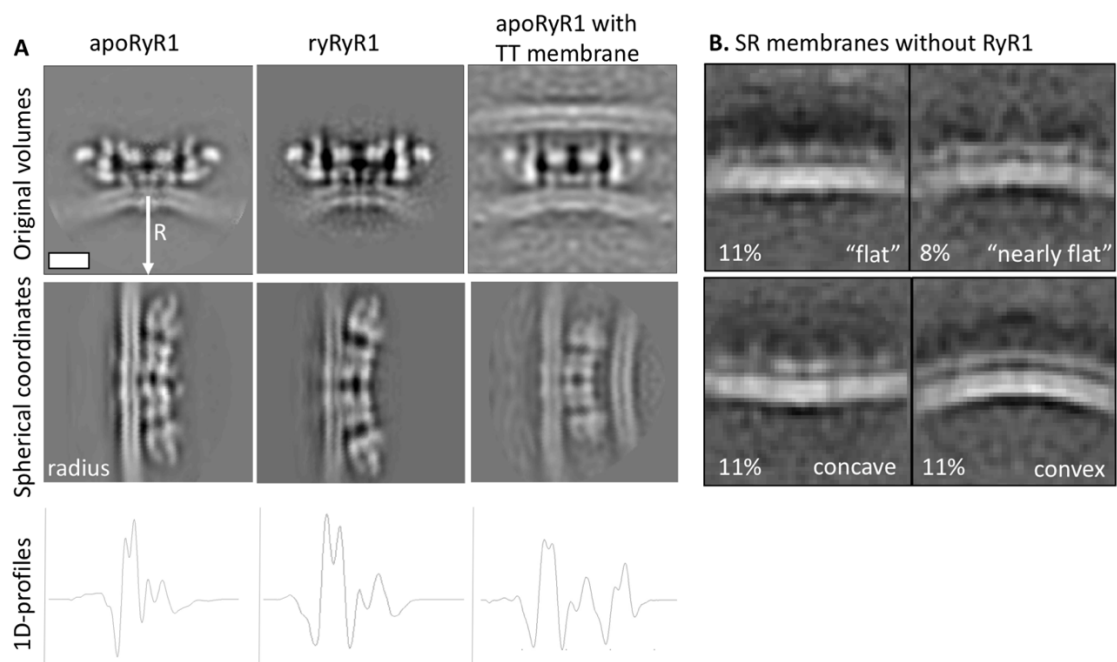


Figure 2.3.8.3. Measuring the local curvature of the membrane by transforming the density maps into spherical coordinates and varying the distance to the origin of the coordinate system. A: Top row: Maps of the apoRyR1, ryRyR1, and apoRyR1 with putative T-tubule (TT) membrane. Middle row: The maps from the top row transformed into spherical coordinates carrying the distance to the center of the spherical transformation. The radius was varied in order to optimize the flatness of the SR membrane in spherical coordinates, the values are: 49 nm for apoRyR1, 35 nm for ryRyR1 and 54 nm for apoRyR1-TT. B: Averaged patches of SR membrane lacking RyR1 in presence of EDTA. Patches show different local curvature with concave, flat or near-flat, and convex appearances. Four selected classes are shown with the

percentage of total observations indicated for each class. Scale bar for both images: 10 nm. (Figure prepared together with Dr. Misha Kudryashev)

2.4 Discussion and outlook

We prepared the SR vesicles from fresh rabbit skeletal muscles and solved the structures of RyR1 *in situ* in different functional states in native membrane by StA, following the work of Renken and colleagues (Renken et al., 2009). However, due to the use of more sophisticated hardware and more particles, we were able to achieve a significantly higher resolution of 12.6 Å in comparison to the 71 Å of the previous work. The recently reported near-atomic single particle structures allowed more detailed interpretation of our structures in native membrane. Analysis of our structure revealed the presence of four important features absent from the structures of purified receptor: an unaccommodated density in the cytoplasmic region; an additional helix-like transmembrane density proximal to the transmembrane domain of RyR1; intra-extensions in the sarcoplasmic lumen; curved membrane in the vicinity of RyR1 and curvature increasement upon activation. These differences likely result from the native environment of the receptor present in our studies while absent in the single particle studies.

The previously reported single particle structures of purified RyR1 were missing density between residues 3613 and 3639, which is observed in the *in situ* structure. Other studies have suggested that these residues are a competitive interaction site of CaM and S100A1 (Wright et al., 2008). However, at the current resolution we cannot conclude whether CaM or S100A1 is bound, or whether our structure is an average of a mixture of states. The published structure of CaM (PDB: 5TB2) in complex with a RyR1 peptide (residues 3614-3639) did not fit this observed density as a

rigid body when the RyR1 peptide termini were used to orient the structure. This rigid-body fitting resulted in both clashes and atoms that did not fit the density, suggesting that a conformational change is needed in order to accommodate CaM in its Ca²⁺-bound or Ca²⁺-free states. The fragment of RyR1 (residues 4302-4430) previously reported to interact with CaM in Ca²⁺-independent manner (Yamaguchi, Xin et al., 2001) is several nanometers away from residues 3613-3639 and is unlikely to explain the unfitted density. To better interpret this unaccommodated density, the resolution of the structure has to be improved.

Previous work has suggested that triadin, junctin and the CSQ1 polymer form a complex with RyR1 (Boncompagni, Thomas et al., 2012) and serve as a sensor for luminal Ca²⁺, inhibiting RyR1 at low Ca²⁺ concentrations (Wei, Varsanyi et al., 2006). At high Ca²⁺ concentrations, CSQ1 has been suggested to polymerize (Park, Wu et al., 2003). Some of the filaments observed inside the SR vesicles at 5 mM Ca²⁺ (Figure 2.3.6.1C) may be attributable to polymerized CSQ1 while those outside of the SR could be polymerized CSQ1 or actin. Junctin and triadin both have single predicted transmembrane helices and long disordered intra-SR domains. We were unable to identify distinct densities in the SR that could correspond to triadin or junctin; however, the ordered transmembrane density in the SR bilayer adjacent to the central pore could correspond to the transmembrane domains of triadin or junctin, or both. The *in situ* structure of RyR1 also shows ordered extensions that protrude into the SR; however, these extensions did not respond to changes in the luminal Ca²⁺ concentration. In contrast, the disperse protein density inside the SR lumen, which we speculate is CSQ1, clearly responded to changes in Ca²⁺ concentration, as would be expected for CSQ1 (Beard et al., 2009). We suggest that the sarcoplasmic extension densities may represent some part of residues

4340-4540 of RyR1, which are absent from the published atomic models due to higher flexibility in this region. Interestingly, based on fitting of the atomic model, F4540 is located in the outer bilayer of the SR membrane, and A4350 in the inner bilayer, with no other transmembrane helices predicted in the interval between them by TMHMM (Krogh, Larsson et al., 2001). We therefore can not currently estimate how many residues of RyR1 may be located in the SR lumen. Further structural analysis will be required to determine the composition of the sarcoplasmic extensions.

Understanding conformational dynamics *in situ*, including interactions with binding partners and the native membrane promises to be a comprehensive way to analyze the structure and function of proteins like RyR1 with similarly extensive regulation. However, StA structures of RyR1 *in situ* still require higher resolution in order to better understand the molecular composition and regulation of the entire RyR1 interactome in native membranes. The current class averages reported from our data do not allow interpretation at the level of secondary structure due to resolution limitations. However, there is a clear difference in class occupancy when compared to the classifications performed by both des Georges and colleagues (des Georges et al., 2016) and Efremov and colleagues (Efremov et al., 2015) on isolated RyR1. In the case of the single particle structures, the Ca^{2+} -depleted datasets had almost equal occupancies of their four classes. In contrast, the most populated class for our *in situ* data had approximately 45% of the particles, suggesting a different conformational spectrum from the purified RyR1. The most populated class *in situ* represented the global average and showed the highest similarity to class 2 from Des Georges et al. (PDB: 5TB2), suggesting that this may be a more physiologically common conformation. The observed differences in the occupancy distribution across the classes may be due to

the presence of curved native membrane, the occupancy of natively interacting proteins such as CaM/S100A1, and/or the presence of additional transmembrane proteins in the *in situ* sample.

Classification and principal component analysis of the structural variations of RyR1 revealed both expected and unexpected motions. Mode 1 from the principal component analysis demonstrates the presence of two populations of RyR1 in native membranes with and without contact between the N-terminal solenoid and the SPRY3 domain. It has been previously suggested that addition of a peptide corresponding to residues 590-628, which are located at the end the N-solenoid domain, can cause enhancement of ryanodine binding to RyR1 and RyR2 (El-Hayek, Saiki et al., 1999). In light of this, we hypothesize that mode 1 corresponds to two populations of RyR1 consisting of more or less active receptors. Receptors in the same state (with or without the contact between Nsol and SPRY3) tended to be located proximal to each other in the tomograms, suggesting that this conformational variation could be spatially regulated. The molecular mechanisms of such spatial regulation would need to be investigated further. Global conformational changes represented by the mode 1 are similar to the conformational changes between our apoRyR1 and ryRyR1 structures: the movement of the outer domains towards the SR membrane, with little displacement of the membrane itself. Mode 2 reveals variation in the distance between the leaflets of the bilayer that could result from compositional heterogeneity of bilayer itself, and which would have implications for protein function. Modes 3 and 4 show two types of vertical elongation/contraction that may relate to a change in the distance between the SR membrane and the T-tubules, something that can also occur *in vivo* as a response to membrane deformation. Similar conformational changes are present when comparing the apoRyR1 and

apoRyR1 with the putative TT-membrane structures. However, the majority of our RyR1 particles did not have the opposing T-tubule, so the presence of these modes of movements in our analysis suggests that the vertical elongation may also have additional functions. Finally, mode 5 shows an intriguing relationship between the conformation of the receptor and the local membrane curvature; however, it should be noted that the change in curvature is smaller than that observed upon activation of the receptor. It is still unknown how these observed conformational states relate to the function of RyR1, and more experiments informed by this data will be needed to further elucidate this structure-function relationship.

Interestingly, activation of the receptor increases the observed membrane curvature, a change that was not observed during a previous structural analysis of purified RyR1 reconstituted in nanodiscs (Efremov et al., 2015). Fluctuations in membrane curvature in the absence of RyR1 activation are small and have only been observed in Mode 5 of our PCA analysis (Figure 2.3.7.1D) and in 10% of the particles assigned to class 4, which had decreased membrane curvature (Figure 2.3.7.1C). This suggests that the even greater membrane curvature observed in the ryRyR1 structure is likely a consequence of RyR1 activation. The increase in membrane curvature has potential implication for the gating of RyR1. The energy stored upon RyR1 opening in the deformed membrane can contribute to additional force in the direction of channel closing. As this force contributes to the energy landscape that defines the thermodynamic properties of channel opening and closing, it should be accounted for when performing any computational modelling of the channel.

The resolution of our structures is still limited by both the number of particles and sample heterogeneity. Application of fast-incremental data collection schemes (Chreifi, Chen et al., 2019, Eisenstein, Danev et al.,

2019) may make it possible to record sufficiently large datasets in the future, which would allow better classification of the RyR1 conformational states *in situ* while still retaining a sufficient number of particles in each class to reach sub-nanometer resolution. Such structural analysis could be further complemented by the application of molecular dynamics simulations or manifold analysis (Dashti, Ben Hail et al., 2017, Frank & Ourmazd, 2016). High-resolution classification *in situ* would allow better understanding of the interactions of RyR1 with its associated proteins, as well as quantitative understanding of the conformational landscape of the open-closed transitions in native membranes.

The DHPR on the T-tubule membrane was reported to form tetrad and one DHPR tetrad is bound to every other RyR1 by freeze-fracture EM. However, we cannot see DHPR in the corresponding position in the *in situ* structure of RyR1 with adjacent T-tubule. The loss of DHPR could happen during rabbit skeletal muscle homogenization or DHPR was degraded during the purification process of SR. In the future optimized method of SR purification needs to be developed to avoid the loss or degradation of DHPR, or correlative light microscopy and cryo-EM on native rabbit skeletal muscle can be used thus the purification of SR can be avoided and the *in situ* structure of DHPR is likely to be solved (Timmermans & Otto, 2015).

Chapter 3: Improvement of the resolution of RyR1 by hybrid single particle-subtomogram averaging

3.1 Introduction of hybrid single particle-subtomogram averaging

In this chapter we aimed at obtaining higher resolution structure of RyR1 in native membranes using proposed new method so that we can further explore the structure-based mechanism of RyR1 and have a deeper understanding about it. Conventional tomography and subtomogram averaging has the advantages to solve structures of intact protein complexes *in situ*, however the resolution is often limited by multiple factors. First, proteins move in vitreous ice in non-uniform directions during data collection (Brilot, Chen et al., 2012), in the case of single particle cryo-EM the movement of proteins can be as high as 6 Å if the total electron dose reaches 35 e-/Å² (Li, Mooney et al., 2013a), which is only a quarter to a half of the electron dose applied during tomographic tilt series data collection. As a result, proteins are continuously move during data collection and the assumption that tomogram is recorded from a rigid body does not apply. Second, the electron dose on each image of the tomogram is as low as 1-3 e-/Å², which leads to only a few visible Thon rings and makes precise defocus estimation difficult. Third, the thickness of sample induces additional defocus gradient along the electron beam direction, which affects the precision of contrast transfer function (CTF) estimation and correction. The sample for tomography is usually thicker than that of single particle analysis, and the high angle tilted images result in even thicker sample. In theory CTF correction precision of 250 nm imposes a resolution limit of approximately 10 Å (Kudryashev, 2018) unless a 3D CTF correction is performed (Turonova, Schur et al., 2017). In the end, structures solved by tomography and subtomogram averaging at sub-nanometer resolution requires large number of protein particles,

large number of particles usually have to be recorded at lower magnifications which can provide larger field of view, however lower magnifications leads to lower data quality (Leigh, Navarro et al., 2019).

In the study of RyR1 *in situ* by tomography and subtomogram averaging, we aim to improve the current resolution at 12.6 Å to sub-nanometer level, which can allow us to decipher the structure with more concluded details. To do this, two strategies were adopted. First, I collected new tomographic data of SR vesicles at the higher magnification of 81000x instead of the previous 53000x. Higher magnification yielded smaller pixel size of 1.7 Å, which in theory results in more Thon rings at higher frequencies; Working together with the colleagues Ricardo Sanchez and Dr. Misha Kudryashev we processed the new dataset of ~100 tomograms and obtained an ~9.5 Å StA map. We further applied hybrid method of subtomogram averaging and single particle analysis instead of only conventional method to process the data, details were described as follows.

The hybrid method combines the advantages of single particle analysis (SPA) and subtomogram averaging (StA), which was proved to improve the resolution of structures by StA to near-nanometer level (Song, Shang et al., 2019). First, the untilted image (0° tilt) of the tomogram was recorded at higher electron dose with approximately 16 e-/Å², which has stronger and more Thon rings and higher estimated resolution limit and is single particle-like image (Figure 3.1.1). The other tilted images of the tomogram were recorded at lower electron dose with approximately 2 e-/Å², which are typical tomographic images with weaker and less Thon rings and lower estimated resolution limit (Figure 3.1.1). All those images are merged into a tilt-series. Then, the hybrid tilt-series is processed with the standard workflow, including motion correction, CTF estimation and correction, tomographic alignment and reconstruction, particle picking and

subtomogram averaging. Finally, the locations and orientations of the particles performing the reconstruction only from the untilted image are calculated and the 2D particles are extracted. Finally, local refinement of the locations and orientations of the particles against the structure with outputs from the last step by using single particle analysis is performed (Scheres, 2012) (Figure 3.1.2).

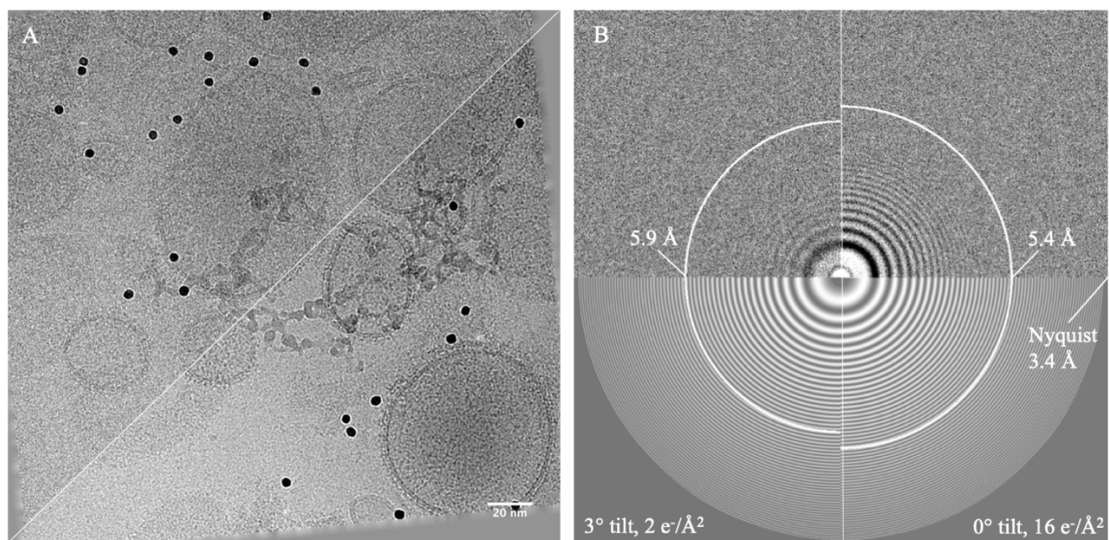


Figure 3.1.1. Comparisons of the untilted and tilted images. A: Micrograph of SR vesicles comprises half of the high-dose 0° tilt (upper left) and half of the 3° tilt (lower right); B: CTF estimation and correction of the 0° tilt and 3° tilt by Gctf. The resolution limit estimated for the 0° tilt and 3° tilt is 5.9 Å and 5.4 Å, respectively.

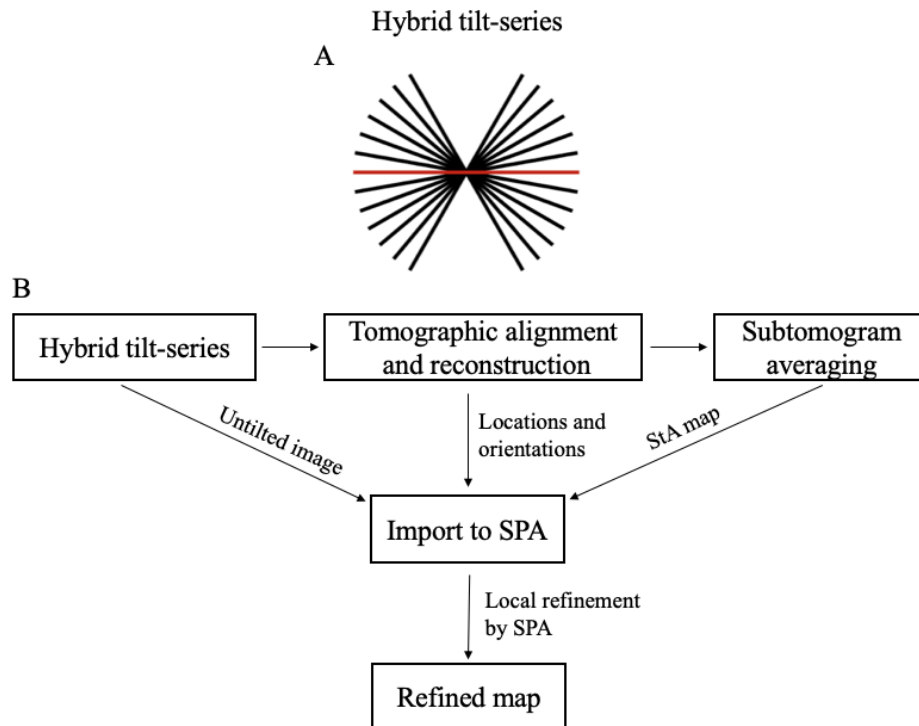


Figure 3.1.2. A: Hybrid subtomogram averaging workflow. Each line represents one image of the tilt-series, the red line represents the untilted image and other black lines represent tilted images. B: The workflow of hybrid method of SPA and StA. Hybrid tilt-series is first processed and tomogram is reconstructed, subtomogram averaging is performed and StA map is obtained. Then the untilted image and the locations and orientations of the particles from the untilted image together with StA map are imported into a module developed by our lab. Finally, local refinement by SPA is performed and refined map with improved resolution is obtained.

3.2 Methods

3.2.1 Tomographic data collection

SR vesicles were prepared with the same method described in part 1, and new tomographic datasets of SR vesicles in closed state were collected with the same method described in part 1 on the same microscope, the only difference is that the magnification used for data collection is 81000x instead of 53000x, which yielded a smaller pixel size at 1.7 Å/pixel instead of 2.7 Å/pixel.

3.2.2 Tomographic data processing

Data was first processed with the standard workflow of Cryo-ET as described in the methods of part 1, including motion correction, CTF correction, tomogram reconstruction and particle picking. 57 tomograms were reconstructed out of 97 recorded, and 2563 particles contributed to StA.

Hybrid method was used to create a dataset that can be used initially with Cryo-ET tools and then refined with Relion (Scheres, 2012). To achieve this, the electron dose of the recorded tomograms was redistributed to have one projection with a high enough electron dose so that Relion (Scheres, 2012) works. After processing the tomograms with the traditional Cryo-ET pipeline, the alignment information of each particle was exported into a created single-particle project using only the high-dose projection and then the alignment was refined. This procedure is similar with the one proposed with the software TYGRESS (Song et al., 2019), but our method has two differences: First, the high-dose projection is included in each tomogram; second, the Dynamo (Castano-Diez et al., 2012) project was imported into Relion using a custom Matlab script, instead of creating a new set of tools. It is noteworthy that as RyR1 is bound to the membrane of thick SR vesicles, the log-likelihood metric of Relion (Scheres, 2012) was replaced with the cross-correlation metric. In this way, the refinement procedure was performed in two steps. First, a traditional auto-refine project with limited angular search was performed; second, refinement with the “auto_refine” option disabled and the “always-CC” option enabled was performed. After two rounds of refinements, the structure of RyR1 was finally refined to an overall resolution at 9.5 Å.

3.3 Results

3.3.1 Structure of RyR1 in native membranes at sub-nanometer resolution

With the application of hybrid method and increase of magnification during data collection, we could be able to determine the structure of RyR1 in closed state in SR membrane by using the sample prepared with the same method described in part 1 (Figure 3.3.1.1A). From the 57 collected tomograms, we picked 2563 particles, which yielded the final structure with an imposed C4 symmetry at a global resolution of 9.5 Å (Figure 3.3.1.1B). Local resolution is higher in the central domain, which is the same as the previous structure of closed RyR1 above shows (Figure 3.3.1.1C).

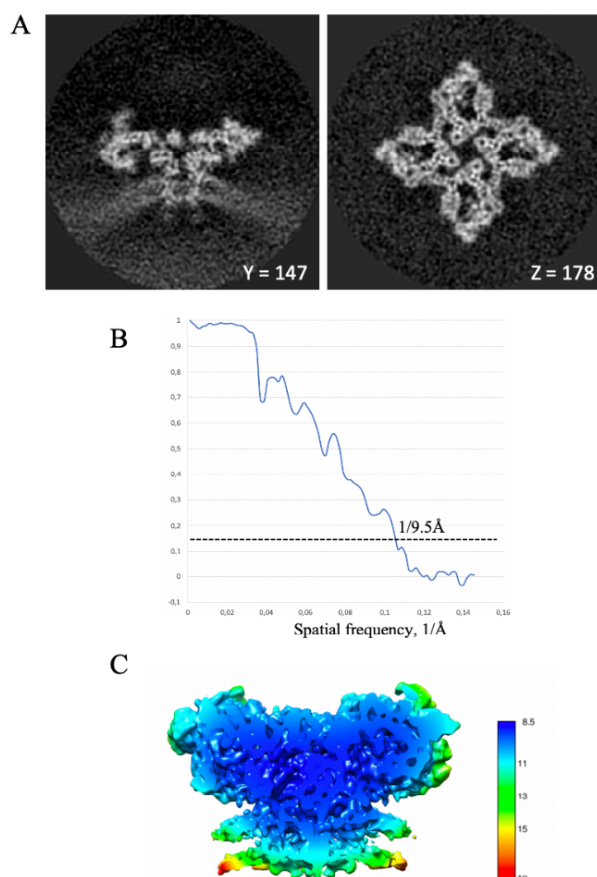


Figure 3.3.1.1. The new structure of closed RyR1 *in situ*. A: Slices through the *in situ* average map of RyR1 from the XY and XZ directions. B: Resolution measurement of

the structure by Fourier shell correlation between independently processed half-maps. C: Heat-map of the local resolution of the structure with resolutions indicated by the accompanying colorimetric key.

At the optimal contour level in Chimera (Pettersen, Goddard et al., 2004) that the density map of the overall structure is shown at best, the giant cytoplasmic region and SR membrane are present but the luminal extensions are invisible (Figure 3.3.1.2), however it is clearly visible in the previous *in situ* structure described in the part 1. The single particle structure of purified RyR1 (5TB2) can be fitted into the density well.

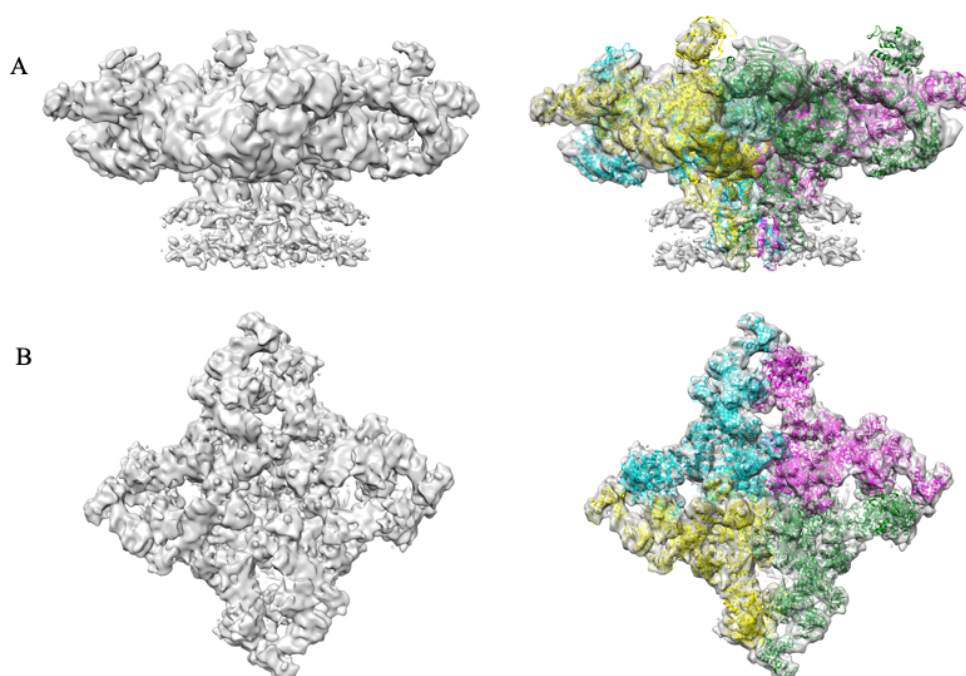


Figure 3.3.1.2. Volume-rendered visualizations of the new average structure of closed RyR1 at 9.5 Å resolution shown in side and top view, the single particle structure of RyR1 (PDB: 5TB2) was fitted into the density map, the four monomers of the structure were shown with different color.

We looked into the fitted density map and found surprisingly that the density of the unaccommodated density in the cytoplasmic domain is almost invisible in the map (Figure 3.3.1.3A), which is more defined in the

previous *in situ* structure at 12.6 Å described above (Figure 2.3.4.1). In the SR membrane, it was reported that the pore-forming helices (S5 and S6) are linked via a short amphipathic helix to the pseudo-voltage-sensor domain (pVSD) comprising S1-S4 (des Georges et al., 2016). The quality of the densities of the helices (S1-S6) of RyR1 are greatly improved (Figure 3.3.1.3B and 3.3.1.3D), all the TM helices have their corresponding densities, which in the previous *in situ* structure are not resolved completely (Figure 3.3.1.3C).

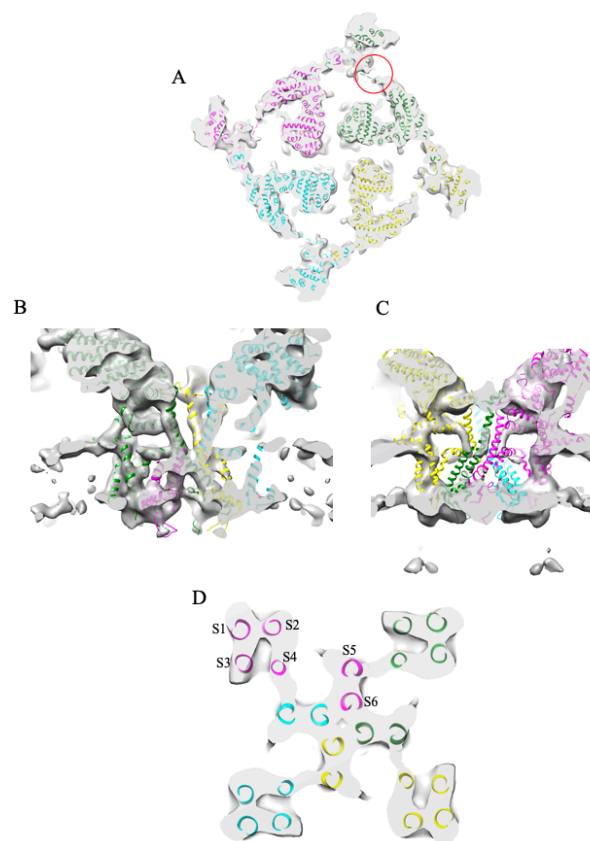


Figure 3.3.1.3. Improvements of the new RyR1 structure. A: The position of the unaccommodated density in the cytoplasmic domain in the new RyR1 density map with the fitted atomic model (PDB: 5TB2), which is shown as indicated by the red circle according to the position of the corresponding site in the previous RyR1 density map. B: The transmembrane helices of the new RyR1 density map with the fitted atomic model. C: The transmembrane helices of the previous RyR1 density map in part 1 with

the fitted atomic model. D: Cross section view of the pseudo-voltage-sensor domain (S1-S4) and the pore-forming helixes (S5 and S6).

3.4 Discussion and outlook

The improved *in situ* structure has higher resolution due to the application of hybrid method and increase of magnification for data collection. Compared to the previous *in situ* structure at lower resolution solved by conventional subtomogram averaging, the new structure presents improved features of the transmembrane (TM) helixes (S1-S6), which allows all the helixes to be fitted. The fitting is overall good, however there are some local deviations of the helixes out of the EM density, we assume that the TM helixes of our structure may present the conformation which may have minor differences with the single particle structure of the purified RyR1. To achieve better fitting, we will seek cooperation from other lab to perform molecular dynamic simulation of the single particle structure. The minor conformational difference of the TM helixes of the *in situ* structure and purified single particle structure may be due to the different environment of RyR1. RyR1 *in situ* has a more native environment than the purified RyR1 by detergents, which may have yet unknown physiological implications of the minor conformational difference.

Though the quality of the TM helixes is greatly improved, however the density of the unaccommodated density in the cytoplasmic domain and the luminal extensions are unexpectedly invisible in the new *in situ* structure. This may imply that the unaccommodated density in the cytoplasmic domain and the luminal extensions are highly flexible or dynamic, which allows the corresponding densities observable at certain extent at low resolution but becomes unfortunately poorly visible at higher resolution.

In addition, we did not perform classification of the particles, which did not distinguish the dynamic conformations and led to the poor visualization of the TM helices. The clear demonstration of these flexible regions needs more data and classification, which is our future work to do. In order to perform classification into several classes and analyze the conformational heterogeneity of RyR1 *in situ* at higher resolution, large amounts of data should be recorded and processed. In addition, I will follow the newly established protocol for the closed RyR1 to prepare open RyR1 sample in native SR membrane and also collect tomographic datasets of it with the higher magnification at 81000x, and process the datasets with the hybrid method. Compared to the results we obtained part 1, it is expected to achieve higher resolution of the open structure of RyR1 *in situ* and shed more light on the activation and open mechanisms of RyR1 *in situ*.

Chapter 4: Structure of SidE family proteins by single-particle cryo-EM

4.1 Introduction

In this chapter we combine cryo-EM and x-ray crystallography to solve the structure of SidE family proteins. The project is performed in collaboration with the lab of Prof. Dr. Ivan Dikic from Goethe Frankfurt University.

Legionella pneumophila, the causative agents of Legionnaires' disease, is a Gram-negative pathogenic bacterium that is distributed ubiquitously in fresh water environment. Infection of *L. pneumophila* of immunocompromised people can lead to severe symptoms such as bacterial pneumonia or the mild flu-like Pontiac fever (Newton, Ang et al., 2010, Qiu & Luo, 2017). During infection *L. pneumophila* first utilizes the organelle trafficking (Dot)/intracellular multiplication (Icm) type IVB secretion systems (T4BSSs) to inject more than 300 kinds of virulence proteins into its host cells such as amoebae, then it resides and replicates in a membrane-bound compartment inside host cell (Ensminger, 2016), which is called replication vacuole or known as *Legionella*-containing vacuole (LCV) (Isberg, O'Connor et al., 2009) (Figure 4.1.1). In the later phase of infection, host cell is killed and replicated bacterium are released to infect other host cells.

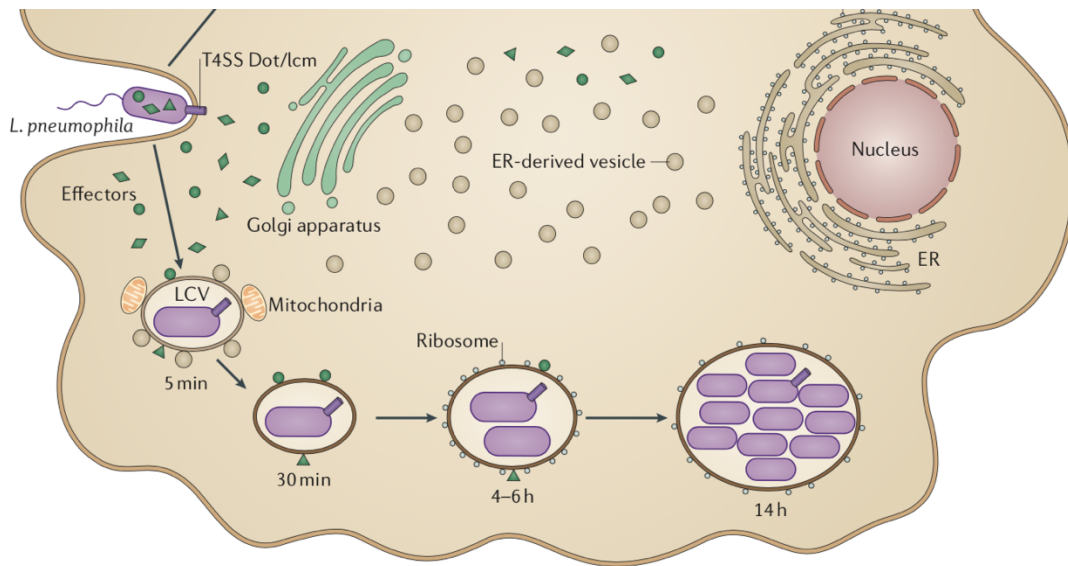


Figure 4.1.1. The infection processes of *L. pneumophila* in phagocytes (Adapted from Qiu *et, al*(Qiu & Luo, 2017)). *L. pneumophila* virulence proteins (indicated by the green geometrical shapes) translocated by the Dot/Icm T4 secretion system influence and manipulate host cellular processes. After 4-6 hours of infection, the LCV membrane surface presents ribosomes, which enable evasion of elimination of LCV by lysosome of host cell.

Currently there are over 330 kinds of virulence proteins that have been found or identified in *L. pneumophila* Dot/Icm evasion system (Ensminger, 2016).

Besides *L. pneumophila*, other *Legionella* species also have similar number of virulence proteins (Burstein, Amaro *et al.*, 2016). Among all these virulence proteins, so far only seven of them are found to be shared by all *Legionella* species (Burstein *et al.*, 2016). The biochemical activity and structural insights for most of these virulence proteins are still unclear. Previous studies showed that the virulence proteins of *L. pneumophila* modulates the vesicle trafficking pathways (Qiu & Luo, 2017). The SidE family member is one kind of the virulence proteins and contains four proteins, which are SdeA, SdeB, SdeC and SidE. They all have four common domains: deubiquitinase (DUB), phosphodiesterase (PDE),

mono-ADP-ribosyltransferase (mART), and the predicted to be coiled-coil (CC) C-terminal domain (Figure 4.1.2). Unlike canonical ubiquitylation pathway catalyzed by the three enzymes E1-E2-E3 cascade, SidE family proteins are involved into non-canonical ubiquitylation pathway (Bhogaraju, Kalayil et al., 2016).

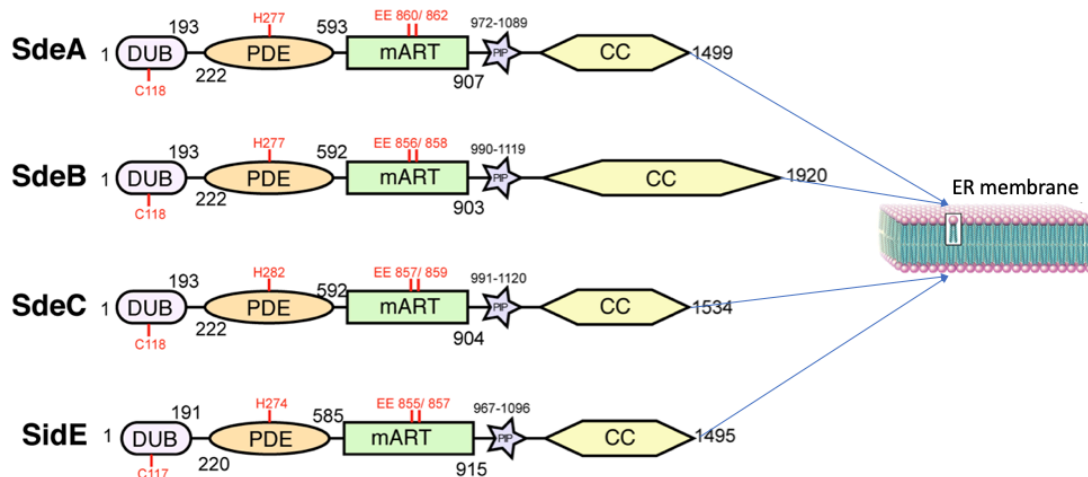


Figure 4.1.2. The SidE family members. The four members SdeA, SdeB, SdeC and SidE have four same functional domains: DUB (deubiquitinase), PDE (phosphodiesterase), mART (mono-ADP-ribosyltransferase), PIP (it is predicted to be phosphoinositide binding motif) and CC (it is predicted to be coiled coil). CC are suggested to anchor to endoplasmic reticulum (ER) membrane.

Ubiquitylation is an important post-translational modification in which the small 8.6 kDa protein ubiquitin is ligated to substrate protein (Glickman & Ciechanover, 2002, Mukhopadhyay & Riezman, 2007, Schnell & Hicke, 2003). The canonical ubiquitylation pathway is catalyzed by the well-known three enzymes E1-E2-E3 cascade through three steps. First, ubiquitin is activated in a two-step reaction by the ubiquitin-activating enzyme E1, which is ATP-dependent. E1 binds both ATP and ubiquitin and the C-terminus of ubiquitin is acyl-adenylated, then the ubiquitin is ligated to the active site cysteine residue; second, ubiquitin is transferred from E1 to the active site cysteine of the ubiquitin-conjugating enzyme E2;

third, the ubiquitin ligase E3 catalyzes the final step. An isopeptide bond is formed between one lysine of substrate protein and the C-terminal glycine of ubiquitin (Komander & Rape, 2012, Pickart & Eddins, 2004). In comparison with the above canonical ubiquitylation pathway, the SidE family proteins were found to catalyze non-canonical ubiquitylation pathway fueled by NAD without the need of E1 and E2 in recent years (Qiu, Sheedlo et al., 2016). The N-terminal DUB domain first removes ubiquitin from proteins modified via canonical ubiquitylation mechanism. Then the mono-ADP-ribosyltransferase catalyzes ADP-ribosylation at residue Arginine 42 to activate ubiquitin, finally the activated ADP-ribosylated ubiquitin (Ub-ADPR) cleaved by the phosphodiesterase domain (PDE) into AMP and phosphoribosylated ubiquitin (PR-Ub). PR-Ub is concomitantly phosphoribosylated ligated to the serine residues of substrate protein via phosphodiester bond (Qiu & Luo, 2017, Qiu et al., 2016) (Figure 4.1.3). Noteworthily, CC is proved to be anchored to the ER membrane, thus the whole protein is localized to the ER membrane, enabling to perform its catalytic activity on the main target protein Rab33, which is ER-associated (Qiu & Luo, 2017). In addition in 2018 it was reported that the phosphoribosylation of ubiquitin prevents the activation of E1 and E2 and impairs several ubiquitin-dependent processes (Bhogaraju et al., 2016), suggesting that the noncanonical ubiquitylation related enzymes can be a target for drug design to cure related diseases.

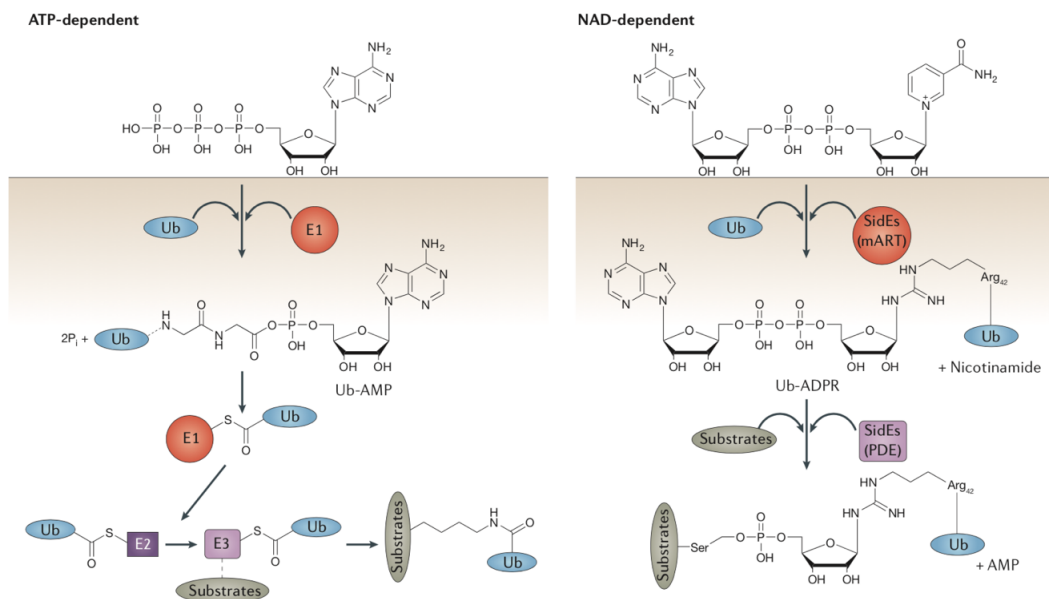


Figure 4.1.3. The mechanisms of canonical and noncanonical ubiquitylation pathways (Adapted from Qiu *et al* (Qiu & Luo, 2017)). Left: the canonical ubiquitylation pathway which uses ATP as fuel and is E1-E2 dependent; right: the noncanonical ubiquitylation pathway which uses NAD as fuel and is E1-E2 independent.

So far some structural studies of SidE family proteins have been reported. In 2018 three research groups published crystal structures of the N- and C-terminal truncated SdeA in apo state, ubiquitin-binding state and ubiquitin-NADH-binding state (Akturk, Wasilko *et al.*, 2018, Dong, Mu *et al.*, 2018, Kalayil, Bhogaraju *et al.*, 2018). In the same year structures of SidE in a similar truncated strategy were solved in apo state, ubiquitin-binding state, NAD-binding state and ADP-ribose binding state (Wang, Shi *et al.*, 2018). Those structures combined with biochemical assays elucidated the coordinated ubiquitylation process and mechanism of PDE domain and mART domain greatly, however they lack the N- and C-terminal, namely DUB domain and part of CC (Figure 4.1.4). Crystal structure of DUB domain has been reported (Sheedlo, Qiu *et al.*, 2015), the structure of CC and its underlying ER anchoring mechanism still remain enigmatic.

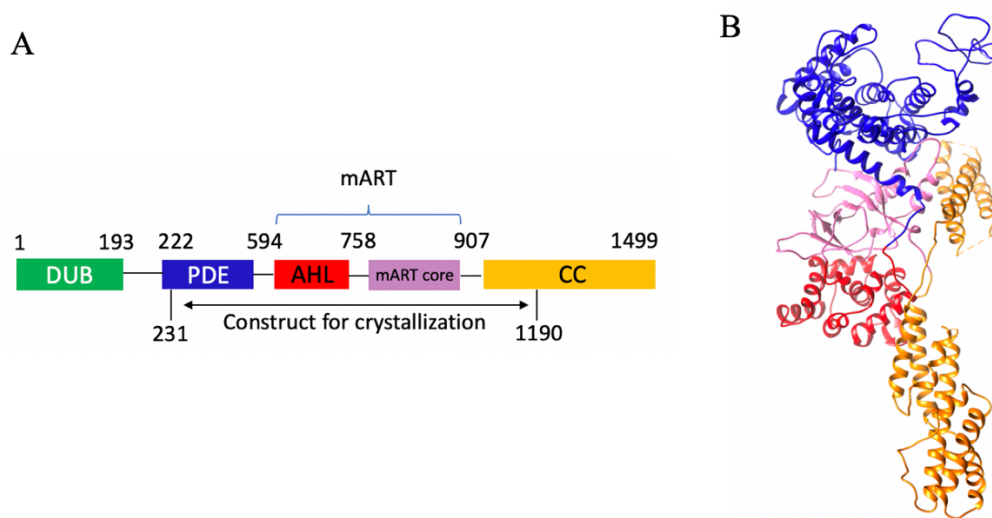


Figure 4.1.4. Crystal structure of truncated SdeA (Dong et al., 2018) (PDB: 5YIM). A: The domain diagram and the construct used for crystallization. B: crystal structure of SdeA(231-1190) which is domain-colored based on the domain diagram.

As one kind of effector proteins, SidE family members are translocated into host cell via the Dot/Icm T4BSSs (Ghosal, Jeong et al., 2019). The Dot/Icm T4BSSs is made up of about 27 components, which according to their localization can be classified into outer membrane proteins, outer membrane lipoproteins, periplasmic protein, inner membrane proteins, inner membrane-associated ATPases and soluble cytosolic proteins. These proteins exist in several subcomplexes, the coupling protein subcomplex of *Legionella* T4BSSs includes DotL, DotM, DotN, IcmS, IcmW and LvgA (Figure 4.1.5A). Among these six proteins, DotL is a hexameric ATPase hexameric ATPase that links substrate proteins to the transenvelope secretion conduit. DotL carries out functions by forming a multiprotein complex with several other proteins. Recently the crystal structure of the C-terminal of DotL (DotLc) in complex with IcmS and IcmW was reported (Kwak, Kim et al., 2017), providing insights into the selective recognition mechanisms of effector proteins (Figure 4.1.5B).

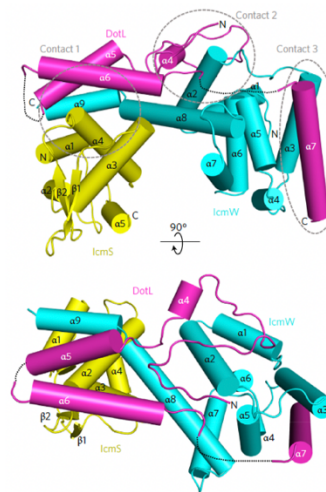
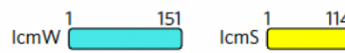
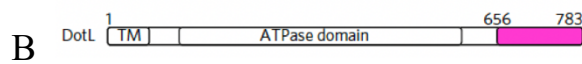


Figure 4.1.5. Components and structures of the Dot/Icm T4BSSs. A: a 3D representation of the Dot/Icm T4BSSs from subtomogram averaging (Ghosal et al., 2019), parts of the components are color-coded, OM stands for outer membrane, IM stands for inner membrane; B: the crystal structure of the DotL(656-783)-IcmW-IcmS complex (Kwak et al., 2017).

The object of the project is to solve the structure of SdeC in its full length and the complex of the C-terminal of SdeC with DotLc-IcmS-IcmW by single-particle cryo-EM. The key aspects of the structure would define the

mechanisms of the coordinated catalytic mechanisms of deubiquitylation of DUB domain and ubiquitylation of PDE and mART domains, such as how the substrate protein is transferred from DUB domain to PDE and mART domains. Furthermore, there are two questions that we want to investigate. First, the mechanism that the CC domains are anchored to the ER membrane and the interaction of the CC domains and ER membrane are still unclear, which are important for the localization of SidE family proteins. Second, what is the recognition mechanism of SidE family proteins by the DotLc-IcmS-IcmW complex? This is important for the SidE family proteins being translocated into the host cells.

4.2 Methods

4.2.1 Protein expression and purification

Biochemistry including protein expression and purification were done by our collaborator Dr. Mohit Misra from the lab of Prof. Dr. Ivan Dikic from Goethe Frankfurt University.

SdeC was cloned into vector pGEX6P1 with a N-terminal GST (Glutathione S-transferases) tag and a C-terminal His tag. The recombinant vector was amplified using NEB Turbo cells, and was expressed in the *E.coli* strain NEB Xpress cell. Cells were grown in LB medium at 37°C until the OD reaches 0.6-0.8, induced with 0.1 mM IPTG (isopropyl β -D-1-thiogalactopyranoside), grown overnight at 25°C and collected. The cell pellet was resuspended with buffer containing 50mM Tris-HCL, 0.5 M NaCl, 25 mM Imidazole, 5% glycerol, pH 7.5 and lysed by high pressure cell disruptor. Cell debris were removed by centrifugation at 14,000 g for one hour, supernatant was collected, applied to His tag affinity purification, GST tag affinity purification, ion exchange chromatography (Hiprep Q HP) and then size exclusion chromatography.

The size exclusion chromatography has two steps. First, protein pooled from ion exchange chromatography was applied to the column SD16/600 followed by SD 26/600; second, protein pooled from the column SD 26/600 was further applied to the column SD 10/300 GL 200 increase. The protein in the buffer 25 mM Tris-HCl, 100 mM NaCl, pH 7.5 eluted in a single peak and fractions were pooled and concentrated to about 0.3 mg/ml for cryo-EM grid preparation.

4.2.2 Cryo-EM grid preparation and single particle image data collection

EM sample preparation, data collection and processing are done by us. Grids were frozen in the same method as mentioned above for the RyR1 vesicle sample. 3 μ L of protein at the concentration of about 0.3 mg/ml was applied to a 300-mesh gold Quantifoil[®] R 2/2 grid with gold support. The grid was blotted with Whatman[®] No. 1 filter paper and plunged into liquid ethane cooled to liquid nitrogen temperature. Imaging was performed on a Thermo Fisher Titan Krios operated at 300 kV equipped with a Gatan K2 Summit[®] direct electron detector and a Gatan Quantum[®] energy filter.

Movies containing 40 frames were collected at x130,000 magnification in counting mode with a physical pixel size of 1.077 Å, total dose on all frames were 33 $e^-/\text{Å}^2$. Defocus values of the images ranged from -1.5 to -2.5 μ m. Data were collected by the automated imaging software EPU.

4.2.3 Image processing

Motion correction of the movies was performed by MotionCor2 (Zheng et al., 2017), defocus estimation was performed by CTFFIND (Rohou & Grigorieff, 2015). Approximately 275,909 particles from 1,314 micrographs were picked by crYOLO (Wagner, Merino et al., 2019). 2D classification and averaging and bad particles sorting were performed by

cryoSPARC (Punjani, Rubinstein et al., 2017), initial model was reconstructed by using the sorted 2D class averages. Then 3D classification based on all the particles with the initial model above was performed by cryoSPARC, one good 3D class out of six classes was obtained, 73,701 particles were contributed to this 3D class. The Mask used for excluding the flexible CC of this 3D class was generated in Chimera (Pettersen et al., 2004). Further 3D focused auto-refinement were performed by RELION (Kimanius et al., 2016), per-particle CTF refinement and beam tilt correction and per-particle motion correction called as Bayesian polishing were applied followed by the 3D auto-refinement. In the postprocessing step in RELION, a soft mask was calculated and applied to the two half-maps before the Fourier shell coefficient (FSC) was calculated resulting in an overall resolution of 4.6 Å. The B-factor estimation and map sharpening were performed in the postprocessing step. Local resolutions were estimated in RELION.

4.3 Results

4.3.1 Purification of SdeC

The purification of SdeC underwent five days at 4 °C. Size exclusion profile from the last purification step is shown in Figure 4.3.1.1A, the near-single peak corresponded to SdeC according to its molecular weight (Figure 4.3.1.1B). SDS-PAGE (sodium dodecyl sulfate–polyacrylamide gel electrophoresis) shows that there are some impurities, mass spectrometry of these impurities suggests that they are degraded SdeC (Figure 4.3.1.1C).

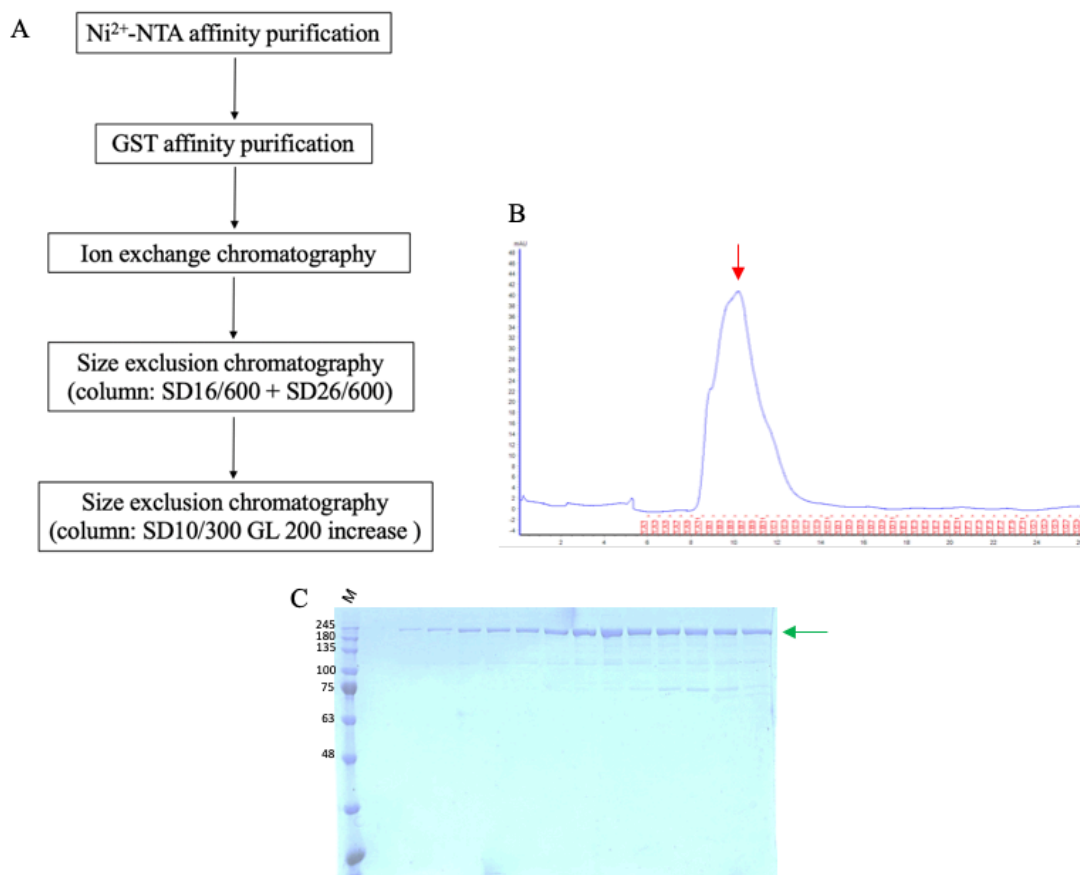


Figure 4.3.1.1. Purification of SdeC. A: The workflow of SdeC purification. B: Size exclusion chromatography profile of SdeC at the last purification step, the peak indicated by the red arrow corresponds to SdeC according to its molecular weight; C: Fractions from the peak were pooled and SDS-PAGE of the fractions were run, bands corresponding to SdeC were indicated by the green arrow. (Figure provided by Dr. Mohit Misra)

4.3.2 Cryo-EM structure of SdeC

Cryo-EM images of SdeC presents good contrast, however it is very difficult to discern isolated particles of SdeC by naked eyes (Figure 4.3.2.1B). We fully relied on crYOLO to pick the particles automatically. After performing 2D classification and averaging of the 275,909 picked particles, we picked eleven good 2D averages (Figure 4.3.2.1C) and reconstituted an initial model (Figure 4.3.2.2A). 3D classification was performed based on the initial model with all the picked particles by

crYOLO. The best 3D class was obtained out of 6 classes (Figure 4.3.2.2B), the overall density of this class looks reasonable except a small poor part in the CC domain of the C-terminal, this poor part was assumed to be caused by the flexibility of it and it was masked out and local refinement was performed on the rest of the density to achieve higher resolution (Figure 4.3.2.2C). Local refinement and CTF refinement and beam tilt correction and Bayesian polishing were done in RELION, finally yielding a structure with an overall resolution at 4.6 Å (Figure 4.3.2.2D and 4.3.2.3). The crystal structure of SdeA₂₃₁₋₁₁₉₀ can be well fitted into the density map, however the N-terminal DUB domain and GST tag are missing, and part of CC domain on the C-terminal is also missing because the EM density of this part is originally poor, so it was masked out for the local refinement of the remaining structure (Figure 4.3.2.2D). The missing part of CC domain has several hydrophobic residues, which may potentially contribute to the suggested interaction of CC domain and the ER membrane. The missing part of CC domain is also likely to be unfolded in the purified form as it has hydrophobic residues, which may be the reason why its density is poor in the EM map of SdeC.

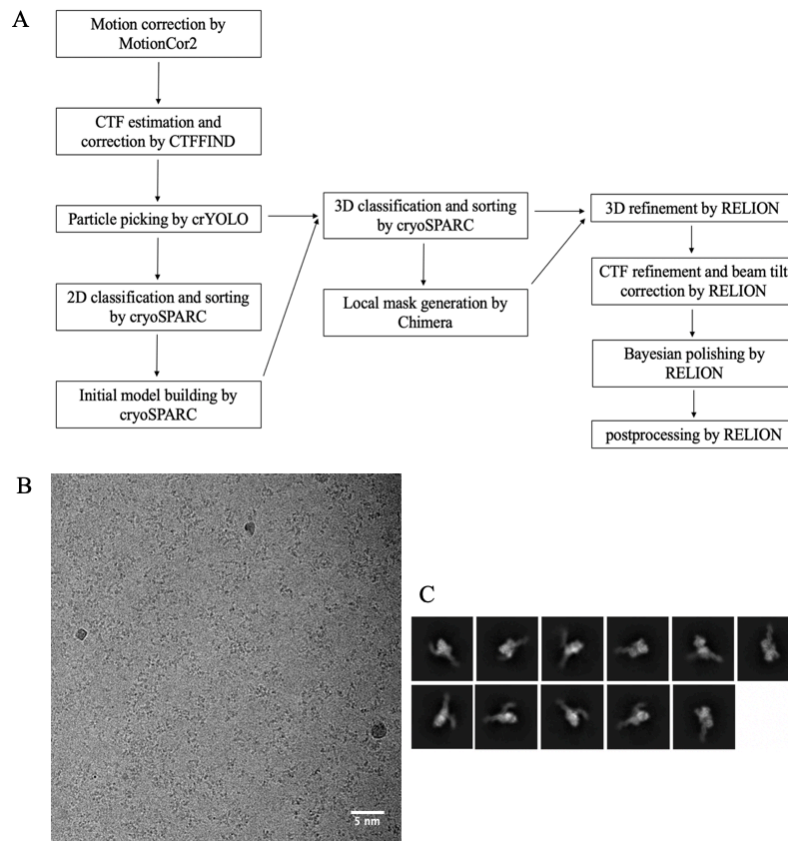


Figure 4.3.2.1 A: The workflow of EM image data processing. B: A typical motion-corrected cryo-EM micrograph of SdeC. C: The eleven good 2D class averages which were picked out of 150 Classes.

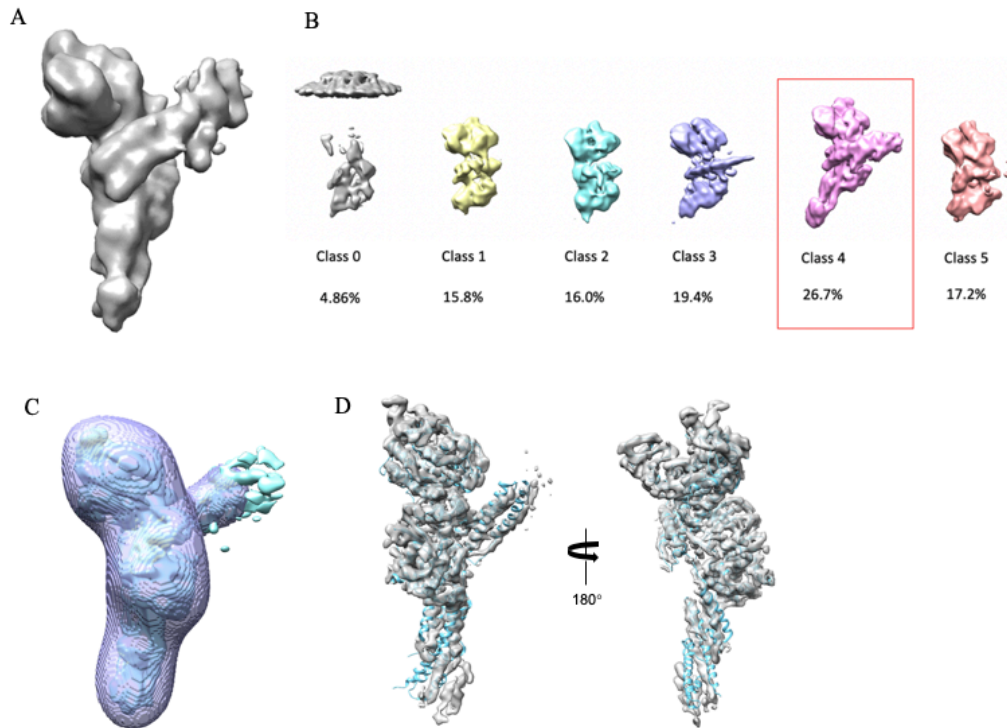


Figure 4.3.2.2. 3D classification and local refinement of the SdeC density map. A: the initial model generated by cryoSPARC with 275,909 particles. B: the six 3D classes and their corresponding ratio of particles, the good 3D class was highlighted with the red rectangular. C: The applied mask shown in purple color which masked out the flexible part of the C-terminal, density inside the mask was kept and used as initial model for the local refinement. D: After local refinement and CTF refinement and beam tilt correction and Bayesian polishing in RELION, the crystal structure of SdeA was docked into the final refined model.

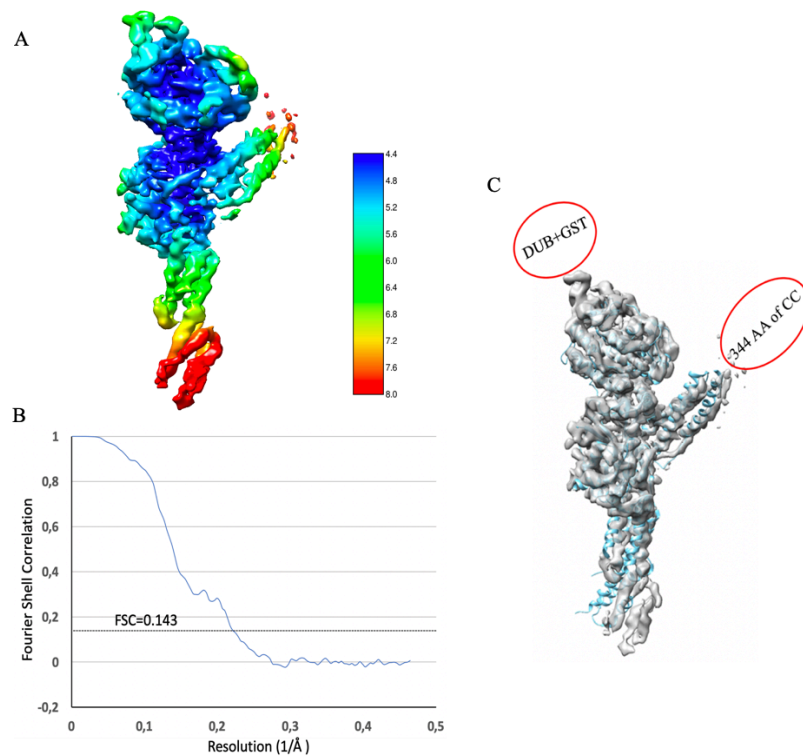


Figure 4.3.2.3. Resolution of SdeC by single-particle cryo-EM. A: The local resolution of the density map generated in RELION. B: The Fourier Shell Correlation (FSC) plot generated with output from RELION, final resolution is 4.6 Å derived from FSC between two independently processed half-sets of data (FSC=0.143). C: the missing densities of the full-length SdeC which are indicated by red ellipsoids. One missing density is the DUB domain plus a GST tag in the N-terminal, another missing density is about 344 amino acids (AA) in the CC domain.

4.3.3 CC domain and the composite map SdeA-CC₂₃₁₋₁₄₉₉

We employed a hybrid structural approach for structural determination of the proteins from Side family. Dr. Mohit Misra attempted to solve structure of the CC domain from SdeA,B,C and have successfully solved the structure of SdeA-CC₁₁₅₈₋₁₄₉₉. Native crystals were able to be diffracted to 2 Å, combining with the diffraction data of native crystals soaked with 1mM EMTS, the crystal structure of SdeA-CC₁₁₅₈₋₁₄₉₉ was solved. To our knowledge, this structure is the first structure of CC domain among all the

members of SidE family proteins. The structure comprises of 10 α -helices, the overall structure of SdeA-CC₁₁₅₈₋₁₄₉₉ has a bow shape (Figure 4.3.3.1).

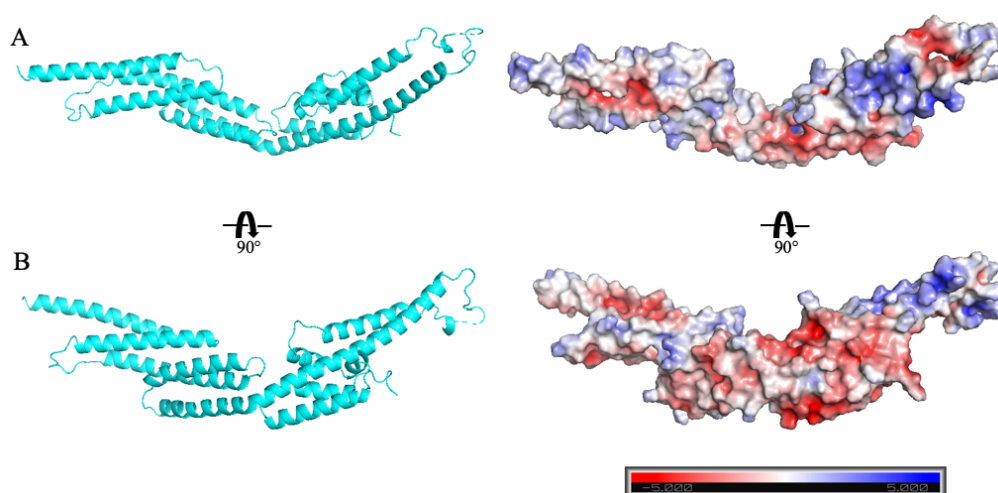


Figure 4.3.3.1 Crystal structure of SdeA-CC₁₁₅₈₋₁₄₉₉, which contains 10 helices. A and B: Two different views of the structure and their corresponding electrostatic potential maps. (Figure courtesy of Dr. Mohit Misra)

The crystal structure of SdeA-CC₁₁₅₈₋₁₄₉₉ and the reported structure of SdeA₂₃₁₋₁₁₉₀ could be superimposed on one common α -helix that is harboured in both structures, since the common α -helix is the last α -helix of the previously known structure of SdeA (PDB:5YIM) and also the first α -helix in the structure of SdeA-CC₁₁₅₈₋₁₄₉₉ (Figure 4.3.3.2A). The combined structure contains the PDE domain, mART domain and CC domain while lacking the DUB domain. The combined structure of SdeA₂₃₁₋₁₄₉₉ can also be fitted into the EM density map of SdeC (Figure 4.3.3.2B). The structure of SdeA-CC₁₁₅₈₋₁₄₉₉ does not have the corresponding EM density.

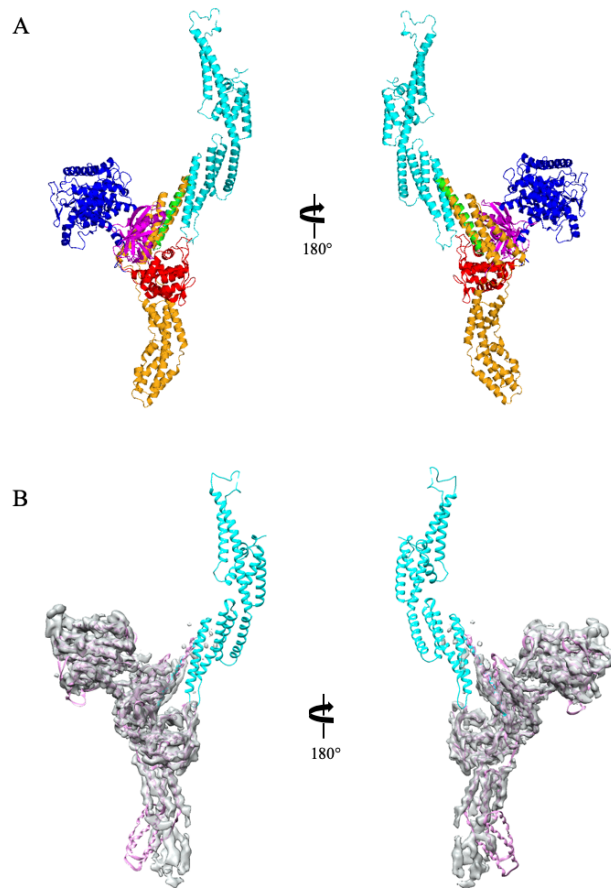


Figure 4.3.3.2. A: The combined structure of SdeA₂₃₁₋₁₄₉₉, SdeA-CC₁₁₅₈₋₁₄₉₉ is cyan, the other domains of SdeA are the same color coded as shown in figure 4. B: The combined structure of SdeA₂₃₁₋₁₄₉₉ fitted into the EM density map of SdeC shown in figure 8, the SdeA-CC₁₁₅₈₋₁₄₉₉ part has no corresponding EM density. (Figure courtesy of Dr. Mohit Misra)

4.4 Discussion and outlook

We used a “divide and conquer” approach to determine the structure of the SidE family proteins by a combination of single particle cryo-EM and X-ray crystallography. We determined the structure of SdeC at 4.6 Å resolution by single particle cryo-EM. In the EM density map of SdeC, the DUB domain and GST tag on the N-terminal and part of the CC (from amino acid 1190 to 1534, hereafter referred as CC₁₁₉₀₋₁₅₃₄) on the C-terminal are invisible, which are similar with the truncated crystal

structure (Figure 4.3.2.2), suggesting that the linker between DUB domain and the following PDE domain, and the linker between the CC₁₁₉₀₋₁₅₃₄ and the present CC part in the structure are flexible, thus the crystal structure of the full length SdeC is unavailable as it is likely difficult to crystallize the full length protein due to the flexibilities. Secondary structure predictions also show that these linkers are disordered, further proving their flexibilities. In order to obtain the structure of the CC₁₁₉₀₋₁₅₃₄, we are trying to grow crystals of CC₁₁₉₀₋₁₅₃₄ and solve its structure by x-ray crystallography since it is small. In addition, we are also trying to purify the complex of CC₁₁₉₀₋₁₅₃₄+IcmS+IcmW+DotLc and solve the structure of it by either x-ray crystallography and single particle cryo-EM. The resolution of the current structure of SdeC is likely limited by the small number of particles. Next we also aim to collect more data to improve the resolution.

In addition, other two research groups Kalayil and colleagues (Kalayil et al., 2018) and Akturk and colleagues (Akturk et al., 2018) have also reported the crystal structures of similar truncated SdeA at the same time. These two crystal structures are shorter and only contain PDE domain and mART domain without CC at all (hereafter referred as shorter-SdeA), which present conformational differences compared to the structure of the longer construct that contains part of CC (hereafter referred as longer-SdeA). Superposition of these three structures show that the α -helical lobe (AHL, amino acids 592-758) from the mART domain of the shorter-SdeA undergone a large swing. The AHL in the two shorter-SdeA adopt an extended conformation, while the AHL in the longer-SdeA adopts a closed conformation (Figure 4.4.1). The extended conformation of AHL of the shorter-SdeA was also detected by the small-angle x-ray scattering (SAXS), suggesting that this extended conformation is the natural state of

of the shorter-SdeA, instead of being caused by crystal packing force. The reason why the AHLs adopt different conformations in the shorter-SdeA and longer-SdeA is probably the CC in the longer-SdeA prevents the AHL swinging to the extended conformation and “locks” it to the closed conformation. Our EM structure of SdeC which contains part of CC shows similar conformation with that of the longer-SdeA, further proving that CC is important to keep the closed conformation of AHL. Mutation assays proved that AHL plays an important role in the ADP-ribosylation activity of mART domain. The closed conformation of AHL mediates contact with NAD^+ in the structure of clostridium perfringens iota-toxin (Tsurumura, Tsumori et al., 2013), which functions in the regulation of cytoskeletal disorganization and cell death and it also possesses mART domain. This observation suggests that the closed conformation of AHL is required for the mART activity of SdeA.

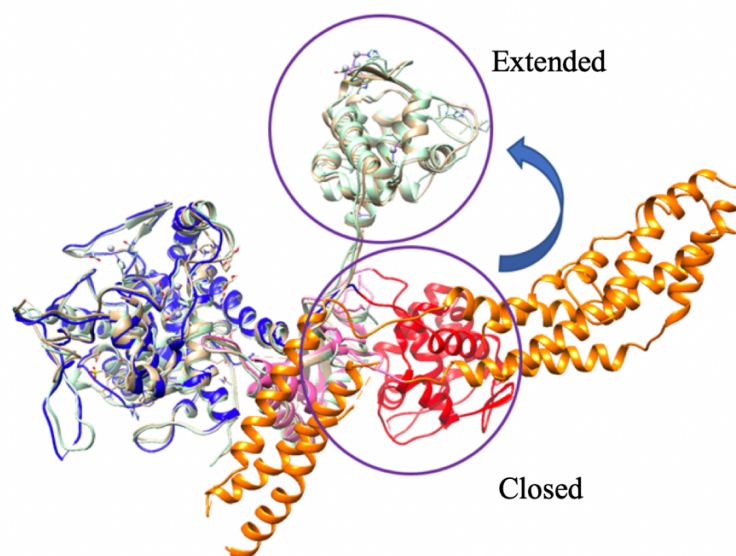


Figure 4.4.1. Overlay of the longer-SdeA and the two shorter-SdeA. The longer-SdeA is domain-colored as that of Figure 4.1.4. The two shorter-SdeA are colored gold and light green. The AHLs are highlighted as the purple circles, the huge swing of AHL from closed conformation in the longer-SdeA to extended conformation in the shorter-SdeA.

In all of the current structures of the SidE family proteins, none of them contain the structure of DUB domain, which is probably due to the flexibility of the linker between DUB domain and PDE domain. The DUB domain catalyzes deubiquitination of substrate proteins ubiquitinated through the canonical ubiquitylation pathway by a proposed hydrolytic mechanism. The deubiquitinated substrate proteins can be further ubiquitinated through the noncanonical ubiquitylation pathway by the SidE family proteins, those ubiquitinated substrate proteins do not perform their normal physiological functions any more. Though the crystal structure of DUB domain was already reported and the deubiquitination mechanism was unveiled, the full length structures of SidE family proteins which have DUB domain and other domains together are currently still unavailable, the question how DUB domain and other domains coordinate to perform deubiquitination and ubiquitination by different mechanisms on the same substrate protein still does not have a definite answer. It could be highly interesting try to solve the flexibility problem of the linker between DUB domain and PDE domain and obtain the structure of the combined domains, the methods we can try include Grafix (Stark, 2010) and GraDeR (Hauer, Gerle et al., 2015), which can potentially stabilize proteins by addition of a crosslinker.

Our composite structure which includes the crystal structure of SdeA₁₁₅₈₋₁₄₉₉ is the first solved structure of CC domain among the members of SidE family proteins. The electrostatic map shows that it possesses a positively charged site (Figure 4.4.2B), while the secretion chaperone (DotL(656-783)-IcmW-IcmS complex) of the Type IV secretion system components of *Legionella* possesses a negatively charged groove (Figure 4.4.2A) (Kwak et al., 2017). It was reported that the DotL(656-783)-IcmW-IcmS

complex can interact with the *Legionella* effector proteins to inject them into the host cells. Based on this information, we could assume the interaction between them (Figure 4.4.2C).

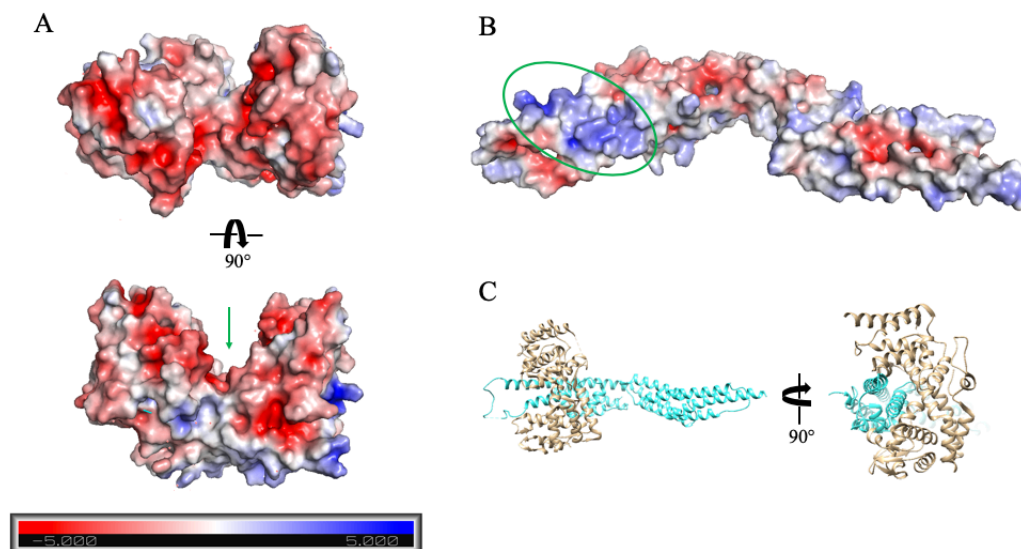


Figure 4.4.2. Assumed interaction between DotL(656-783)-IcmW-IcmS complex and SdeA-CC₁₁₅₈₋₁₄₉₉. A: Two different views of the electrostatic potential maps of the crystal structure of the DotL(656-783)-IcmW-IcmS complex, the green line indicates the groove which has acidic amino acids with negative charges. B: The electrostatic potential map of the crystal structure of SdeA-CC₁₁₅₈₋₁₄₉₉, the green ellipsoid indicates the site which has alkaline amino acids with positive charges. C: The assumptive interaction of the DotL(656-783)-IcmW-IcmS complex and SdeA-CC₁₁₅₈₋₁₄₉₉ based on their opposite charges shown in figure A and B. The Gold-colored structure is DotL(656-783)-IcmW-IcmS complex and the cyan-colored structure is SdeA-CC₁₁₅₈₋₁₄₉₉. (Figure courtesy of Dr. Mohit Misra)

By combing the crystal structure of SdeA-CC₁₁₅₈₋₁₄₉₉ and the reported structure of SdeA₂₃₁₋₁₁₉₀, we were able to build the atomic model of SdeA₂₃₁₋₁₄₉₉, which for the first time provides a panoramic view of the Side family proteins containing the PDE domain, mART domain and CC domain. The long CC domain extends like a α -helical arm and is supposed

to bind to the phospholipids present in the membrane based on the biochemical data of Dr. Mohit Misra. The CC domain acts as a recognition motif for the Type IV secretion system components when present inside the bacteria and serves as a membrane binding platform in order to modify the substrates by phospho-ribose ubiquitination when injected into the host cells, thus it is important to understand its structure and function. The interaction of the CC domain and the phospholipids is highly interesting and it is potentially possible to understand the interaction by solving the structure of protein with the CC domain reconstituted into nanodiscs using single particle cryo-EM (Bayburt & Sligar, 2010, Yokogawa, Fukuda et al., 2019). Such structural analysis may provide insights into which amino acids of the CC domain are responsible for the interaction.

Chapter 5: Concluding remarks and future perspectives

Membrane proteins are involved into various important life processes and it is key to solve their structures to understand the structure-based mechanisms. Due to the fast development of cryo-EM technique in recent years, now cryo-EM has become a very powerful and suitable technique to be applied to the structural studies of membrane proteins, especially for the non-crystalline membrane proteins and the large and dynamic membrane protein complexes (De Zorzi et al., 2016). Single-particle cryo-EM can solve the structures of purified proteins to atomic resolutions (Kuhlbrandt, 2014), while cryo-electron tomography and subtomogram averaging enable the structural studies of membrane proteins and protein complexes in their native context (Zhang, 2019). In my thesis, we solved the structures of RyR1 in native SR membrane at apo and ryanodine-binding states at 12.6 Å and 17.5 Å, respectively. The observed extra densities in the cytoplasmic domain and SR membrane and SR lumen which are not present in the high-resolution structures of purified RyR1 by single-particle cryo-EM provide a case showing that the structures of membrane proteins can have differences between their native states and isolated states, hence it is important and meaningful to investigate the structures of membrane proteins in their native context, in which the structures can be preserved completely. In addition, the work of RyR1 in my thesis also suggests that it is very practical and informative to combine cryo-electron tomography and subtomogram averaging with single-particle cryo-EM to solve and interpretate the structures of membrane together. Cryo-electron tomography and subtomogram averaging can provide a more complete density map of membrane protein at intermediate resolution, in which the high-resolution single particle or crystal structures of different components of membrane protein can be fitted in. The

combined results enable the panoramic description and comprehensive interpretation the structures of membrane proteins in their native environments. Moreover, the resolution of the structure of RyR1 in native membrane at apo states was successfully improved to 9.5 Å using hybrid method which combines cryo-electron tomography and subtomogram averaging with single particle analysis. It shows that those two cryo-EM techniques can be well combined to achieve higher resolution of structures of membrane proteins in native environments, which is another advantage of the cryo-EM techniques combination.

The resolution achieved by cryo-EM is limited by many factors. Among them sufficient number of particles is a critical factor to achieve higher resolution. Unlike single-particle cryo-EM, the data collection speed of cryo-electron tomography is usually much more time-consuming (~40-50 minutes per target) and is difficult to collect large number of particles. In 2019 the reported fast-incremental single-exposure (FISE) tilt series scheme to collect tomography in less than 5 minutes per target provides a promising alternative method to collect sufficient number of particles (Eisenstein et al., 2019). Beside resolution improvement, with more particles conformational heterogeneity of membrane proteins in native context can be more reliably analyzed and deeper structural insights into mechanisms of membrane proteins can be obtained. We aim to collect more data using this new strategy in the future in order to further improve the resolution and better understand the mechanisms of RyR1 in native membrane.

In my thesis another work about the SidE family proteins is a successful case in which single-particle cryo-EM and x-ray crystallography are well combined. Using single-particle cryo-EM, the structure of the rigid domains of SdeC was solved to 4.6 Å, in which crystal structure of the

homologous protein SdeA can be fitted. Using x-ray crystallography, the structure of the CC domain of SdeA was solved to 2 Å. Based on one common helix harbored by these two structures, the overlay structure including CC domain was obtained, which provides the near-panoramic view of the SidE family proteins for the first time. On another side, the peripheral CC domain is one of our focus of interests as it is important for the recognition and importation by the TypeIV secretion system into host cell and for the localization of the SidE family proteins on the ER membrane. In our results part of the CC domain which is suggested to bind to the ER membrane does not have clear density in the EM map, one of the possible reasons is that the membrane-interacting CC domain is partially unfolded in the purified form without detergents. Based on this, it may indicate that some peripheral membrane proteins are somehow similar with the integral membrane proteins.

References

- Akturk A, Wasilko DJ, Wu XC, Liu Y, Zhang Y, Qiu JZ, Luo ZQ, Reiter KH, Brzovic PS, Klevit RE, Mao YX (2018) Mechanism of phosphoribosyl-ubiquitination mediated by a single Legionella effector. *Nature* 557: 729-+
- Al-Qusairi L, Laporte J (2011) T-tubule biogenesis and triad formation in skeletal muscle and implication in human diseases. *Skelet Muscle* 1: 26
- Bai XC, McMullan G, Scheres SHW (2015) How cryo-EM is revolutionizing structural biology. *Trends Biochem Sci* 40: 49-57
- Bai XC, Yan C, Yang G, Lu P, Ma D, Sun L, Zhou R, Scheres SHW, Shi Y (2015) An atomic structure of human gamma-secretase. *Nature* 525: 212-217
- Bai XC, Yan Z, Wu J, Li Z, Yan N (2016a) The Central domain of RyR1 is the transducer for long-range allosteric gating of channel opening. *Cell Res* 26: 995-1006
- Bai XC, Yan Z, Wu JP, Li ZQ, Yan N (2016b) The Central domain of RyR1 is the transducer for long-range allosteric gating of channel opening. *Cell Research* 26: 995-1006
- Barone V, Randazzo D, Del Re V, Sorrentino V, Rossi D (2015) Organization of junctional sarcoplasmic reticulum proteins in skeletal muscle fibers. *J Muscle Res Cell M* 36: 501-515
- Bayburt TH, Sligar SG (2010) Membrane protein assembly into Nanodiscs. *FEBS Lett* 584: 1721-7
- Beard NA, Wei L, Dulhunty AF (2009) Ca(2+) signaling in striated muscle: the elusive roles of triadin, junctin, and calsequestrin. *Eur Biophys J* 39: 27-36

Bhogaraju S, Kalayil S, Liu YB, Bonn F, Colby T, Matic I, Dikic I (2016) Phosphoribosylation of Ubiquitin Promotes Serine Ubiquitination and Impairs Conventional Ubiquitination. *Cell* 167: 1636-+

Boncompagni S, Thomas M, Lopez JR, Allen PD, Yuan Q, Kranias EG, Franzini-Armstrong C, Perez CF (2012) Triadin/Junctin double null mouse reveals a differential role for Triadin and Junctin in anchoring CASQ to the jSR and regulating Ca(2+) homeostasis. *PLoS One* 7: e39962

Brilot AF, Chen JZ, Cheng A, Pan J, Harrison SC, Potter CS, Carragher B, Henderson R, Grigorieff N (2012) Beam-induced motion of vitrified specimen on holey carbon film. *J Struct Biol* 177: 630-7

Burstein D, Amaro F, Zusman T, Lifshitz Z, Cohen O, Gilbert JA, Pupko T, Shuman HA, Segal G (2016) Genomic analysis of 38 Legionella species identifies large and diverse effector repertoires. *Nat Genet* 48: 167-75

Cao E, Liao M, Cheng Y, Julius D (2013) TRPV1 structures in distinct conformations reveal activation mechanisms. *Nature* 504: 113-8

Castano-Diez D, Kudryashev M, Arheit M, Stahlberg H (2012) Dynamo: A flexible, user-friendly development tool for subtomogram averaging of cryo-EM data in high-performance computing environments. *Journal of Structural Biology* 178: 139-151

Castano-Diez D, Kudryashev M, Stahlberg H (2017) Dynamo Catalogue: Geometrical tools and data management for particle picking in subtomogram averaging of cryo-electron tomograms. *J Struct Biol* 197: 135-144

Castano-Diez D, Zanetti G (2019) In situ structure determination by subtomogram averaging. *Curr Opin Struct Biol* 58: 68-75

Cheng YF (2018) Single-particle cryo-EM-How did it get here and where will it go. *Science* 361: 876-+

Chreifi G, Chen SY, Metskas LA, Kaplan M, Jensen GJ (2019) Rapid tilt-series acquisition for electron cryotomography. *Journal of Structural Biology* 205: 163-169

Contreras FX, Ernst AM, Wieland F, Brugger B (2011) Specificity of intramembrane protein-lipid interactions. *Cold Spring Harb Perspect Biol* 3

Dashti A, Ben Hail D, Mashayekhi G, Schwander P, des Georges A, Frank J, Ourmazd A (2017) Conformational Dynamics and Energy Landscapes of Ligand Binding in RyR1 *bioRxiv*

Dashti A, Schwander P, Langlois R, Fung R, Li W, Hosseinizadeh A, Liao HY, Pallesen J, Sharma G, Stupina VA, Simon AE, Dinman JD, Frank J, Ourmazd A (2014) Trajectories of the ribosome as a Brownian nanomachine. *P Natl Acad Sci USA* 111: 17492-17497

De Zorzi R, Mi W, Liao MF, Walz T (2016) Single-particle electron microscopy in the study of membrane protein structure. *Microscopy-Jpn* 65: 81-96

des Georges A, Clarke OB, Zalk R, Yuan Q, Condon KJ, Grassucci RA, Hendrickson WA, Marks AR, Frank J (2016) Structural Basis for Gating and Activation of RyR1. *Cell* 167: 145-157 e17

Dong YA, Mu YJ, Xie YC, Zhang YP, Han YY, Zhou Y, Wang WH, Liu ZH, Wu M, Wang H, Pan M, Xu N, Xu CQ, Yang MJ, Fan SL, Deng HT, Tan TW, Liu XY, Liu L, Li J et al. (2018) Structural basis of ubiquitin modification by the Legionella effector SdeA. *Nature* 557: 674-+

Efremov RG, Leitner A, Aebersold R, Raunser S (2015) Architecture and conformational switch mechanism of the ryanodine receptor. *Nature* 517: 39-43

Eisenstein F, Danev R, Pilhofer M (2019) Improved applicability and robustness of fast cryo-electron tomography data acquisition. *J Struct Biol*

El-Hayek R, Saiki Y, Yamamoto T, Ikemoto N (1999) A postulated role of the near amino-terminal domain of the ryanodine receptor in the regulation of the sarcoplasmic reticulum Ca(2+) channel. *J Biol Chem* 274: 33341-7

Ensminger AW (2016) Legionella pneumophila, armed to the hilt: justifying the largest arsenal of effectors in the bacterial world. *Curr Opin Microbiol* 29: 74-80

Fan X, Wang J, Zhang X, Yang Z, Zhang JC, Zhao LY, Peng HL, Lei JL, Wang HW (2019) Single particle cryo-EM reconstruction of 52 kDa streptavidin at 3.2 Angstrom resolution. *Nat Commun* 10

Fang QL, Zhu DJ, Agarkova I, Adhikari J, Klose T, Liu Y, Chen ZG, Sun YY, Gross ML, Van Etten JL, Zhang XZ, Rossmann MG (2019) Near-atomic structure of a giant virus. *Nat Commun* 10

Fernandez-Leiro R, Scheres SHW (2016) Unravelling biological macromolecules with cryo-electron microscopy. *Nature* 537: 339-346

Frangakis AS, Hegerl R (2001) Noise reduction in electron tomographic reconstructions using nonlinear anisotropic diffusion. *Journal of Structural Biology* 135: 239-250

Frank J, Ourmazd A (2016) Continuous changes in structure mapped by manifold embedding of single-particle data in cryo-EM. *Methods* 100: 61-67

Franzini C (1970) Studies of Triad .1. Structure of Junction in Frog Twitch Fibers. *Journal of Cell Biology* 47: 488-+

Galaz-Montoya JG, Ludtke SJ (2017) The advent of structural biology in situ by single particle cryo-electron tomography. *Biophys Rep* 3: 17-35

Ghosal D, Jeong KC, Chang YW, Gyore J, Teng L, Gardner A, Vogel JP, Jensen GJ (2019) Molecular architecture, polar targeting and biogenesis of the Legionella Dot/Icm T4SS. *Nat Microbiol* 4: 1173-1182

- Glickman MH, Ciechanover A (2002) The ubiquitin-proteasome proteolytic pathway: destruction for the sake of construction. *Physiol Rev* 82: 373-428
- Hagen WJH, Wan W, Briggs JAG (2017) Implementation of a cryo-electron tomography tilt-scheme optimized for high resolution subtomogram averaging. *Journal of Structural Biology* 197: 191-198
- Hakamata Y, Nakai J, Takeshima H, Imoto K (1992) Primary structure and distribution of a novel ryanodine receptor/calcium release channel from rabbit brain. *FEBS Lett* 312: 229-35
- Haselbach D, Schrader J, Lambrecht F, Henneberg F, Chari A, Stark H (2017) Long-range allosteric regulation of the human 26S proteasome by 20S proteasome-targeting cancer drugs. *Nat Commun* 8
- Hauer F, Gerle C, Fischer N, Oshima A, Shinzawa-Itoh K, Shimada S, Yokoyama K, Fujiyoshi Y, Stark H (2015) GraDeR: Membrane Protein Complex Preparation for Single-Particle Cryo-EM. *Structure* 23: 1769-1775
- Hwang JH, Zorzato F, Clarke NF, Treves S (2012) Mapping domains and mutations on the skeletal muscle ryanodine receptor channel. *Trends in Molecular Medicine* 18: 644-657
- Inui M, Saito A, Fleischer S (1987) Purification of the Ryanodine Receptor and Identity with Feet Structures of Junctional Terminal Cisternae of Sarcoplasmic-Reticulum from Fast Skeletal-Muscle. *Journal of Biological Chemistry* 262: 1740-1747
- Isberg RR, O'Connor TJ, Heidtman M (2009) The *Legionella pneumophila* replication vacuole: making a cosy niche inside host cells. *Nat Rev Microbiol* 7: 13-24

Kalayil S, Bhogaraju S, Bonn F, Shin D, Liu YB, Gan NH, Basquin J, Grumati P, Luo ZQ, Dikic I (2018) Insights into catalysis and function of phosphoribosyl-linked serine ubiquitination. *Nature* 557: 734-+

Kimanius D, Forsberg BO, Scheres SHW, Lindahl E (2016) Accelerated cryo-EM structure determination with parallelisation using GPUs in RELION-2. *Elife* 5

Komander D, Rape M (2012) The ubiquitin code. *Annu Rev Biochem* 81: 203-29

Kremer JR, Mastronarde DN, McIntosh JR (1996) Computer visualization of three-dimensional image data using IMOD. *Journal of Structural Biology* 116: 71-76

Krogh A, Larsson B, von Heijne G, Sonnhammer ELL (2001) Predicting transmembrane protein topology with a hidden Markov model: Application to complete genomes. *Journal of Molecular Biology* 305: 567-580

Kudryashev M (2018) Cellular Imaging. *Biological and Medical Physics, Biomedical Engineering: Springer, Cham*

Kuhlbrandt W (2014) The Resolution Revolution. *Science* 343: 1443-1444

Kwak MJ, Kim JD, Kim H, Kim C, Bowman JW, Kim S, Joo K, Lee J, Jin KS, Kim YG, Lee NK, Jung JU, Oh BH (2017) Architecture of the type IV coupling protein complex of *Legionella pneumophila*. *Nat Microbiol* 2: 17114

Laganowsky A, Reading E, Allison TM, Ulmschneider MB, Degiacomi MT, Baldwin AJ, Robinson CV (2014) Membrane proteins bind lipids selectively to modulate their structure and function. *Nature* 510: 172-175

Lai FA, Erickson HP, Rousseau E, Liu QY, Meissner G (1988) Purification and Reconstitution of the Calcium Release Channel from Skeletal-Muscle. *Nature* 331: 315-319

Lanner JT, Georgiou DK, Joshi AD, Hamilton SL (2010) Ryanodine receptors: structure, expression, molecular details, and function in calcium release. *Cold Spring Harb Perspect Biol* 2: a003996

Leigh KE, Navarro PP, Scaramuzza S, Chen W, Zhang Y, Castano-Diez D, Kudryashev M (2019) Subtomogram averaging from cryo-electron tomograms. *Methods Cell Biol* 152: 217-259

Li X, Mooney P, Zheng S, Booth CR, Braunfeld MB, Gubbens S, Agard DA, Cheng Y (2013a) Electron counting and beam-induced motion correction enable near-atomic-resolution single-particle cryo-EM. *Nat Methods* 10: 584-90

Li XM, Mooney P, Zheng S, Booth CR, Braunfeld MB, Gubbens S, Agard DA, Cheng YF (2013b) Electron counting and beam-induced motion correction enable near-atomic-resolution single-particle cryo-EM. *Nature Methods* 10: 584-+

MacMillan D, Currie S, McCarron JG (2008) FK506-binding protein (FKBP12) regulates ryanodine receptor-evoked Ca²⁺ release in colonic but not aortic smooth muscle. *Cell Calcium* 43: 539-49

Mastrorade DN (2005) Automated electron microscope tomography using robust prediction of specimen movements. *J Struct Biol* 152: 36-51

Mio K, Mio M, Arisaka F, Sato M, Sato C (2010) The C-terminal coiled-coil of the bacterial voltage-gated sodium channel NaChBac is not essential for tetramer formation, but stabilizes subunit-to-subunit interactions. *Prog Biophys Mol Bio* 103: 111-121

Mio K, Sato C (2018) Lipid environment of membrane proteins in cryo-EM based structural analysis. *Biophys Rev* 10: 307-316

Mitchell RD, Palade P, Fleischer S (1983) Purification of morphologically intact triad structures from skeletal muscle. *J Cell Biol* 96: 1008-16

Mukhopadhyay D, Riezman H (2007) Proteasome-independent functions of ubiquitin in endocytosis and signaling. *Science* 315: 201-5

Nakai J, Imagawa T, Hakamat Y, Shigekawa M, Takeshima H, Numa S (1990) Primary structure and functional expression from cDNA of the cardiac ryanodine receptor/calcium release channel. *FEBS Lett* 271: 169-77

Newton HJ, Ang DK, van Driel IR, Hartland EL (2010) Molecular pathogenesis of infections caused by *Legionella pneumophila*. *Clin Microbiol Rev* 23: 274-98

Nidhish Raj TM (2018) Multilabel Classification of Membrane Protein in Human by Decision Tree (DT) Approach. *Biomed Pharmacol J*

Nyholm TK (2015) Lipid-protein interplay and lateral organization in biomembranes. *Chem Phys Lipids* 189: 48-55

Orlova EV, Saibil HR (2011) Structural Analysis of Macromolecular Assemblies by Electron Microscopy. *Chem Rev* 111: 7710-7748

Otsu K, Willard HF, Khanna VK, Zorzato F, Green NM, MacLennan DH (1990) Molecular-Cloning of Cdna-Encoding the Ca-2+ Release Channel (Ryanodine Receptor) of Rabbit Cardiac-Muscle Sarcoplasmic-Reticulum. *Journal of Biological Chemistry* 265: 13472-13483

Paolini C, Protasi F, Franzini-Armstrong C (2004) The relative position of RyR feet and DHPR tetrads in skeletal muscle. *J Mol Biol* 342: 145-53

Park H, Wu S, Dunker AK, Kang C (2003) Polymerization of calsequestrin. Implications for Ca²⁺ regulation. *J Biol Chem* 278: 16176-82

Petterson EF, Goddard TD, Huang CC, Couch GS, Greenblatt DM, Meng EC, Ferrin TE (2004) UCSF chimera - A visualization system for exploratory research and analysis. *J Comput Chem* 25: 1605-1612

Pickart CM, Eddins MJ (2004) Ubiquitin: structures, functions, mechanisms. *Biochim Biophys Acta* 1695: 55-72

- Prosser BL, Wright NT, Ndez-Ochoa EOH, Varney KM, Liu Y, Olojo RO, Zimmer DB, Weber DJ, Schneider MF (2008) S100A1 binds to the calmodulin-binding site of ryanodine receptor and modulates skeletal muscle excitation-contraction coupling. *Journal of Biological Chemistry* 283: 5046-5057
- Protasi F (2002) Structural interaction between RYRs and DHPRs in calcium release units of cardiac and skeletal muscle cells. *Front Biosci* 7: D650-D658
- Punjani A, Rubinstein JL, Fleet DJ, Brubaker MA (2017) cryoSPARC: algorithms for rapid unsupervised cryo-EM structure determination. *Nature Methods* 14: 290-+
- Qiu J, Luo ZQ (2017) Legionella and Coxiella effectors: strength in diversity and activity. *Nat Rev Microbiol* 15: 591-605
- Qiu JZ, Sheedlo MJ, Yu KW, Tan YH, Nakayasu ES, Das C, Liu XY, Luo ZQ (2016) Ubiquitination independent of E1 and E2 enzymes by bacterial effectors. *Nature* 533: 120-+
- Renken C, Hsieh CE, Marko M, Rath B, Leith A, Wagenknecht T, Frank J, Mannella CA (2009) Structure of frozen-hydrated triad junctions: A case study in motif searching inside tomograms. *Journal of Structural Biology* 165: 53-63
- Rios E, Brum G (1987) Involvement of Dihydropyridine Receptors in Excitation Contraction Coupling in Skeletal-Muscle. *Nature* 325: 717-720
- Rios E, Pizarro G (1991) Voltage Sensor of Excitation-Contraction Coupling in Skeletal-Muscle. *Physiol Rev* 71: 849-908
- Rohou A, Grigorieff N (2015) CTFFIND4: Fast and accurate defocus estimation from electron micrographs. *J Struct Biol* 192: 216-21

- Samsó M, Feng W, Pessah IN, Allen PD (2009) Coordinated Movement of Cytoplasmic and Transmembrane Domains of RyR1 upon Gating. *Plos Biol* 7: 980-995
- Scheres SH (2012) RELION: implementation of a Bayesian approach to cryo-EM structure determination. *J Struct Biol* 180: 519-30
- Schneider MF (1994) Control of Calcium-Release in Functioning Skeletal-Muscle Fibers. *Annu Rev Physiol* 56: 463-484
- Schnell JD, Hicke L (2003) Non-traditional functions of ubiquitin and ubiquitin-binding proteins. *J Biol Chem* 278: 35857-60
- Sheedlo MJ, Qiu JZ, Tan YH, Paul LN, Luo ZQ, Das C (2015) Structural basis of substrate recognition by a bacterial deubiquitinase important for dynamics of phagosome ubiquitination. *P Natl Acad Sci USA* 112: 15090-15095
- Song K, Shang Z, Fu X, Lou X, Grigorieff N, Nicastro D (2019) In situ structure determination at nanometer resolution using TYGRESS. *Nat Methods*
- Stark H (2010) GraFix: stabilization of fragile macromolecular complexes for single particle cryo-EM. *Methods Enzymol* 481: 109-26
- Steven AC, Aebi U (2003) The next ice age: cryo-electron tomography of intact cells. *Trends Cell Biol* 13: 107-10
- Takayuki Kato FM, Takanori Nakane, Naoya Terahara, Takeshi Kaneko, Yuko Shimizu, Sohei Motoki, Isamu Ishikawa, Koji Yonekura, Keiichi Namba (2019) CryoTEM with a cold field emission gun that moves structural biology into a new stage. *MicroscMicroanal*
- Takeshima H, Nishimura S, Matsumoto T, Ishida H, Kangawa K, Minamino N, Matsuo H, Ueda M, Hanaoka M, Hirose T, Numa S (1989) Primary Structure and Expression from Complementary-DNA of Skeletal-Muscle Ryanodine Receptor. *Nature* 339: 439-445

- Timmermans FJ, Otto C (2015) Review of integrated correlative light and electron microscopy. *Rev Sci Instrum* 86
- Tsurumura T, Tsumori Y, Qiu H, Oda M, Sakurai J, Nagahama M, Tsuge H (2013) Arginine ADP-ribosylation mechanism based on structural snapshots of iota-toxin and actin complex. *P Natl Acad Sci USA* 110: 4267-4272
- Turonova B, Schur FKM, Wan W, Briggs JAG (2017) Efficient 3D-CTF correction for cryo-electron tomography using NovaCTF improves subtomogram averaging resolution to 3.4 angstrom. *Journal of Structural Biology* 199: 187-195
- van Meer G, Voelker DR, Feigenson GW (2008) Membrane lipids: where they are and how they behave. *Nat Rev Mol Cell Biol* 9: 112-24
- Vinothkumar KR, Zhu J, Hirst J (2014) Architecture of mammalian respiratory complex I. *Nature* 515: 80-84
- von Heijne G (2006) Membrane-protein topology. *Nat Rev Mol Cell Biol* 7: 909-18
- Wagenknecht T, Berkowitz J, Grassucci R, Timerman AP, Fleischer S (1994) Localization of calmodulin binding sites on the ryanodine receptor from skeletal muscle by electron microscopy. *Biophys J* 67: 2286-95
- Wagenknecht T, Grassucci R, Frank J, Saito A, Inui M, Fleischer S (1989) Three-dimensional architecture of the calcium channel/foot structure of sarcoplasmic reticulum. *Nature* 338: 167-70
- Wagenknecht T, Hsieh C, Marko M (2015) Skeletal muscle triad junction ultrastructure by Focused-Ion-Beam milling of muscle and Cryo-Electron Tomography. *Eur J Transl Myol* 25: 49-56
- Wagner T, Merino F, Stabrin M, Moriya T, Antoni C, Apelbaum A, Hagel P, Sitsel O, Raisch T, Prumbaum D, Quentin D, Roderer D, Tacke S, Siebolds B, Schubert E, Shaikh TR, Lill P, Gatsogiannis C, Raunser S

(2019) SPHIRE-crYOLO is a fast and accurate fully automated particle picker for cryo-EM. *Commun Biol* 2: 218

Wan W, Briggs JAG (2016) Cryo-Electron Tomography and Subtomogram Averaging. *Method Enzymol* 579: 329-367

Wang Y, Shi M, Feng H, Zhu YL, Liu SQ, Gao A, Gao P (2018) Structural Insights into Non-canonical Ubiquitination Catalyzed by SidE. *Cell* 173: 1231-+

Wei L, Varsanyi M, Dulhunty AF, Beard NA (2006) The conformation of calsequestrin determines its ability to regulate skeletal ryanodine receptors. *Biophysical Journal* 91: 1288-1301

Wei R, Wang X, Zhang Y, Mukherjee S, Zhang L, Chen Q, Huang X, Jing S, Liu C, Li S, Wang G, Xu Y, Zhu S, Williams AJ, Sun F, Yin CC (2016a) Structural insights into Ca(2+)-activated long-range allosteric channel gating of RyR1. *Cell Res* 26: 977-94

Wei X, Su X, Cao P, Liu X, Chang W, Li M, Zhang X, Liu Z (2016b) Structure of spinach photosystem II-LHCII supercomplex at 3.2 Å resolution. *Nature* 534: 69-74

Willegems K, Efremov RG (2018) Influence of Lipid Mimetics on Gating of Ryanodine Receptor. *Structure* 26: 1303-1313 e4

Witherspoon JW, Meilleur KG (2016) Review of RyR1 pathway and associated pathomechanisms. *Acta Neuropathol Commun* 4: 121

Wright NT, Prosser BL, Varney KM, Zimmer DB, Schneider MF, Weber DJ (2008) S100A1 and calmodulin compete for the same binding site on ryanodine receptor. *Journal of Biological Chemistry* 283: 26676-26683

Wu J, Yan Z, Li Z, Yan C, Lu S, Dong M, Yan N (2015) Structure of the voltage-gated calcium channel Cav1.1 complex. *Science* 350: aad2395

Yamaguchi N, Xin CL, Meissner G (2001) Identification of apocalmodulin and Ca²⁺-calmodulin regulatory domain in skeletal muscle Ca²⁺ release

channel, ryanodine receptor. *Journal of Biological Chemistry* 276: 22579-22585

Yan Z, Bai X, Yan C, Wu J, Li Z, Xie T, Peng W, Yin C, Li X, Scheres SHW, Shi Y, Yan N (2015) Structure of the rabbit ryanodine receptor RyR1 at near-atomic resolution. *Nature* 517: 50-55

Yokogawa M, Fukuda M, Osawa M (2019) Nanodiscs for Structural Biology in a Membranous Environment. *Chem Pharm Bull* 67: 321-326

Zalk R, Clarke OB, des Georges A, Grassucci RA, Reiken S, Mancina F, Hendrickson WA, Frank J, Marks AR (2015) Structure of a mammalian ryanodine receptor. *Nature* 517: 44-9

Zhang K (2016) Gctf: Real-time CTF determination and correction. *Journal of Structural Biology* 193: 1-12

Zhang P (2019) Advances in cryo-electron tomography and subtomogram averaging and classification. *Curr Opin Struct Biol* 58: 249-258

Zheng SQ, Palovcak E, Armache JP, Verba KA, Cheng Y, Agard DA (2017) MotionCor2: anisotropic correction of beam-induced motion for improved cryo-electron microscopy. *Nat Methods* 14: 331-332

Zorzato F, Fujii J, Otsu K, Phillips M, Green NM, Lai FA, Meissner G, MacLennan DH (1990) Molecular-Cloning of Cdna-Encoding Human and Rabbit Forms of the Ca-2+ Release Channel (Ryanodine Receptor) of Skeletal-Muscle Sarcoplasmic-Reticulum. *Journal of Biological Chemistry* 265: 2244-2256

Declaration of Contributions and Publications

Except where stated otherwise by reference or acknowledgement, the work presented was generated by myself under the supervision of my advisors during my doctoral studies. All contributions from colleagues are explicitly referenced in the thesis. The material listed below was obtained in the context of collaborative research:

Figure 3.3.1.1: The new structure of closed RyR1 *in situ*.

Figure 3.3.1.2: Volume-rendered visualizations of the new average structure of closed RyR1 at 9.5 Å resolution.

Ricardo Sanchez, group of Dr. Misha Kudryashev, Max-Planck-Institute of Biophysics. Structure determination of closed RyR1 *in situ* using hybrid method.

Figure 4.3.1.1: Purification of SdeC.

Figure 4.3.3.1: Crystal structure of SdeA-CC₁₁₅₈₋₁₄₉₉.

Figure 4.3.3.2:

Figure 4.4.2: Assumed interaction between DotL(656-783)-IcmW-IcmS complex and SdeA- CC₁₁₅₈₋₁₄₉₉.

Dr. Mohit Misra, group of Prof. Dr . Ivan Dikic, Goethe Frankfurt University. Purification of SdeC and crystal structure determination of SdeA-CC₁₁₅₈₋₁₄₉₉.

Curriculum Vitae

Personal information:

Name: Wenbo Chen Birth date: 25.11.1989 Nationality: China

Education background:

From 2008 to 2012, bachelor degree in biological science, Shandong University, China.

Supervisor: Prof. Dr. Lichuan Gu, Bachelor thesis: Molecular mechanism by which Ydiv acts as an enhancing factor in Clpxp degrading FlhD₄C₂

From 2013 to 2016, master degree in biochemistry and molecular biology, Institute of Biophysics, Chinese Academy of Sciences, China.

Supervisor: Dr. Fei Sun. Master thesis: Structural studies of mitochondrial inner membrane division by S-OPA1 under pressure

From 2016 to 2020, doing PhD study in Max-Planck-Institute of Biophysics, Germany.

Supervisor: Dr. Misha Kudryashev. PhD thesis: Structure and function of integral and peripheral membrane proteins by cryo-EM: RyR1 and SidE family proteins

International conferences

August 24-29, 2018. The 11th K.H.Kuo Summer School of Electron Microscopy & Crystallography 2018 Kuo Symposium on 3D-EM of Macromolecules and cells, Zhejiang University, Hangzhou, China

June 2-5, 2019. The Second Russian international conference “Cryo-electron microscopy 2019: achievements and prospects”, Lomonosov Moscow State University, Moscow, Russia. Poster: Structure of RyR1 in native membranes

Language skills:

Chinese (native), English (fluent) and German (B1 level)

Publications

1. **Chen, W.**, Kudryashev, M.: Structure of RyR1 in native membranes. *EMBO Reports*, e49891, doi: 10.15252/embr.201949891 (2020).
2. Zhang, D., Zhang, Y., Ma, J., Zhu, C., Niu, T., **Chen, W.**, Pang, X., Zhai, Y., Sun, F.: Cryo-EM structures of S-OPA1 reveal its interactions with membrane and changes upon nucleotide binding. *eLife* 2020;9:e50294, doi:10.7554/eLife.50294 (2020).
3. Sanchez, R., Zhang, Y., **Chen, W.**, Dietrich, L., Kudryashev, M.: Subnanometer-resolution structure determination *in situ* by a hybrid Subtomogram Averaging-Single Particle Cryo-EM-Workflow. (In preparation)
4. Bhaskara, R. M., Grumati, P., Pardo, J. G., Kalayil, S., Pinto, A. C., **Chen, W.**, Kudryashev, M., Dikic, I., Hummer, G.: Curvature induction and membrane remodeling by FAM134B reticulon homology domain assist selective ER-phagy. *Nat Commun* **10**, 2370, doi:10.1038/s41467-019-10345-3 (2019).
5. Leigh, K. E., Navarro, P. P., Scaramuzza, S., **Chen, W.**, Zhang, Y., Diez, D. C., Kudryashev, M.: Subtomogram averaging from cryo-electron tomograms. *Methods Cell Biol* **152**, 217-259, doi:10.1016/bs.mcb.2019.04.003 (2019).

Acknowledgment

Time flies! It has been almost four years since I came to Max-Planck-Institute of Biophysics to work on my PhD. It is exciting for me to finish my PhD thesis after giving enormous efforts and write the acknowledgment here.

I appreciate all the people who have provided kind help and generous support to me during my pursuit of the doctorate. I thank my PhD supervisor, Dr. Misha Kudryashev, a great and remarkable scientist in the field of cryo electron microscopy. Dr. Misha Kudryashev is not only patient and helpful in guiding students how to do scientific researches, but also is very considerate of us as he gives additional fellowship to students to make our lives better. In addition, I grasped tomography and subtomogram averaging technique from him, for which I am very thankful. I thank my co-supervisors, Prof. Dr. Klaas-Martinus Pos and Prof. Dr. Eric Geertsma from Goethe Frankfurt University, for their co-guidance during my work and for being TRAM committee members of me.

I thank all my dear lab members including the ones that have left our lab for their help to me in many aspects. They are Eva, Patricia, Ashishi, Kendra, Bianca, Yingyi Zhang, Shihying Chang, Ricardo, Nikita, Wolfram, Simon, Daniel, Guiqun and Luise.

I thank Max-Planck-Institute of Biophysics for providing excellent experimental facilities and considerable support in administration so that I can carry out my work smoothly. The secretary of our department does a very good job in the administration work, and Silvia helps me in my visa extension. Thanks to all of them.

I thank my collaborators, Dr. Mohit Misra and the lab leader Prof. Dr. Ivan Dikic from the Buchmann Institute for Molecular Life Sciences, Goethe

Frankfurt University for their wonderful collaboration on the work of structural studies of the SidE family proteins.

I thank my other collaborators, Dr. Bing Ni and the lab leader Prof. Dr. Victor Sourjik from the Max Planck Institute for Terrestrial Microbiology for their wonderful collaboration on the work of structural studies of bacterial flagellar motor.

I thank my parents and my brother for supporting me to come to Germany to study.